KUNGL TEKNISKA HÖGSKOLAN

TRITA-MEK
Technical Report 1997:1
ISSN 0348-467X
ISRN KTH/MEK/TR—97/1-SE

Experimental and Theoretical Studies of Plane Liquid Jets

Daniel Söderberg

Licentiate Thesis
Stockholm, 1997

Royal Institute of Technology
Department of Mechanics

Abstract

In modern paper manufacturing free liquid jets are used to distribute the fibre suspension to the paper machine. It is believed that the homogeneity of the jet flow is of vital importance to obtain a good quality paper. The present investigation has been undertaken in order to better understand the development of free, plane liquid jets. Both the development of the basic laminar flow as well as its stability have been investigated. This includes both the formulation of the problem with the appropriate boundary conditions, obtaining solutions for the basic flow field and to the stability equations for two-dimensional wave disturbances as well as comparisons with experiments. The experiments have been made with two different nozzles, a plane channel flow nozzle giving a nearly parabolic outflow velocity distribution and a slit nozzle which closely approximates an inviscid jet. Both flow visualization and velocity measurements of the jet flow have been made. The basic flow of the channel flow jet was analyzed and the relaxation length determined. The stability analysis showed that the boundary conditions at the jet surface were important for the instability, assuming an inviscid ambient gas overestimated the instability considerably as compared to a viscous gas. The stability calculations show that two types of wave disturbances may exist, either sinuous or varicose. Depending on the parameters of the problem (such as the Reynolds number and the basic velocity distribution) one or several modes may be unstable. These modes were mapped in the parameter range of the present experiments and the sinuous modes were found to be the most unstable. Hot wire anemometry measurements of controlled forced disturbances showed that these waves also were sinuous. When the waves reach a certain amplitude they break up which creates strong streaky structures in the jet.

To my wife and my children

Contents

CHAPTER 1

Introduction

Paper manufacturing originates from China and the technology is more than 2000 years old. Despite the long history of paper manufacturing the basic principle has not changed and is still based on letting a suspension of water and fibres settle on a permeable surface which traps the fibres but allows the water to pass. As the water is removed the fibres form a network, a fibre mat, which after dehydration becomes a paper sheet. For a long time the sheets were handmade but the process has been automated and is today continuous. The fibre suspension is formed into a plane liquid jet by a nozzle, a so called headbox, and distributed on one or between two moving permeable bands or wires. The velocity of the jet is 10-35 m/s and it is typically 5-10 m wide and 1 cm thick. After being trapped between the two wires the water is removed by pressure pulses created by roll nips, *e.g.* two counter-rotating cylinders, or blades pressed against the moving wires. Finally the remaining water is removed by heat. The fibre suspensions which are fed to the paper machine usually have a fibre concentration less than 1% but still such a suspension is a non-Newtonian liquid where fibres tend to flocculate and form fibre networks.

The development of modern paper technology, when it comes to the forming part, *i.e.* the first part of the paper machine, is towards higher velocities and multi-layered forming. Multi-layered forming (see figure 1.1) is done by ejecting two or more co-planar jets which consist of different fibre suspensions. By this procedure it is possible to produce a paper where the properties varies throughout the sheet. This will for example make it possible to have a core with strong paper covered with surface layers that give good printing quality.

Problems in the final product can consist of density and thickness variations in the sheet as well as unwanted orientation of the fibres. Specifically, streaky structures can be found in both the machine direction, *i.e.* the streaks are in the direction of the jet, and in the cross machine direction. These problems are primarily believed to originate from non-homogeneities in the liquid jet flow, since the fibre network will form very quickly after entering between the wires and prevent further mixing and re-distribution. In order to understand the origins of these problems and hopefully improve the possibility to control the flow process, the behaviour of the free liquid jet flow has to be understood. The present work consists of a theoretical and experimental study of the fluid mechanics of plane liquid jets, and is part of a larger effort within the FaxénLaboratory, KTH, to

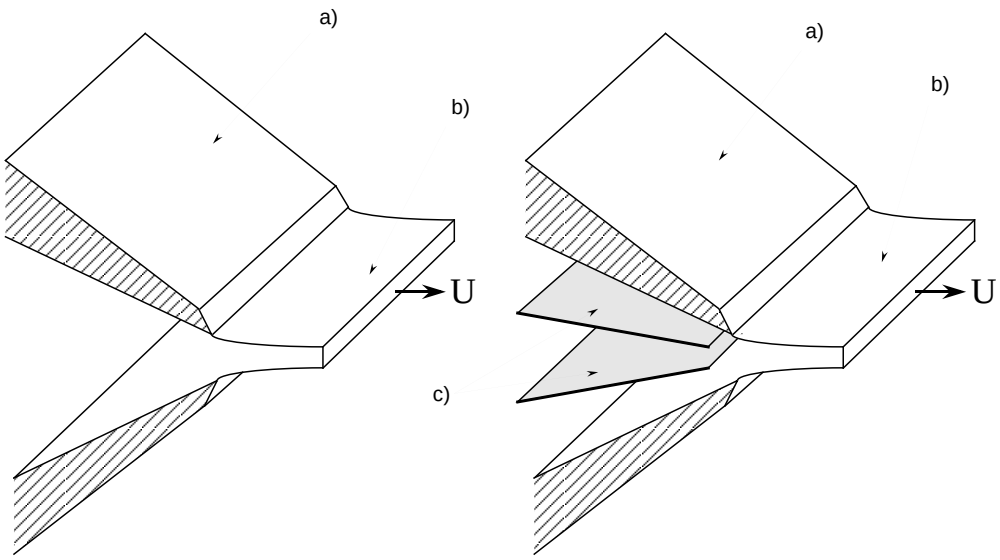

FIGURE 1.1. Nozzles producing liquid jets. Simple (left) and for multi-layered forming (right). a) nozzle, b) liquid jet and c) separation vanes.

understand the fluid mechanics of the first stages in the forming process of modern paper machines.

1.1. Previous studies of liquid jets

The flow of free, especially cylindrical, liquid jets has attracted much attention during the history of fluid mechanics. Free liquid jets are used in many industrial applications, for example jet cutting, fuel injection and cooling through impingement. Also, as mentioned earlier, the most common method used when producing paper includes the flow of a plane liquid jet. The research concerning cylindrical liquid jets has mainly been focused on liquid jet break-up to be able to predict and control the droplet size.

1.1.1. Laminar flow of liquid jets. The laminar flow of liquid jets will depend on geometry and nozzle shape. If the flow of a plane *i.e.* two-dimensional liquid jet, is considered to be inviscid and irrotational, *i.e.* potential flow, a solution for the location of the free surface and the velocity field can be obtained by conformal mapping. For a jet emanating from a two dimensional orifice (slit), the solution can be found in many fluid dynamics textbooks, see for example Lamb (1932), Pai (1954) and Batchelor (1967). This can be extended to a nozzle with varying angle of contraction, Söderberg (1994).

The outflow from a plane two-dimensional channel with an upstream fully developed laminar flow, the so called plane Poiseuille flow, was analyzed by Tillet (1968). He did this by a boundary layer assumption and gave a solution in form of a series expansion, which shows that the streamwise velocity undergoes a relaxation from the fully developed parabolic profile at the end of the channel to a uniform velocity distribution. The analysis is only valid for high Reynolds numbers.

For the flow of more general liquid jets, which are partly or fully dominated by viscous forces the basic flow has to be solved with numerical methods. Nickell, Tanner & Caswell (1974) made a numerical investigation of the circular liquid jet at low Reynolds numbers. The aim was to investigate the die swell phenomenon, which is a typical effect of a non-Newtonian fluid, *e.g.* polymer melts. A jet that expands directly when leaving the nozzle is said to experience a die swell. For a low Reynolds number Newtonian jet this occurs too. This was discovered experimentally by Gavis & Modan (1967). They found that the circular liquid jet expanded for Reynolds numbers below 16. The calculations by Nickell *et al.* also showed that the Newtonian die-swell is about 13%. The reason for this was mainly the stress singularity at the end of the nozzle where the boundary conditions change from no-slip to no-shear.

The flow of a plane liquid jet emanating from a nozzle with varying contraction ratio, *i.e* the converging angle of the nozzle, was investigated numerically by Yu & Liu (1992). The results show that also the plane liquid jet expands for low Reynolds numbers. When the contraction ratio increases the expansion of the jet at low Reynolds numbers becomes smaller. Also, when the Reynolds number is increased a high contraction ratio gives a location of the surface as predicted by the theory for a potential jet.

1.1.2. Stability and break-up of cylindrical jets. One of the earliest results concerning the hydrodynamics of liquid jets was obtained by Plateau (1873), who predicted the most probable droplet size by considering the surface area of a liquid cylinder. The surface tension can also be expressed as a surface energy, and by minimization of the surface area the energy is also at a minimum state. This is obtained if the column breaks up into pieces that are $2\pi a$ long, where a is the radius of the cylinder. The theoretical result was in agreement with experimental results by Savart (1833).

As one of the earliest results using linear stability theory Rayleigh (1896) considered a liquid jet with a uniform velocity distribution, *i.e.* the flow is parallel and the velocity constant throughout the jet. Viscosity in the liquid is neglected, *i.e.* the flow is assumed to be inviscid. No effects of the ambient gas are considered but superficial forces are assumed to act on the surface of the jet. The analysis was performed by the assumption that the surface of the jet is subjected to an infinitesimal perturbation and predicts that the liquid cylinder will break up into droplets for axisymmetric disturbances only. It also shows that break-up

will occur only for disturbances with a wavelength λ that satisfies $\lambda > 2\pi a$, where a is the radius of the cylinder.

Since then linear stability theory has been used extensively for various flow situations, for example, different types of channel flow and boundary layer flow along a flat plate. Linear stability theory for the break-up of a cylindrical jet has later been extended to include viscosity and non-linear effects. This has been done experimentally and numerically, and is reviewed by McCarthy & Molloy (1974) and Bogy (1979). It is shown experimentally, (Goedde & Yuen, 1970), that non-linear effects cause ligaments between the drops when the jet disintegrates and the conclusion is that non-linear effects dominate the growth process.

The effect of a non-uniform velocity distribution inside a cylindrical jet has also been considered theoretically by Leib & Goldstein (1986) and experimentally by Debler & Yu (1988). The theoretical result is based on a spatial stability analysis, and the conclusion is that the growth of a disturbance is lower when the velocity profile in the liquid jet deviates from the uniform. The experiments by Debler & Yu (1988), were carried out by investigating the stability of a circular liquid jet emanating from tubes of varying length. With a constant flow rate through the tubes the profiles at the end of the tubes were more or less developed. The experiments gave qualitatively the same result, *i.e.* the growth rate is reduced with a non-uniform profile. They also showed that the turbulence level in the tube had a significant effect on the break-up length of the jet. A higher turbulence level gave a more rapid disintegration of the jet.

These investigations are all concerned with the axisymmetric disturbance which break-up into discrete droplets. This type of break-up is also denoted 'varicose'. If the velocity of the jet is increased the break-up will be different, see Hoyt & Taylor (1977). They made visualizations of a circular liquid jet emanating from a converging nozzle where the end was a short straight pipe. The experiment also allowed for a co-flowing gas which could have a higher velocity than the liquid in the jet. Close to the exit short waves, *i.e.* wavelengths orders of magnitude smaller than the jet diameter, could be seen which broke up a few jet diameters downstream. The result of the break-up was formation of spray droplets, and the break-up was not sensitive to the velocity of the ambient gas. Further downstream a helical disturbance could be seen growing. This disturbance had a large amplitude and was enhanced by a higher velocity of the gas.

The wavelengths found for the short waves were compared with linear stability results by Brennen (1970), which were obtained for a hydrodynamic cavity behind axisymmetric headforms.

1.1.3. Stability and break-up of plane liquid jets. The stability of a plane liquid jet has not been studied to the same extent as the cylindrical. A plane jet is basically two-dimensional with a thickness that is small compared to its width. Also, the basic flow is assumed to be symmetric with respect to the centreline of the jet. One type of instability is a two-dimensional travelling wave disturbance, which can be either symmetric or anti-symmetric, see figure 1.2.

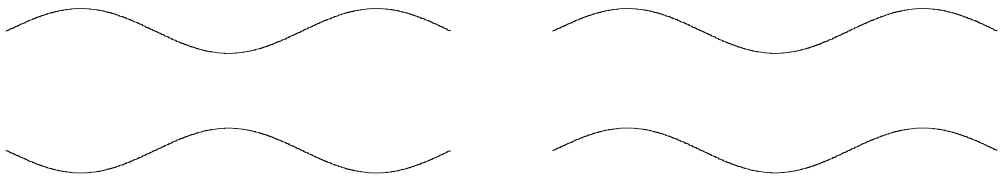

FIGURE 1.2. Definition of symmetry. Symmetric or varicose (left) and antisymmetric or sinuous (right).

Earlier work have studied the stability of plane liquid jets at different levels of approximation. If a liquid jet with no ambient gas is considered this can be done in basically the same manner and with the same assumptions of uniform velocity and surface tension as the study by Rayleigh (1896) of the circular jet, see Drazin & Reid (1981). This study shows that the jet is stable to all kinds of disturbances since surface tension always has a damping effect and forces the surface back to its rest state when perturbed. This is the opposite to the result for the circular geometry, since for the plane jet there is no transport of information, when surface tension is considered, from one surface of the jet to the other.

To improve this result Hagerty & Shea (1955) assumed that the jet was surrounded by an inviscid gas, and as the jet moved through the gas, which was at rest, it resulted in an aerodynamic drag on the perturbed surface of the jet. The result is that the jet is unstable to external perturbations within a limited wavelength band.

These results were further improved by Li & Tankin (1991), who made the same type of calculation but for a viscous liquid. The conclusions from their study was that the main reason for instability is the aerodynamic drag from the surrounding gas, but, in a certain parameter region viscosity enhances the growth. Surface tension always acts as a restoring force.

Experimental investigations concerning plane liquid jets have mainly been through flow visualizations, but also measurements of spray angle and break-up lengths have been done. Mansour & Chigier (1991) studied atomization and investigated the break-up length of a plane liquid jet with co-flowing gas, where the gas has a higher velocity than the jet. This configuration is interesting since in combustion annular liquid jets with co-flowing high speed gas are used for fuel injection. Measurements of the turbulent flowfield in a free liquid jet were made by Wolf, Incropera & Wiskanta (1992). Also, visualizations and measurements of mean flow and turbulence quantities, by Laser Doppler Velocimetry, for a high Reynolds number jet emanating from a converging channel was made by Lindqvist (1996).

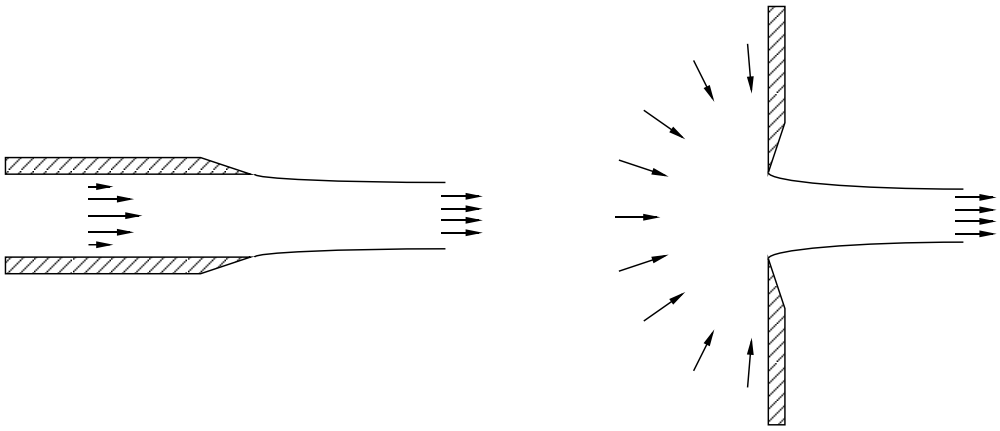

FIGURE 1.3. Nozzles used. Channel (left) and slit (right).

1.2. Present work

The present work examines the flow and stability of laminar plane liquid jets. Special emphasis is put on the influence of the nozzle producing the liquid jet. A nozzle can have many different shapes, but to limit the investigation two canonical shapes of the nozzle have been considered, one which consists of a plane channel and the other which consists of a slit, figure 1.3.

The channel nozzle is assumed to have a fully or partly developed laminar upstream flow. If the channel is long enough the velocity distribution in the channel will take the form of a parabola. When this emanates into a ambient gas with a lower viscosity and density the fluid inside the jet will be redistributed to eventually become uniform.

The process of velocity profile relaxation has been investigated numerically. The result is that the distance, ℓ_R, to reach a uniform velocity distribution is $\ell_R = 0.36aRe$, where Re is the Reynolds number based on half the channel height a and the mean velocity. This shows that the relaxation of the jet is a weaker process than for developing channel flow, for which the entrance length, ℓ_E, is given by $\ell_E = 0.16aRe$, see *e.g.* Schlichting (1979). Also, the calculation shows that this length is approximately independent of the flow profile at the end of the channel. The effect of a surrounding gas was also examined. If the viscosity of the gas is smaller than the viscosity of the liquid in the jet the effect was shown to be small. Experimental measurements of the velocity profile inside the jet was made with a Pitot tube. These were compared with calculations which showed a fair agreement confirming the theoretical calculations.

The flow through the slit nozzle on the other hand is mainly inviscid. It has been shown in numerical calculations that the location of the free surface, as predicted by inviscid theory, is in good agreement with numerical calculations

and experiments for high contraction angles of the nozzle, Yu & Liu (1992). Also, Pitot tube measurements of the liquid jet emanating from the slit nozzle were made in the present study. These show that the jet also has a uniform velocity distribution close to the nozzle, and is in agreement with inviscid theory.

The instabilities of the jet flow was studied through flow visualization using both the shadowgraph method and by adding reflective flakes to the water. Several different types of instabilities were observed. For the channel jet flow two-dimensional waves were observed on the surface of the jet. These waves grow in amplitude and break up. The particle visualizations show that the break-up occurs along a well defined line parallel to the nozzle. The break-up causes a streamwise streaky structure and a partial disintegration of the jet. In both nozzles another type of stationary as well as non-stationary streaky instabilities were observed originating from inside of the nozzle. However, the streaks caused by the break-up of the waves appear to be the stronger. With increasing velocity the break-up moves closer to the channel outlet. This type of instability could not be found in the slit nozzle at any velocity possible to obtain in the experiments.

The jet emanating from the channel nozzle has been analyzed with linear stability theory and five different unstable modes were found, three anti-symmetric and two symmetric. These are unstable for different wavenumbers and positions in the jet. In the experiments waves on the jet were triggered by acoustic excitation at velocities below where the 'natural' waves occurred. Measurements of these with the use of hot wire anemometry were performed, showing that the triggered waves were anti-symmetric. The spatial variation of the wavelength of the waves were obtained by image processing of the flow visualization experiments.

CHAPTER 2

Basic assumptions and geometry

A free liquid jet is produced by forcing a liquid through a nozzle and out into a gas. The characteristics of the jet depend on the geometry of the nozzle, upstream conditions and physical properties of the liquid and gas. Here the plane liquid jet is assumed to be emanating from a converging channel, see figure 2.1, with an upstream specified flow. Both the liquid and gas are assumed to be incompressible Newtonian fluids. The equations governing the liquid and gas phases are the momentum equations

$$\rho\left(\frac{\partial u_i}{\partial t}+u_k\frac{\partial u_i}{\partial x_k}\right)=-\frac{\partial p}{\partial x_i}+\mu\frac{\partial^2 u_i}{\partial x_k\partial x_k}+\rho f_i,\quad i=1,2,3. \tag{1}$$

and the continuity equation

$$\frac{\partial u_i}{\partial x_i}=0, \tag{2}$$

where $\mathbf{u}=\mathbf{u}(\mathbf{x},t)=u_i\mathbf{e}_i=u\mathbf{e}_x+v\mathbf{e}_y+w\mathbf{e}_z$, is the velocity vector, p the pressure, ρ the density, μ the dynamic viscosity and f_i an external volume force.

The orientation and geometry of the nozzle can be seen in figure 2.1, where the x-direction also will be referred to as the streamwise direction of the jet, the

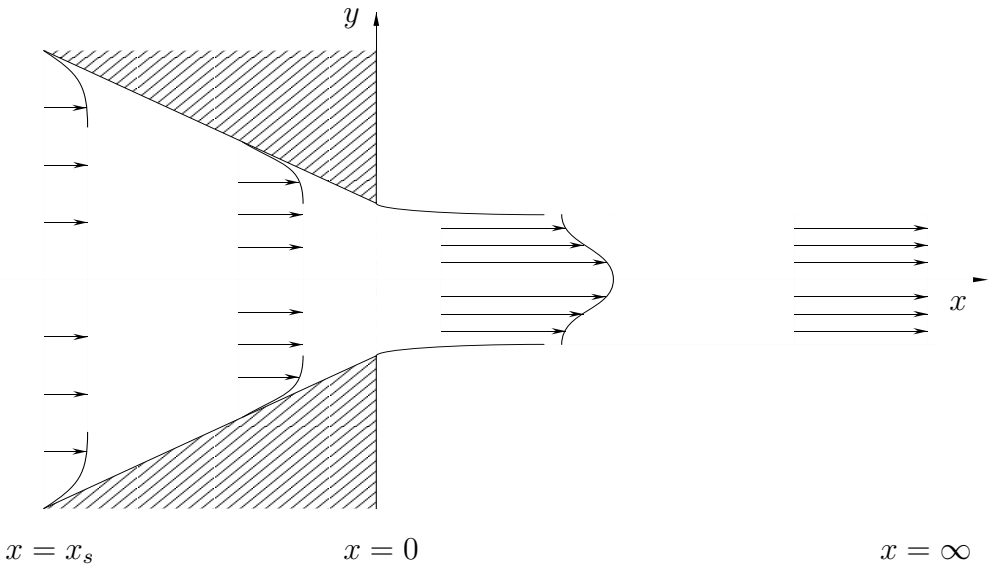

FIGURE 2.1. Principle of geometry and flow

y-direction as normal and the z-direction, (not shown in the figure), as spanwise to the jet.

The liquid in the jet and the ambient gas are separated by a surface upon which surface tension forces acts, and the location of this free surface is given by

$$\mathcal{H}(x, y, z, t) = y - h(x, z, t) = 0, \tag{3}$$

where $h(x, z, t)$ is unknown. To be able to determine h an equation has to be formulated which couples the velocity field and the location of the surface. The equation of motion for the free surface is given by the kinematic condition that a liquid particle on the surface always will remain there. This gives that

$$\frac{\partial \mathcal{H}}{\partial t} + u_i \frac{\partial \mathcal{H}}{\partial x_i} = 0.$$

By replacing $\mathcal{H}$ in this equation with the right hand side of eq. (3) this can be written as an equation for h,

$$\frac{\partial h}{\partial t} + u\frac{\partial h}{\partial x} + w\frac{\partial h}{\partial z} = v \quad \text{at} \quad y = h(x, z, t). \tag{4}$$

Hence the normal velocity of the surface is the same as the normal velocity v of a fluid element that exists there. This is true for the liquid in the jet as well as for the gas outside the jet,

$$\frac{\partial h}{\partial t} + u^{l,g}\frac{\partial h}{\partial x} + w^{l,g}\frac{\partial h}{\partial z} = v^{l,g} \quad \text{at} \quad y = h(x, z, t).$$

Here superscripts l and g denote the liquid and gas phase respectively, a notation that will be used in the following. If both phases are considered to be viscous there is a no-slip condition between the liquid and gas which gives that the velocities in all three directions have to be continuous across the free surface,

$$u_i^l = u_i^g \quad \text{at} \quad y = h(x, z, t). \tag{5}$$

This also implies that a derivative of any order of the primitive variables u_i or p, with respect to the streamwise or spanwise coordinates, x or z, are continuous across the surface. This can be seen from

$$\frac{d}{dx}u_i^{l,g}(x, h(x)) = \frac{\partial u_i^{l,g}}{\partial x} + \frac{dh}{dx}\frac{\partial u_i^{l,g}}{\partial h}$$

and since the last term is identical for both phases we obtain

$$\frac{\partial u_i^l}{\partial x} = \frac{\partial u_i^g}{\partial x}. \tag{6}$$

Together with the continuity equation this gives that

$$\frac{\partial v^g}{\partial y} = \frac{\partial v^l}{\partial y}, \quad \text{at} \quad y = h(x, z, t). \tag{7}$$

The body force in eq.(1) is considered since in any type of experimental set-up or practical application gravity will always be present and either bend or stretch the jet depending on the direction to which it is directed. If the jet is directed in

any other direction than vertical the stability of the jet will also be affected by gravity.

The gravity will only be taken into account to be able to compare experimental and numerical results. When gravity is considered it is assumed to be acting only in the streamwise direction of the jet, which is consistent with the experimental set-up,

$$\mathbf{f} = g\,\mathbf{e}_x.$$

2.1. Boundary conditions

The equations describing the flow of the liquid jet and ambient gas as well as the location of the free surface have to be complemented with appropriate boundary and initial conditions. In the converging channel the walls consist of solid surfaces which give no-slip conditions for the flow,

$$u = v = w = 0 \quad \text{at} \quad y = \pm y_w \quad x_s < x \leq 0.$$

For $x > 0$, *i.e.* for the free jet, boundary conditions must also be specified for the ambient gas away from the jet. Also conditions that describe the liquid-gas interface have to be formulated. The surface separating the liquid in the jet and the gas is subjected to pressure and viscous stresses from each of the phases. Also, the surface is influenced by surface tension effects. At the surface there has to be a force balance,

$$s_i^l - s_i^g = s_i^\gamma, \tag{8}$$

where $\mathbf{s} = s_i \mathbf{e}_i$ is the stress at the surface, see figure 2.2, and γ denotes the superficial forces.

The stresses from the liquid and gas are given by projecting the stress tensor for each fluid phase,

$$\sigma_{ij}^{l,g} = -p^{l,g}\delta_{ij} + \mu^{l,g}\left(\frac{\partial u_i^{l,g}}{\partial x_j} + \frac{\partial u_j^{l,g}}{\partial x_i}\right),$$

onto the normal of the surface, figure 2.2,

$$s_i^{l,g} = \sigma_{ij}^{l,g} n_j \tag{9}$$

where the normal is given by

$$\mathbf{n} = \frac{\nabla\,\mathcal{H}(x,y,z,t)}{|\nabla\,\mathcal{H}(x,y,z,t)|} = \left(-\frac{\partial h}{\partial x}, 1, -\frac{\partial h}{\partial z}\right)|\nabla\,\mathcal{H}(x,y,z,t)|^{-1}, \tag{10}$$

and

$$|\nabla\,\mathcal{H}(x,y,z,t)| = \left(1 + \left(\frac{\partial h}{\partial x}\right)^2 + \left(\frac{\partial h}{\partial z}\right)^2\right)^{\frac{1}{2}}.$$

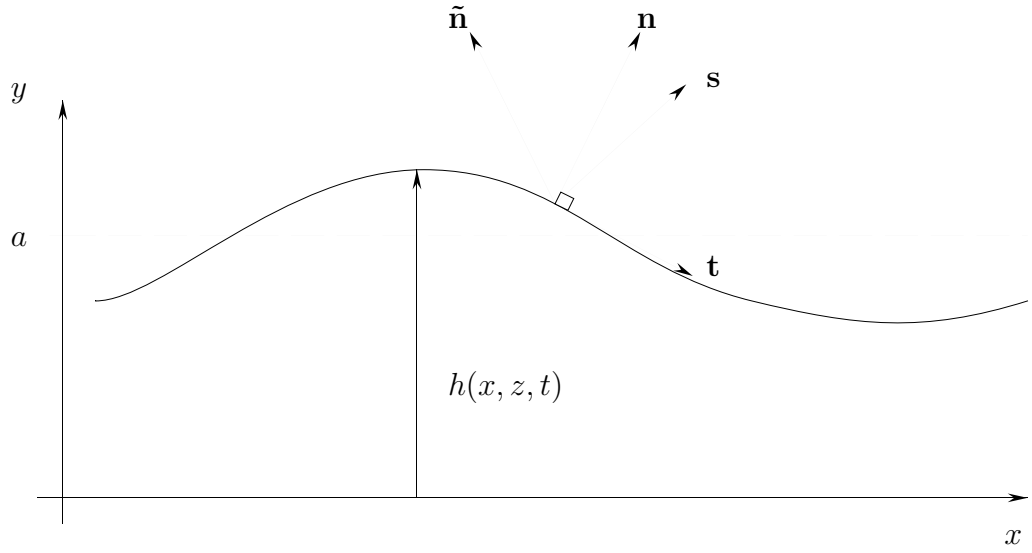

FIGURE 2.2. Definition of vectors on the free surface.

The surface is assumed to have an infinitesimal thickness and the jump in stress due to surface tension is a vector given by,

$$s_i^\gamma = \gamma(\frac{1}{R_x} + \frac{1}{R_z})n_i = \gamma\frac{\partial n_j}{\partial x_j}n_i,$$

where γ is the coefficient of surface tension, R_x and R_z are the radiia of curvature in the xy- and yz-plane respectively. This gives three conditions at the surface, $i = 1, 2, 3$,

$$-(p^l - p^g)\delta_{ij}n_j + \mu^l(\frac{\partial u_i^l}{\partial x_j} + \frac{\partial u_j^l}{\partial x_i})n_j - \mu^g(\frac{\partial u_i^g}{\partial x_j} + \frac{\partial u_j^g}{\partial x_i})n_j = \gamma\frac{\partial n_j}{\partial x_j}n_i. \qquad (11)$$

Because of the definition of the normal to the free surface, eq. (10), these three conditions are all non-linear.

If the equations are restricted to a two-dimensional formulation in the xy-plane, these boundary conditions will look like

$$-(p^l - p^g)n_x + 2(\mu^l - \mu^g)\frac{\partial u^l}{\partial x}n_x + \left(\mu^l\frac{\partial u^l}{\partial y} - \mu^g\frac{\partial u^g}{\partial y}\right)n_y + (\mu^l - \mu^g)\frac{\partial v^l}{\partial x} = \gamma\left(\frac{\partial n_x}{\partial x} + \frac{\partial n_y}{\partial y}\right)n_x,$$

$$-(p^l - p^g)n_y + 2(\mu^l - \mu^g)\frac{\partial v^l}{\partial y}n_y + \left(\mu^l \frac{\partial u^l}{\partial y} + \mu^g \frac{\partial u^g}{\partial y}\right) n_x + (\mu^l - \mu^g)\frac{\partial v^l}{\partial x}n_x = \gamma \left(\frac{\partial n_x}{\partial x} + \frac{\partial n_y}{\partial y}\right) n_y.$$

where the conditions for continuous velocity at the surface have been used, eqs. (5)-(7). To simplify these the definition of the normal to the surface, eq. 10, is used

$$(p^l - p^g)h_x - 2(\mu^l - \mu^g)\frac{\partial u^l}{\partial x}h_x + \left(\mu^l \frac{\partial u^l}{\partial y} - \mu^g \frac{\partial u^g}{\partial y}\right) + (\mu^l - \mu^g)\frac{\partial v^l}{\partial x} = \gamma \frac{d}{dx}\left(\frac{h_x}{\sqrt{1+h_x^2}}\right) h_x,$$

$$-(p^l - p^g) + 2(\mu^l - \mu^g)\frac{\partial v^l}{\partial y} - \left(\mu^l \frac{\partial u^l}{\partial y} + \mu^g \frac{\partial u^g}{\partial y}\right) h_x - (\mu^l - \mu^g)\frac{\partial v^l}{\partial x}h_x = -\gamma \frac{d}{dx}\left(\frac{h_x}{\sqrt{1+h_x^2}}\right).$$

The tangential shear on the surface is obtained if the stress, $\mathbf{s}$, is projected onto the tangent to the surface $\mathbf{t} = (n_y, -n_x)$,

$$\mathbf{t} \cdot (\mathbf{s}^l - \mathbf{s}^g - \mathbf{s}^\gamma) = 0.$$

This gives

$$4(\mu^l - \mu^g)\frac{\partial v^l}{\partial y}h_x + \left\{\mu^l \frac{\partial u^l}{\partial y} - \mu^g \frac{\partial u^g}{\partial y}\right\}(1 - h_x^2) + (\mu^l - \mu^g)\frac{\partial v^l}{\partial x}(1 - h_x^2) = \gamma \frac{d}{dx}\left(\frac{h_x}{\sqrt{1+h_x^2}}\right) h_x, \quad (12)$$

Then the stresses are projected onto $\tilde{\mathbf{n}} = (n_x, -n_y)$, figure 2.2,

$$\tilde{\mathbf{n}} \cdot (\mathbf{s}^l - \mathbf{s}^g - \mathbf{s}^\gamma) = 0,$$

which gives

$$(p^l - p^g)(1 - h_x^2) + 2(\mu^l - \mu^g)\frac{\partial u^l}{\partial x}(1 + h_x^2) = \gamma \frac{d}{dx}\left(\frac{h_x}{\sqrt{1+h_x^2}}\right)(1 - h_x^2). \quad (13)$$

These new boundary conditions, eqs. (12) and (13), show that the ambient gas only enters through the pressure and the first normal derivative of the streamwise velocity.

The remaining boundary conditions are obtained from the assumption that the flow is symmetric with respect to the centreline of the channel and jet.

$$\frac{\partial u}{\partial y} = 0, \quad v = 0, \quad \frac{\partial p}{\partial y} = 0 \quad \text{at} \quad y = 0.$$

2.2. Flow of the surrounding gas

The flow of the surrounding gas depends on the geometry outside the jet. In order to investigate the effect of a viscous gas without making assumptions about the geometry and without having to solve the flow for the gas phase an approximate explicit expression for the tangential shear of the gas phase on the surface of the jet is assumed.

To estimate the friction of the gas the solution to Stokes first problem, the infinite starting plate (see *e.g.* Schlichting (1979)), is used,

$$u^g = u_{surface}(1 - \operatorname{erf}\eta), \quad \text{where} \quad \eta = (y-a)/(\nu^g t)^{\frac{1}{2}}, \tag{14}$$

where $u_{surface}$ is the streamwise velocity of the surface of the jet. From this expression the tangential shear at the free surface in the streamwise direction is given by

$$\sigma = \mu^g \frac{\partial u_g}{\partial y} = -\mu^g u_{surface}(\pi\nu^g t)^{-\frac{1}{2}}. \tag{15}$$

where ν^g is the kinematic viscosity of the gas. The tangential shear is a function of time, t, but can be converted into a downstream distance by

$$t = U_m x.$$

With this substituted for t in eq. (15) the shear at a position x of the surface is given by

$$\sigma = -\mu^g u_{surface}(\frac{U_m}{\pi\nu^g x})^{\frac{1}{2}}.$$

This assumption for shear is considered only since an exact solution of the flow field in the gas outside of the jet depend on the far field conditions for the gas, and, when performing the stability analysis the analytical solution provides an easy access to the velocity distribution in the gas.

2.3. Scaling of the governing equations

In the following we will express the equations in non-dimensional form. The reference length is defined as the half channel height, a, at the exit $x = 0$ and the reference velocity is defined from the flow rate Q through the nozzle, $U_m = Q/a$. This will give U_m as the mean velocity at the exit, $x = 0$. These are introduced in eq. (1) for both phases and give the following non-dimensional form of the momentum equation

$$\frac{\partial \tilde{u}_i}{\partial t} + \tilde{u}_k \frac{\partial \tilde{u}_i}{\partial \tilde{x}_k} = -\frac{\partial \tilde{p}^{l,g}}{\partial \tilde{x}_i} + \frac{1}{Re^{l,g}} \frac{\partial^2 \tilde{u}_i}{\partial \tilde{x}_k \partial \tilde{x}_k} + \frac{1}{Fr^2}, \tag{16}$$

and the continuity equation

$$\frac{\partial \tilde{u}_i}{\partial \tilde{x}_i} = 0, \tag{17}$$

where the velocity vector, pressure and derivatives in non-dimensional form are given by

$$\tilde{u}_i = \frac{u_i}{U_m}, \quad \tilde{p}^{l,g} = \frac{p}{\rho^{l,g} U_m^2} \quad \text{and} \quad \frac{\partial}{\partial \tilde{x}_i} = \frac{1}{a}\frac{\partial}{\partial x_i}.$$

The Reynolds number, $Re^{l,g}$, and the Froude number, Fr, are defined as

$$Re^{l,g} = \rho^{l,g} U_m a / \mu^{l,g} \quad \text{and} \quad Fr = U_m/(ag)^{\frac{1}{2}}.$$

As the Froude number is independent of density and viscosity, it is the same in the momentum equations for both liquid and gas while for the Reynolds number the relation is given by

$$Re^g = \frac{\tilde{\rho}}{\tilde{\mu}} Re^l,$$

where $\tilde{\rho} = \rho^g/\rho^l$ is the density ratio and $\tilde{\mu} = \mu^g/\mu^l$ is the ratio of the dynamic viscosities. This also gives that

$$\tilde{p}^l = \tilde{\rho}\, \tilde{p}^g,$$

if the unscaled pressure p is the same in both liquid and gas.

The scaling of the no-slip and symmetry boundary conditions is trivial while the conditions for the liquid-gas interface, (12) and (13), are divided by $\mu^l U_m/a$ and $\rho^l U_m^2/a$ respectively. This gives

$$4(1-\tilde{\mu})\frac{\partial \tilde{v}^l}{\partial y} h_x + \left\{ \frac{\partial \tilde{u}^l}{\partial y} - \tilde{\mu}\frac{\partial \tilde{u}^g}{\partial y} \right\}(1-h_x^2) + (1-\tilde{\mu})\frac{\partial \tilde{v}^l}{\partial x}(1-h_x^2) = \frac{1}{We}\frac{d}{dx}\left(\frac{h_x}{\sqrt{1+h_x^2}}\right) h_x, \quad (18)$$

$$(\tilde{p}^l - \tilde{\rho}\tilde{p}^g)(1-h_x^2) + \frac{2}{Re^l}(1-\tilde{\mu})\frac{\partial \tilde{u}^l}{\partial x}(1+h_x^2) = \frac{1}{We}\frac{d}{dx}\left(\frac{h_x}{\sqrt{1+h_x^2}}\right)(1-h_x^2). \quad (19)$$

where $We = \rho^l U_m^2 a/\gamma$ is the Weber number. There is no need to introduce a scaling of the normal of the surface since $h_x = \tilde{h}_{\tilde{x}}$.

The explicit expression for the shear in the gas phase at the surface can be scaled to give,

$$\frac{\partial \tilde{u}}{\partial \tilde{y}} = -\tilde{u}_{surface}\left(\frac{U_m a}{\pi \nu^g}\frac{1}{\tilde{x}}\right)^{\frac{1}{2}} = -\tilde{u}_{surface}\left(\frac{Re^g}{\pi \tilde{x}}\right)^{\frac{1}{2}}.$$

2.4. Inlet and outlet conditions

The upstream conditions depend on the geometry of the nozzle. One could think of a vast amount of different designs. Even for the plane channel the upstream conditions are not simple, but could take various forms.

2.4.1. Channel nozzle. Far upstream, *i.e.* $x \ll 0$, the flow is entering a plane channel with a uniform velocity distribution. The flow then starts to develop and if the channel is long enough the result will be the well known case of plane Poiseuille flow. This developing flow has been described by Schlichting (1979) and gives the inlet length, ℓ_E, for fully developed Poiseuille flow as a linear function of Reynolds number,

$$\ell_E = 0.16aRe$$

where Re is the Reynolds number based on half channel height a and mean velocity U_m. The validity of this expression for high Reynolds numbers is discussed by Van Dyke (1970).

The liquid jet should also satisfy a global momentum- and mass conservation, see appendix A.

2.4.2. Slit nozzle. The flow through a slit nozzle is assumed to be well described by inviscid theory. This assumption is made based on the boundary layer solution to the flow in a convergent channel, figure 2.3. The slit nozzle is replaced by a convergent channel where the nozzle edges are positioned at $x = a$. The boundary layer thickness, δ, at this position would then be $\delta = 3a(Re^l)^{-\frac{1}{2}}$. At $Re = 2000$ this gives $\delta \approx a/15$, which means that the effect of viscosity is limited to a region close to the wall and for an inviscid jet the fluid is accelerating close to the nozzle edges, see *e.g.* Söderberg (1994).

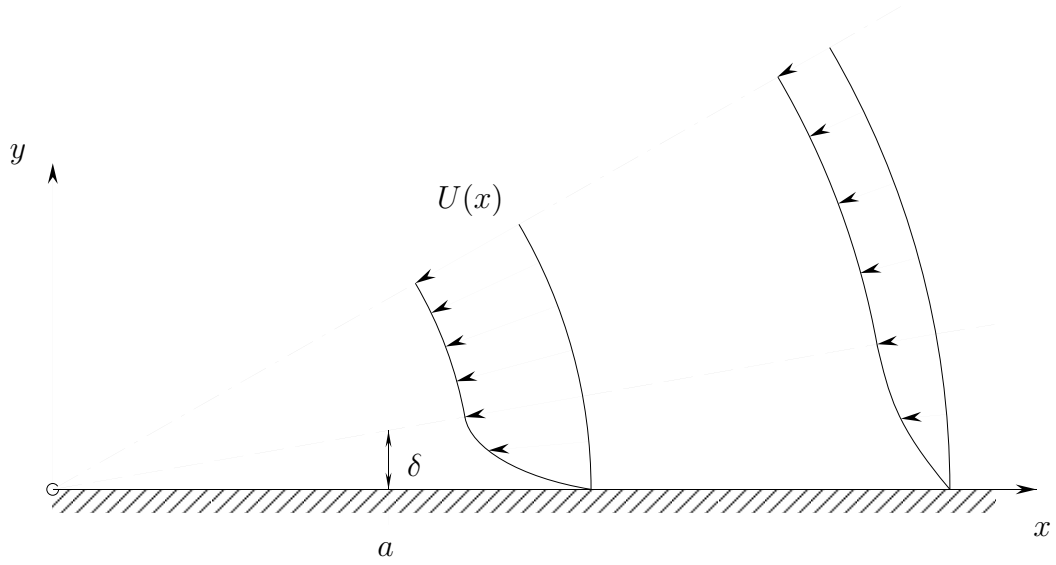

FIGURE 2.3. The flow in a converging channel where the origo is considered to be a sink and $U(x)$ is the potential solution to the problem, (inviscid irrotational flow).

CHAPTER 3

Numerical solution of basic flow

The basic flow of a plane liquid jet is assumed to be independent of the spanwise coordinate z and therefore considered to be well described by the two-dimensional Navier-Stokes equations[1]. Further assumptions are that the flow is laminar and steady. Also, the flow is assumed to be symmetric with respect to the yz-plane.

The equations (16) and (17) are solved by the method of finite differences. A solution is sought in the domain bounded by

$$x_s \leq x \leq x_\infty,$$

in the streamwise direction, and

$$\begin{aligned} 0 \leq y \leq y_w \quad &\text{for} \quad x_s < x \leq x_\infty, \\ 0 \leq y \leq h(x) \quad &\text{for} \quad 0 < x \leq x_\infty, \end{aligned}$$

in the normal direction. Here x_∞ is set to be a point far downstream of the nozzle where the flow is assumed to be parallel. The equations are solved for the primitive variables u, v and p. The domain is partly bounded by the free surface, which is unknown, and therefore the calculation has been made on an adaptive grid. This means that a new grid has to be generated everytime the location of the free surface changes in physical space. The surface will always coincide with a part of the top boundary in the computational domain, which will give a well defined surface as a part of the solution.

The transform that will map the physical domain onto the computational is given by

$$\xi = \xi(x, y) \quad \text{and} \quad \eta = \eta(x, y).$$

These variables represent a conformal transformation and satisfy the Laplace equation

$$\xi_{xx} + \xi_{yy} = 0 \quad \text{and} \quad \eta_{xx} + \eta_{yy} = 0,$$

and the Cauchy-Riemann conditions

$$\xi_x = \eta_y \quad \text{and} \quad \xi_y = -\eta_x.$$

[1] In the following all equations will be given in non-dimensional form, except where otherwise stated.

If these variables are introduced into equations (16) and (17), the following transformed equations are obtained

$$U^C\frac{\partial u}{\partial \xi}+V^C\frac{\partial u}{\partial \eta} = -(\frac{\xi_x}{J}\frac{\partial p}{\partial \xi}+\frac{\eta_x}{J}\frac{\partial p}{\partial \eta})+\frac{1}{Re}(\frac{\partial^2 u}{\partial \xi^2}+\frac{\partial^2 u}{\partial \eta^2}) \quad (20)$$

$$U^C\frac{\partial v}{\partial \xi}+V^C\frac{\partial v}{\partial \eta} = -(\frac{\xi_y}{J}\frac{\partial p}{\partial \xi}+\frac{\eta_y}{J}\frac{\partial p}{\partial \eta})+\frac{1}{Re}(\frac{\partial^2 v}{\partial \xi^2}+\frac{\partial^2 v}{\partial \eta^2}) \quad (21)$$

$$\frac{\partial U^C}{\partial \xi}+\frac{\partial V^C}{\partial \eta} = 0, \quad (22)$$

where the assumption of a steady flow has been used. Here J is the determinant of the Jacobian matrix, $\mathbf{J}$, of the transformation,

$$\mathbf{J}=\begin{bmatrix}\xi_x & \xi_y\\ \eta_x & \eta_y\end{bmatrix} \Rightarrow J=|\mathbf{J}|=\xi_x\eta_y-\xi_y\eta_x.$$

U^C and V^C are velocities in the transformed coordinate system in the ξ and η directions, respectively, given by

$$U^C=(\xi_x u+\xi_y v)/J \quad \text{and} \quad V^C=(\eta_x u+\eta_y v)/J.$$

A conformal transformation is by definition also orthogonal and has several advantages compared to a non-conformal transformation. The grid related parameters are limited and second derivatives of transform variables, ξ and η, are not present in the equations. These may otherwise degrade the accuracy of the solution if the grid is distorted. The transform coordinates can also be interpreted as representing the potential and streamfunction, of an inviscid irrotational flow in the geometry prescribed by the walls, centreline and free surface.

An adaptive conformal grid requires the Laplace equation for the transform variables to be solved repeatedly. Since this is done numerically sharp corners can give a grid where internal vertices ends up outside the physical domain. The flow of the ambient gas was not calculated but instead treated explicitly by the approximation introduced in section 2.2.

3.1. Boundary conditions

In order to solve the transformed equations the boundary conditions has to be transformed too. The no-slip conditions at the wall, eq. (2.1), will not be affected by this,

$$u=v=0 \quad \text{at} \quad y=y_w.$$

At the centreline the x and ξ coordinates are parallel, *i.e.* $\xi_y=0$, we obtain

$$\frac{\partial p}{\partial y}=\xi_y\frac{\partial p}{\partial \xi}+\eta_y\frac{\partial p}{\partial \eta}=\eta_y\frac{\partial p}{\partial \eta}$$

Hence

$$\frac{\partial p}{\partial \eta} = 0 \quad \text{at} \quad y = \eta = 0.$$

which is also true for the streamwise velocity u. The conditions at the centreline then becomes

$$\frac{\partial u}{\partial \eta} = 0, \quad v = 0, \quad \text{and} \quad \frac{\partial p}{\partial \eta} = 0 \quad \text{at} \quad \eta = 0. \tag{23}$$

The condition for the stresses at the surface, eq. (11), contains several derivatives of the transformation variables. The expressions becomes more complicated and are implemented as is. The velocity normal to the surface is parallel to the η direction in the computational domain. This gives

$$V^C = 0 \quad \text{at} \quad \eta = 1. \tag{24}$$

This can be set in a more useful form with the aid of the transformed continuity equation (see eq. 22), which can be integrated in the η direction. Together with eq. (24) this results in an integral expression,

$$\int_0^1 \left(\frac{\partial U^C}{\partial \xi} + \frac{\partial V^C}{\partial \eta} \right) d\eta = \int_0^1 \frac{\partial U^C}{\partial \xi}\, d\eta + V^C\Big|_{\eta=1} - V^C\Big|_{\eta=0} = \frac{\partial}{\partial \xi} \int_0^1 U^C\, d\eta = 0$$

$$\Rightarrow \quad \int_0^1 U^C\, d\eta = \text{constant}.$$

This replaces the kinematic condition at the free surface. Totally there are six conditions. Five of these are needed to solve the equations of motion and one to find the location of the free surface.

3.2. Discretization

The equations (20)-(22), are discretized by the method of finite differences. The computational domain is rectangular and the grid equidistant, figure 3.1. The dependent variables u, v and p are evaluated at the same point. Since the conformal transformation gives the potential flow in the geometry prescribed by the wall, centreline and free surface, the viscous and inviscid flowfields are assumed to be similar, if the streamfunction is considered. Hence the flow will be close to parallel in the computational domain. All second derivatives are represented with central differences and the first order derivatives by a mixed upwind-central difference scheme in order to prevent non-physical oscillations in the solution. The discretizations of the derivatives at the node j, k are given by

$$\left[\frac{\partial u}{\partial \xi}\right]_{j,k} = \frac{1}{2\Delta\xi}(u_{j+1,k} - u_{j-1,k}) + \frac{q}{3\Delta\xi}(-u_{j+1,k} + 3u_{j,k} - 3u_{j-1,k} + u_{j-2,k})$$

$$\left[\frac{\partial^2 u}{\partial \xi^2}\right]_{j,k} = \frac{1}{\Delta\xi^2}(u_{j+1,k} + 2u_{j,k} - u_{j-1,k})$$

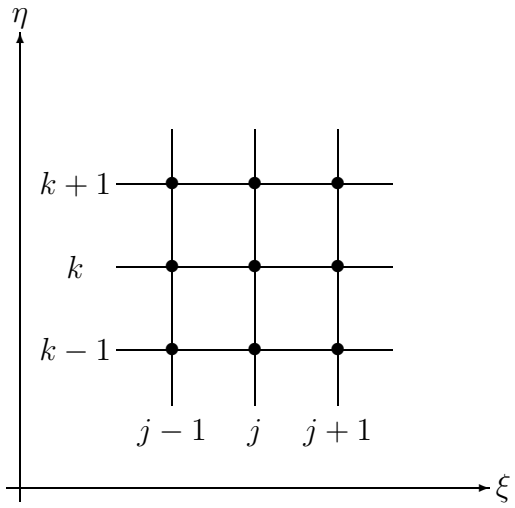

FIGURE 3.1. Gridpoints in computational domain.

q	$\left[\frac{\partial u}{\partial \xi}\right]_{j,k}$	error	type
0	$(u_{j+1,k} - u_{j-1,k})/2\Delta\xi$	$\mathcal{O}(\Delta\xi^2)$	central
0.375	$(3u_{j+1,k} + 3u_{j,k} - 7u_{j-1,k} + u_{j-2,k})/8\Delta\xi$	$\mathcal{O}(\Delta\xi^2)$	QUICK
0.5	$(2u_{j+1,k} + 3u_{j,k} - 6u_{j-1,k} + u_{j-2,k})/6\Delta\xi$	$\mathcal{O}(\Delta\xi^3)$	third order
1.5	$(3u_{j,k} - 4u_{j-1,k} + u_{j-2,k})/2\Delta\xi$	$\mathcal{O}(\Delta\xi^2)$	upwind

FIGURE 3.2. Dependence of q.

The parameter q is continuously variable in the interval, $0 \leq q \leq 1.5$. It is used to control the degree of upwind discretization. Some examples of discretizations can be found in table (3.2). All choices of q produces a scheme where the error is of second order except for the case $q = 0.5$, when the scheme will be of third order.

3.3. Solution method

The discretized equations (20)-(22), are solved by an iterative method, which can be described by figure (3.3). First the initial grid is calculated. This is done by using the location of the free surface given by the solution to the flow of a potential jet. The initial guess for the flow is also taken from this solution. Starting with this initial guess the equations are solved implicitly in the η-direction starting at the upstream boundary, $j = 3$. The first two ξ positions are determined by the choice of inlet conditions. If, for example a plane channel with fully developed

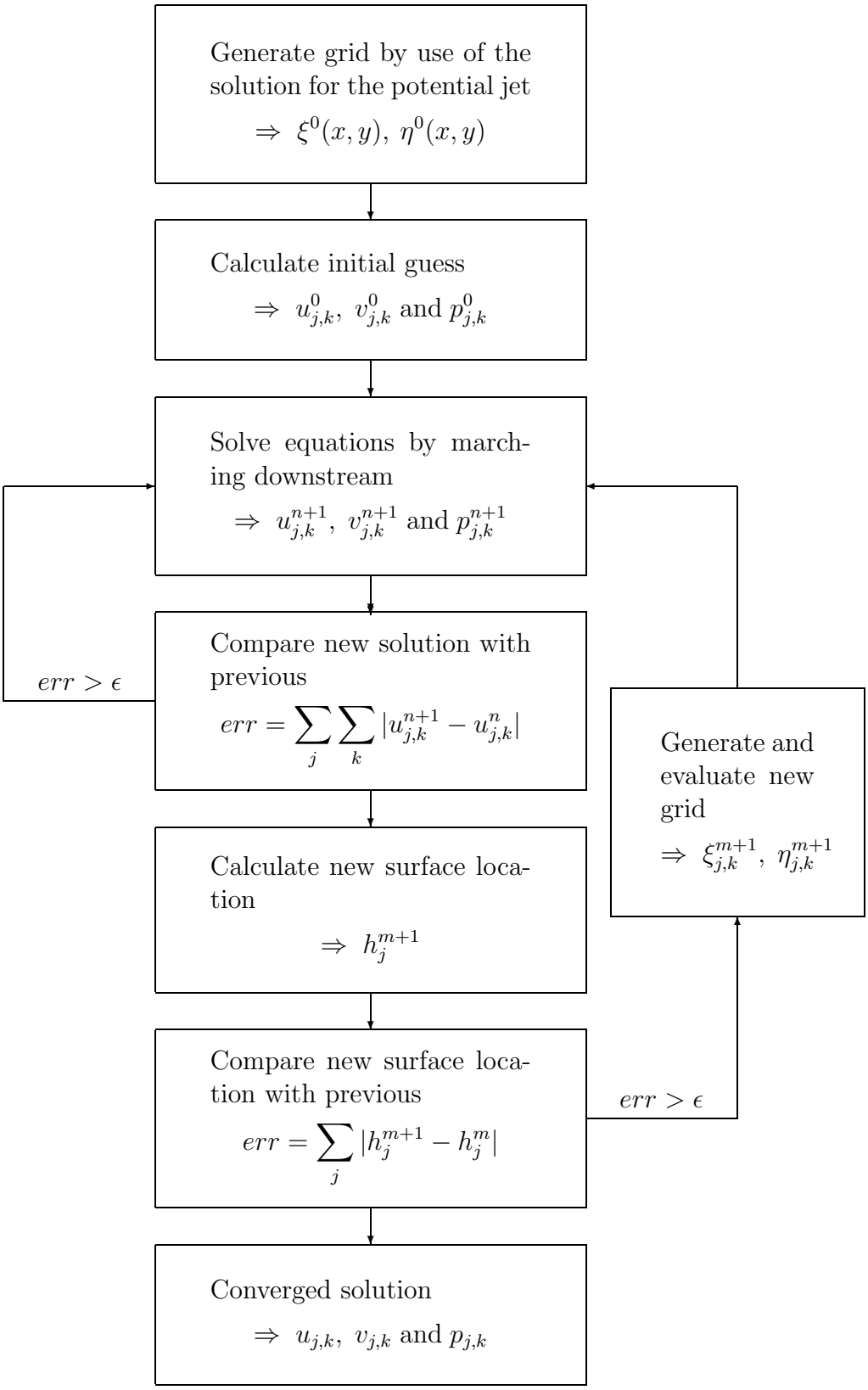

FIGURE 3.3. Solution method

flow is investigated, the velocity distribution in the η-direction is the same for both points, which is equal to setting $v = 0$ as a boundary condition. At the centreline the boundary conditions (23), are specified at all streamwise positions, whereas inside the nozzle the zero velocity conditions are used at the wall. When the equations are solved for the flow outside the jet the conditions (24) and (18) are used instead of the no-slip conditions.

The flow is solved iteratively with QUICK differencing, table 3.2, and subsequent downstream marches and underrelaxation, see *e.g.* Fletcher (1991). During these iterations the free surface is fixed and when the solution is sufficiently converged the location of the surface is corrected with the aid of the remaining boundary condition eq. (4). After correcting the location of the surface the Laplace equations for the transform variables are solved and derivatives of the transform variables re-evaluated. This iterative procedure is repeated until the solution is sufficiently converged.

3.4. Results for the basic flow

Calculations have been performed by the method described in the previous section. The aim has been to provide some insight in the flow of plane liquid jets. Also these calculations provide basic velocity distributions for stability calculations. The liquid jet is emanating from a plane channel with an upstream parabolic velocity distribution, *i.e.* plane Poiseuille flow. Calculations were made for the case of a jet flowing into vacuum, and the effect of a not fully developed flow in the channel was examined. Also, calculations were made to study the effect of a viscous ambient gas and gravity acting in the streamwise direction.

3.4.1. Channel flow. The outflow from a plane channel with an upstream fully developed Poiseuille flow can be seen in figure 3.4. The figure shows the velocity distribution at several downstream positions for both the u and v components. The v velocity is several orders of magnitude smaller the u velocity and is therefore multiplied by a factor of 500. The u profile at $x = -40$ represents the upstream boundary condition, the perfect parabola obtained in a plane Poiseuille flow. The normal velocity at this point is identically zero. These conditions are constant throughout the channel. The effect of the downstream nozzle appears within one channel height from the exit. At the next position, $x = 0$ the profile represents the end of the channel, *i.e.* the nozzle edge. Here the streamwise velocity distribution has changed. The centreline velocity has decreased slightly and the profile is wider. This can also be seen by examination of the normal velocity distribution at the same point. This shows that fluid is transported from the centreline towards the walls. At the walls however, the normal velocity is directed towards the centre of the channel. When the fluid leaves the channel the boundary condition will change from no-slip to no-shear which will result in an acceleration of the fluid at the surface. The acceleration is highest directly after the nozzle edge after

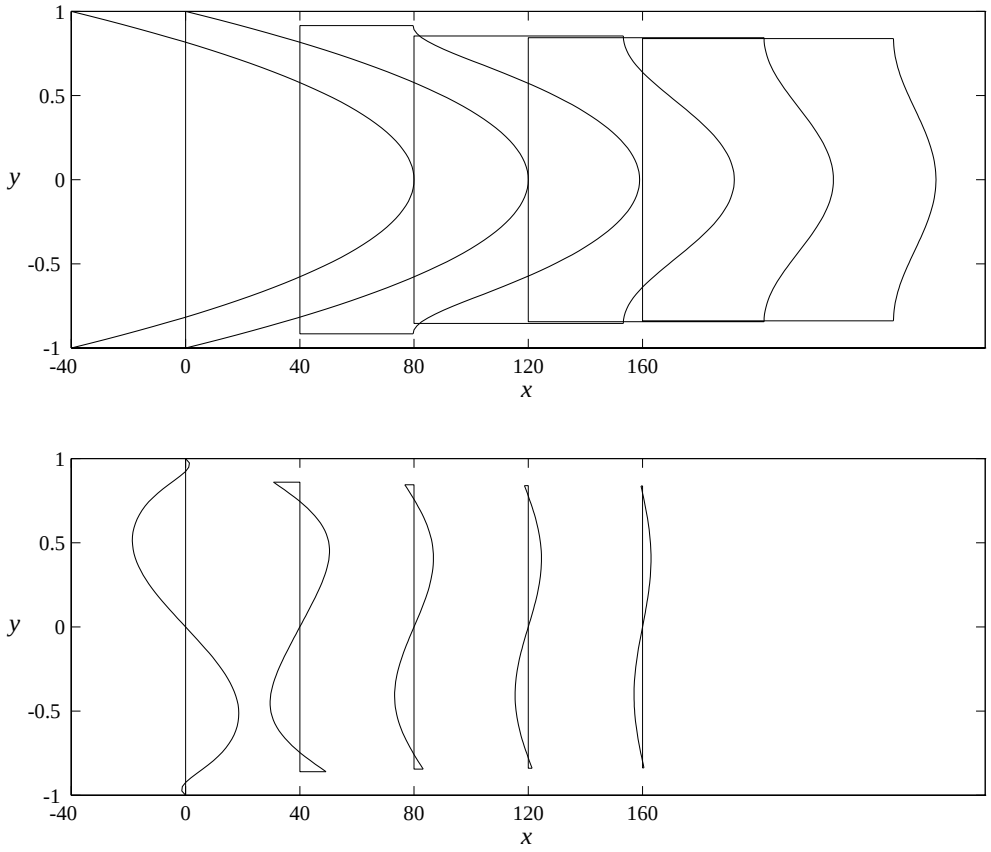

FIGURE 3.4. Velocity profile relaxation, $Re = 1000$, $1/We = 0$, $\tilde{\rho} = 0$ and $\tilde{\mu} = 0$. u-velocity (top) and v-velocity (bottom). v is here scaled up 500 times compared to u

which it decays. At $x = 40$ the streamwise velocity at the surface is $0.8\,U_m$, and the jet has undergone a contraction. This contraction is a consequence of the conservation of momentum and mass flow. Also, this profile has inflexion points. The profiles at positions further downstream are all similar to this.

In figure 3.5 both velocity components have been plotted against the η- and the y-coordinates. The left part of each graph shows the velocity plotted against the computational coordinate η. This clearly shows how the relaxation seems to occur with the two points at $\eta = \pm 0.48$ as fixed for positions downstream of the nozzle. The right part shows the velocity plotted against the 'real' coordinate y. Also in this figure the v-velocity has been scaled up 500 times.

In figure 3.6 the streamwise velocity at the surface and centreline of the jet is plotted against the scaled coordinate x/Re for a range of Reynolds numbers. Also the location of the free surface is plotted in this figure.

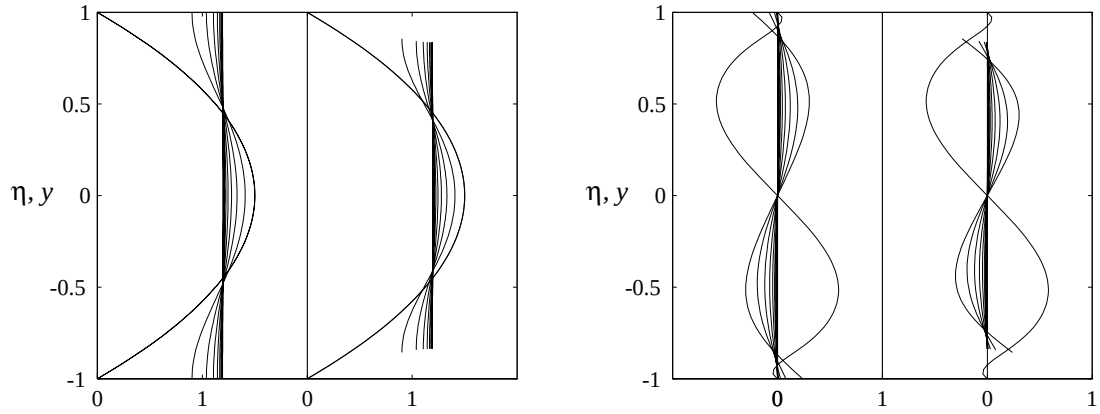

FIGURE 3.5. Velocity profile relaxation u (left) and v (right). Plotted against η and y, (left and right in each graph).

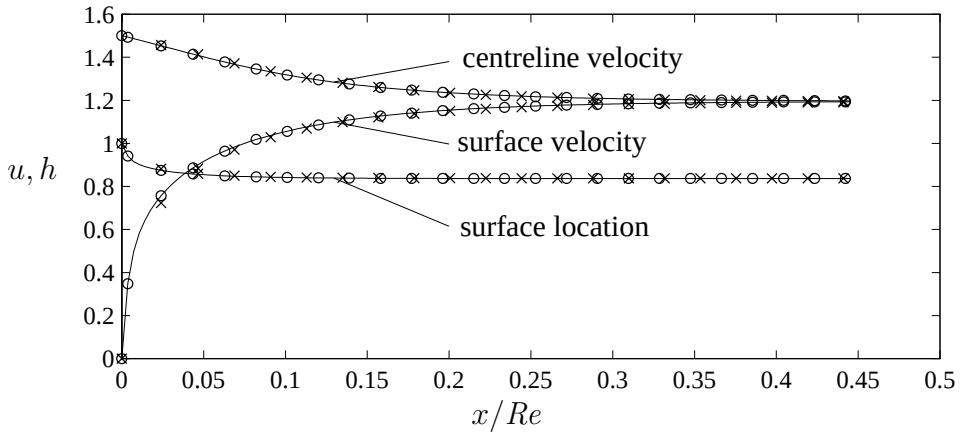

FIGURE 3.6. Velocity at the centreline and surface as well as the location of the free surface. (∘) $Re = 100$, (×) $Re = 1000$; (—) $Re = 10000$, $\tilde{\rho} = 0$ and $\tilde{\mu} = 0$.

In section 2.4.1 the entrance length, ℓ_E, for developing channel flow was discussed, and it scales as x/Re. A relaxation length, ℓ_R, for the channel jet can also be found from figure 3.6. If defining ℓ_R as the length from the edge of the channel to the downstream location where $|u_{surface} - u_{CL}| < 0.01$, then

$$\ell_R = 0.36\, xRe.$$

This figure also shows that the distance to reach the final jet thickness is considerably shorter than the time it takes for the velocity to reach uniformity, the difference is approximately a factor of five.

Calculations have also been performed with profiles at the nozzle edge that deviates from the parabolic. These were obtained by starting the calculation with

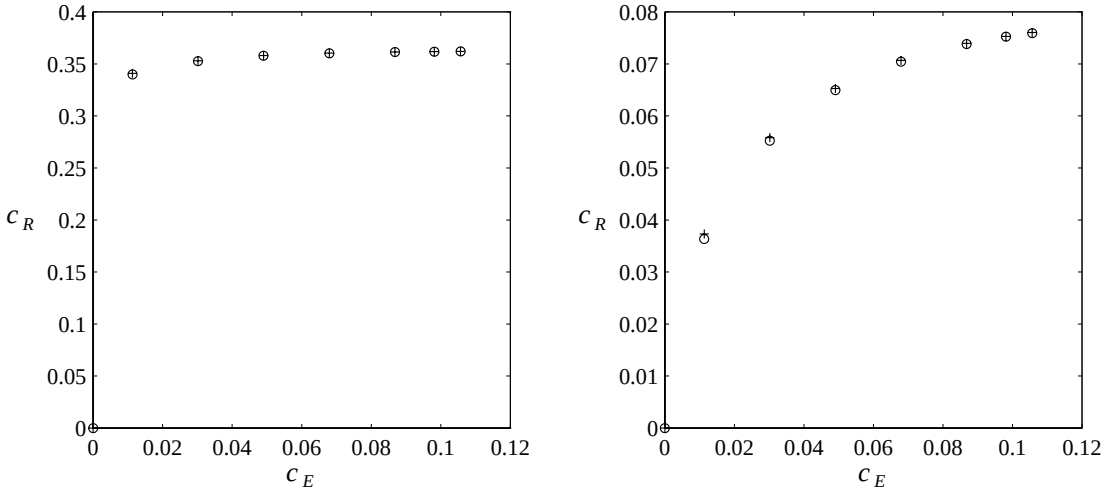

FIGURE 3.7. Relaxation length as a function of entrance length for the velocity profile, (left), and surface location (right). ($\circ$) $Re = 1000$; ($+$) $Re = 10000$, $\tilde{\rho} = 0$ and $\tilde{\mu} = 0$.

a uniform velocity distribution at the upstream boundary. The inlet length ℓ_E and the relaxation length ℓ_R are defined as

$$\ell_E = c_E \, aRe$$
$$\ell_R = c_R \, aRe$$

respectively, where a is half the channel height. The inlet length was then varied for two different Reynolds numbers, $Re = 1000, 10000$. Thus for each inlet length there is one corresponding relaxation length $\ell_R = f(\ell_E)$. The results can be seen in figure 3.7. The left graph contains the result for the relaxation of the velocity profile and the right graph contains the relaxation of the free surface. In both graphs the scaling with the Reynolds number seems to be applicable too. However, the relaxation length for the velocity is only changing slightly, while the length for the surface changes more clearly. The points for $c_E = 0$ are not calculated but assumed to be valid since if there is no channel there will be no change to the uniform velocity profile.

If, in a real flow situation, the jet is directed downwards, gravity will cause an acceleration of the fluid in the jet. Figure 3.8 shows the result for a jet, where the Froude number was kept constant, $Fr = 20$, and the Reynolds number was varied. This corresponds to changing the viscosity of the liquid and keeping channel height and velocity constant. As the figure shows a low Reynolds number means that the effect of gravity during the relaxation process is small, this since the length

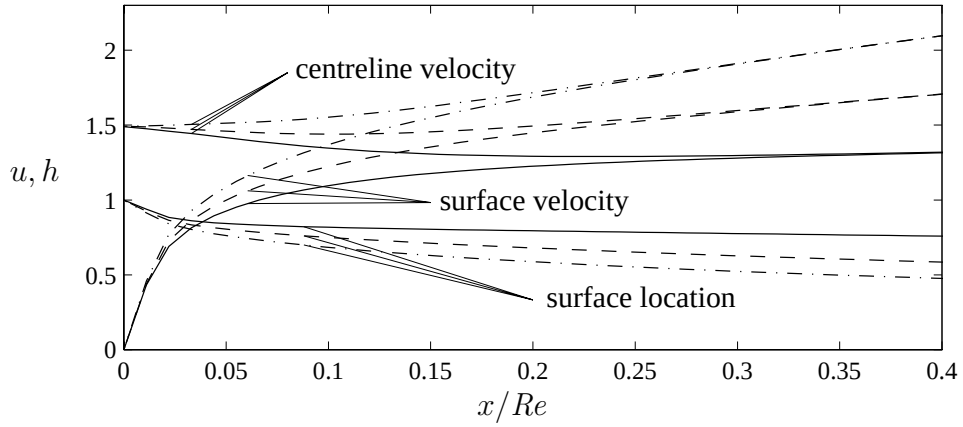

FIGURE 3.8. Velocity at centreline and surface, $Fr = 20$. (solid) $Re = 100$; (dotted) $Re = 500$; (dash-dotted) $Re = 1000$

between the nozzle and end of relaxation is longer when the Reynolds number is increased. Thus, assuming that the velocity is the same for two liquid jets with different viscosity, the time for the gravity to act is shorter for the liquid with highest viscosity, *i.e.* lowest Reynolds number.

Up to this point the ambient gas has been assumed to be inviscid. Clearly viscosity will affect the flow of the jet, since this will create a shear, *i.e.* drag, on the surface. In figure 3.9 results are shown for a constant Reynolds number for the jet with $\tilde{\mu}$ varying. This figure shows that an increase of the viscosity of the gas causes the jet to expand downstream. Also the velocity in the jet decreases. The effect becomes more and more dominant when the viscosity ratio is increased. The asymptotic behaviour of the jet will be dictated by the assumption made for the flow of the ambient gas. For a ratio comparable to a water jet emanating into the air the effect of a viscous ambient gas is very small in the relaxation region, *i.e.* from the end of the channel to ℓ_R.

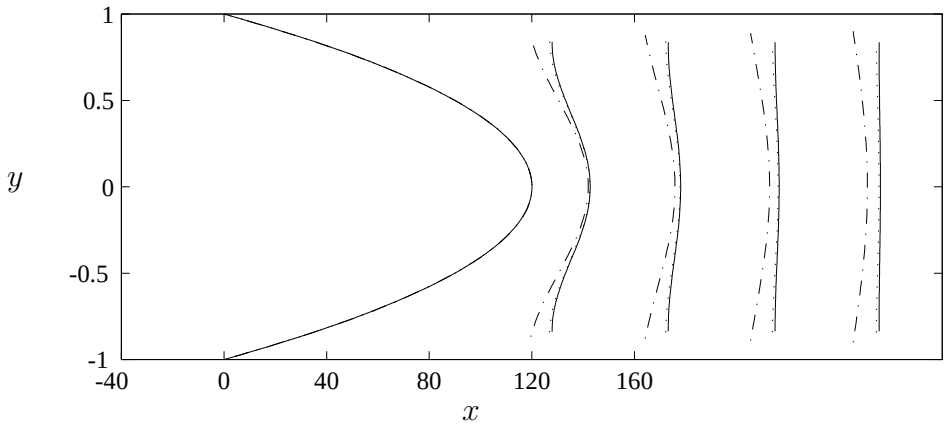

FIGURE 3.9. Velocity profile for $Re = 1000$. (solid) $\tilde{\mu} = 0.01$; (dotted) $\tilde{\mu} = 0.1$; (dash-dotted) $\tilde{\mu} = 10$. Positions for profiles, from left to right are $x = 0$, 40, 80, 120, 160.

CHAPTER 4

Linear stability

Linear stability theory is often used as a tool to predict the transition from laminar to turbulent flow. The idea is to subject a laminar flow to a small, *i.e.* infinitesimal, perturbation and investigate if the disturbance grows in time and/or space. Also the stability of the plane liquid jet can be examined in this way.

The present flow visualization results of plane liquid jets emanating from the plane channel flow nozzle, clearly show waves on the surface of the jet. These waves are initially homogenous in the spanwise direction. Hence, the disturbance is two-dimensional and independent of the spanwise coordinate.

The stability investigation is also limited to two-dimensional travelling wave disturbances, which means that the possibility for three dimensional disturbances are excluded, *e.g.* stationary roll cells or oblique waves.

The basic flow is a function of both x and y, but the variation in the streamwise direction is assumed to be slow compared to the streamwise wavelength of the disturbance. This means that the basic flow can be assumed to be locally parallel, *i.e.* only dependent on the y-coordinate.

4.1. Linear stability equations

The velocity field can be divided into the basic flow field and the disturbance flow field such that

$$\mathbf{u} = \{U(y) + u'(x,y,t), v'(x,y,t)\} \quad \text{and} \quad p = P + p'(x,y,t),$$

where the variables are scaled according to section 2.3, but with the lengthscale taken to be a_{local}, *i.e.* half the undisturbed local jet thickness, and primes denotes disturbance quantities. This decomposition can be inserted into the Navier-Stokes equations eqs. (16) and (17), and after linearization, *i.e.* neglecting terms that are quadratic in the disturbance quantities, this becomes

$$\frac{\partial u}{\partial t} + U\frac{\partial u}{\partial x} \quad + vDU \quad = -\frac{\partial p}{\partial x} + \frac{1}{Re^{l,g}_{local}}\left(\frac{\partial^2 u}{\partial x^2} + \frac{\partial^2 u}{\partial y^2}\right) \tag{25}$$

$$\frac{\partial v}{\partial t} + U\frac{\partial v}{\partial x} \qquad\qquad = -\frac{\partial p}{\partial y} + \frac{1}{Re^{l,g}_{local}}\left(\frac{\partial^2 v}{\partial x^2} + \frac{\partial^2 v}{\partial y^2}\right) \tag{26}$$

where the primes have been dropped[1] and $D = d/dy$. Similarly for the continuity equation

$$\frac{\partial u}{\partial x} + \frac{\partial v}{\partial y} = 0. \tag{27}$$

The Reynolds number $Re^{l,g}_{local}$ represents a local quantity that is obtained when scaling the dimensional equations with half the local jet thickness, a_{local}, the local mean velocity in the jet and the viscosity for the liquid and gas respectively. Since the flow rate is constant in the jet this means that the Reynolds number will be constant at all positions. The scaling of the length and velocity variables will however change. This implies that when the whole jet is considered the results obtained at one streamwise position has to be converted to the 'global' scaling, *i.e.* the half channel height and mean velocity in the channel.

The linearized momentum and continuity equations (25)–(27), can be used to obtain an equation for the v-disturbance

$$(\frac{\partial}{\partial t} + U\frac{\partial}{\partial x})\nabla^2 v - D^2 U\frac{\partial v}{\partial x} = \frac{1}{Re^{l,g}}\nabla^4 v. \tag{28}$$

This equation is linear in x and t, hence a normal mode ansatz can be made

$$v = \hat{v}(y)\exp\left[i\alpha(x - ct)\right]. \tag{29}$$

where $\hat{v}(y)$ is the amplitude function, α the streamwise wavenumber and c the phase speed. By substituting eq. (29) into eq. (28) this becomes the well known Orr-Sommerfeld equation,

$$i\alpha(U - c)(\hat{v}'' - \alpha^2\hat{v}) - i\alpha D^2 U\hat{v} = \frac{1}{Re^{l,g}}(\hat{v}^{iv} - 2\alpha^2\hat{v}'' + \alpha^4\hat{v}). \tag{30}$$

The Orr-Sommerfeld equation (30) together with the correct boundary conditions forms an eigenvalue problem,

$$\mathcal{F}(\alpha, c, Re) = 0.$$

This eigenvalue problem is solved for the complex eigenvalue $c = c_r + ic_i$, by choosing a fixed Reynolds number and a real wavenumber α. The real part c_r gives the phase velocity of the disturbance and the imaginary part c_i together with the wavenumber gives the growth rate in time, αc_i. If $c_i > 0$ the flow is linearly unstable, *i.e.* the disturbance is growing in time.

The disturbances on the free surfaces are given by,

$$\mathcal{H}_{+1}(x, y, t) = y - 1 - h_{+1}(x, t) = 0 \quad \text{at} \quad y = 1,$$
$$\mathcal{H}_{-1}(x, y, t) = y + 1 - h_{-1}(x, t) = 0 \quad \text{at} \quad y = -1.$$

[1]Throughout the rest of this chapter uppercase letters indicate quantities related to the basic laminar flow field, and lowercase letters indicate disturbance quantities.

If these expressions are inserted into the kinematic condition for the surfaces this gives

$$\frac{\partial h_{\pm 1}}{\partial t} + U^{l,g}\frac{\partial h_{\pm 1}}{\partial x} = v^{l,g} \quad \text{at} \quad y = \pm 1. \tag{31}$$

With the normal mode ansatz

$$h_{\pm 1} = \hat{h}_{\pm 1} \exp\left[i\alpha(x - ct)\right],$$

the kinematic condition becomes

$$i\alpha(U^{l,g} - c)\hat{h}_{\pm 1} = \hat{v}^{l,g} \quad \text{at} \quad y = \pm 1. \tag{32}$$

Here $\hat{h}_{\pm 1}$ is the amplitude of the disturbances at the two surfaces. Because of the symmetry of the basic flow with respect to the centreline of the jet, even and odd solutions to the eigenvalue problem can be treated separately[2]. This means that the eigenvalue problem can be solved in half the jet. The boundary conditions at the centreline are determined by the choice of even or odd solutions. The result of the eigenvalue problem is several different eigenvalues. To each eigenvalue belongs an eigenfunction, *i.e.* $\hat{v}$. The eigenvalue and the eigenfunction are said to represent a 'mode'.

4.2. Boundary conditions at the surface

The boundary conditions at the surface, eq. (8), are also linearized with use of the fact that the basic flow field satisfies the boundary conditions. At $y = 1 + h$ the boundary conditions are written as,

$$\frac{\partial v^l}{\partial x} + \frac{\partial u^l}{\partial y} + \frac{dU^l}{dy} - \tilde{\mu}\left(\frac{\partial v^g}{\partial x} + \frac{\partial u^g}{\partial y} + \frac{dU^g}{dy}\right) = 0 \tag{33}$$

$$p^l - \frac{2}{Re^l}\frac{\partial v^l}{\partial y} - \tilde{\rho}p^g + \tilde{\mu}\frac{2}{Re^l}\frac{\partial v^g}{\partial y} + \frac{1}{We}\frac{\partial^2 h}{\partial x^2} = 0. \tag{34}$$

These are linearized to the location of the boundary of the basic flow, $y = 1$. The assumption that the flow is parallel gives the following condition for the shear of the basic flow at the jet surface,

$$\left.\frac{dU^l}{dy}\right|_{y=1} = \tilde{\mu}\left.\frac{dU^g}{dy}\right|_{y=1}.$$

Hence these two terms should cancel in eq. (33), but since the surface is perturbed a distance h from its laminar state this is not the case. This can be seen from a series expansion of the derivative at $y = 1$, which gives

$$\left.\frac{dU^{l,g}}{dy}\right|_{y=1+h} = \left.\frac{dU^{l,g}}{dy}\right|_{y=1} + h\left.\frac{d^2U^{l,g}}{dy^2}\right|_{y=1} + \mathcal{O}(h^2).$$

[2] A v-even solution is equivalent to anti-symmetric wave and *vice versa*, see figure 1.2.

For the basic flow

$$\left.\frac{d^2U^l}{dy^2}\right|_{y=1} \neq \left.\frac{d^2U^g}{dy^2}\right|_{y=1},$$

in general. The boundary condition, eq. (33), can then with the aid of the continuity equation (27), be written as

$$\frac{\partial^2 v^l}{\partial x^2} - \frac{\partial^2 v^l}{\partial y^2} - \tilde{\mu}\left(\frac{\partial^2 v^g}{\partial x^2} - \frac{\partial^2 v^g}{\partial y^2}\right) + \left(\frac{d^2U^l}{dy^2} - \tilde{\mu}\frac{d^2U^l}{dy^2}\right)\frac{dh}{dx} = 0 \tag{35}$$

The pressure in eq. (34) can be removed by using the streamwise momentum equation (25) and the continuity equation (27). This gives

$$\left(\frac{\partial}{\partial t} - U^l\frac{\partial}{\partial x}\right)\frac{\partial v^l}{\partial y} - \frac{1}{Re^l}\left(3\frac{\partial^2}{\partial x^2} + \frac{\partial^2}{\partial y^2}\right)\frac{\partial v^l}{\partial y} - \tilde{\rho}\left(\frac{\partial}{\partial t} - U^g\frac{\partial}{\partial x}\right)\frac{\partial v^g}{\partial y} + \frac{\tilde{\mu}}{Re^l}\left(3\frac{\partial^2}{\partial x^2} + \frac{\partial^2}{\partial y^2}\right)\frac{\partial v^g}{\partial y} + \frac{1}{We}\frac{\partial^4 h}{\partial x^4} = 0. \tag{36}$$

The normal velocity is continuous across the surface, and since it in the basic flow is zero, v has to be continuous at $y = 1$,

$$v^l = v^g. \tag{37}$$

However, the streamwise velocity should also be continuous across the surface, $y = 1$, but if the basic flow is varying with y, then the condition becomes

$$u^l + U^l + h\frac{dU^l}{dy} = u^g + U^g + h\frac{dU^g}{dy},$$

where a series expansion of the basic flow around $y = 1$ has been performed and terms quadratic in the disturbance quantities dropped. The basic flow is continuous, hence

$$u^l + h\frac{dU^l}{dy} = u^g + h\frac{dU^g}{dy}, \tag{38}$$

which by taking $\partial/\partial x$ and using the continuity equation (27) can be written as

$$-\frac{\partial v^l}{\partial y} + \frac{dh}{dx}\frac{dU^l}{dy} + \frac{\partial v^g}{\partial y} - \frac{dh}{dx}\frac{dU^g}{dy} = 0. \tag{39}$$

4.2.1. Flow of an ambient inviscid gas. If the ambient gas is inviscid a solution to the disturbance quantities can be found analytically. We study the upper half plane $y \geq 0$ and the flow of the gas can be described by a velocity potential ϕ, which satisfies

$$\nabla^2\phi = 0,$$

with the far field boundary condition

$$\lim_{y\to\infty} \phi = 0.$$

With the normal mode ansatz, eq. (29), the solution for $y \geq 1$ is

$$\phi = C \exp\{\alpha[1 - y + i(x - ct)]\}, \tag{40}$$

where the constant C has to be determined. There is no shear between the liquid and gas, hence the streamwise component of the velocity is discontinuous at the surface. The basic flow of the gas is considered to be zero everywhere, and the kinematic condition, eq. (31), becomes

$$v^g + U^{l,g}\frac{\partial h}{\partial x} = v^l \quad \Rightarrow \quad v^g = v^l - U^l\frac{\partial h}{\partial x}. \tag{41}$$

By combining eqs. (40) and (41), C is evaluated and the velocity potential in the gas becomes

$$\phi = -\frac{v^l - i\alpha\hat{h}U^l}{\alpha}\exp\{\alpha[1 - y + i(x - ct)]\}.$$

The pressure on the surface from the gas is then given by the unsteady Bernoulli equation,

$$p^g = -\frac{\partial \phi}{\partial t} = ic(v^l - i\alpha\hat{h}U^l)\exp\{\alpha[1 - y + i(x - ct)]\}.$$

This inviscid treatment of the flow in the gas is similar to what was used by Li & Tankin (1991).

4.3. Solution method

There exist several solution methods for the eigenvalue problem generated by the linear stability theory, such as shooting methods that are used to find one single eigenvalue at the time, and methods that solve for the complete eigenvalue spectrum.

Here the eigenvalue problem has been solved with a spectral method, where the solution is represented as an infinite sum of Chebyshev polynomials,

$$\hat{v} = \sum_{n=0}^{\infty} b_n T_n(y), \quad \text{for} - 1 \leq y \leq 1, \tag{42}$$

where T_n is the n-th Chebyshev polynomial and b_n coefficients to be determined. The series is truncated at some finite value N and inserted into the equation and boundary conditions. This gives a linear system of the form

$$\mathcal{L}\mathbf{b} = c\mathcal{M}\mathbf{b},$$

where $\mathbf{b} = \{b_0, b_1, b_2, \ldots, b_{N-1}, b_N\}$ is the coefficient vector to the Chebyshev expansion (42). The matrices $\mathcal{L}$ and $\mathcal{M}$ are given by

$$\mathcal{L} = i\alpha U(\mathbf{T}'' - \alpha^2\mathbf{T}) - i\alpha U''\mathbf{T} - \frac{1}{Re^{l,g}}(\mathbf{T}^{iv} - 2\alpha^2\mathbf{T}'' + \alpha^4\mathbf{T}) \tag{43}$$

$$\mathcal{M} = i\alpha(\mathbf{T}'' - \alpha^2\mathbf{T}), \tag{44}$$

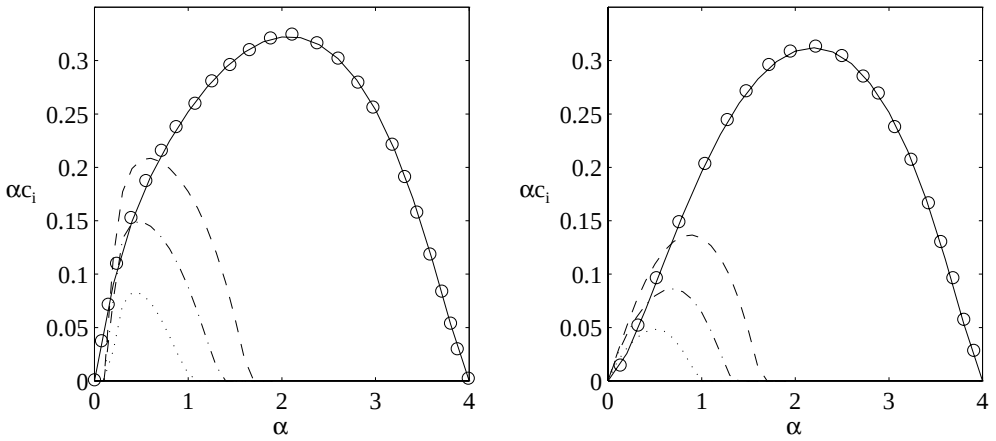

FIGURE 4.1. growth rate as a function of wavenumber. $We = 40$, $Re = 63.2$, $\tilde{\rho} = 0.1$, ($\circ$) Data from Li & Tankin (1991) and (–) calculation with inviscid ambient gas. Also, calculations with a viscous gas $\tilde{\mu} = 0.001$. (- -) $\delta_{99} = 0.023$, (- · -) 0.072 and ($\cdots$) 0.22. Even modes (left) and odd modes (right).

where $\mathbf{T^{(k)}}$ is a matrix representing the k:th derivative of the Chebyshev polynomials. The zeros of the highest order polynomial are chosen as collocation points. The grid points are given as

$$y_m = cos\frac{\pi m}{N}, \quad -1 \leq y \leq 1, \quad m = 0, 1, \ldots, N-1, N$$

which will give a distribution with grid points clustered at the ends of the interval. The matrices (43) and (44) have dimension $(N+1) \times (N+1)$. To these are added the boundary conditions (35)-(39) and the kinematic equation (32) for the free surface. This is done for the liquid as well as for the surrounding gas. The conditions at the free surface will couple these matrices. The resulting general eigenvalue problem can be solved with standard numerical methods. Here the eigenvalue problem was solved by the generalized eigenvalue solver, *eig*, built into the commercially available mathematical software *Matlab*.

4.4. Linear stability results for uniform jet flow

The stability of the plane liquid jet was analyzed for various initial velocity profiles and for various parameter regions. However, first results of calculations for a jet with a uniform velocity distribution are presented in order to compare with earlier reported results, Li & Tankin (1991). These results were obtained with the assumption that the surrounding gas is inviscid, and with a basic velocity distribution in the gas that is zero everywhere, *i.e.* there is a difference in the velocity for the gas and liquid at the surface.

In figure 4.1 the growth rate is plotted as a function of wavenumber. For this case only one unstable even mode and one unstable odd mode exist. The figure contains one graph showing the growth rate for the even mode and one graph showing the growth rate for the odd mode at $Re = 63.2$. For this Re the even mode is the most unstable for all wavenumbers. This Reynolds number was chosen to be able to compare the numerical results directly with the results by Li & Tankin. Hence, it is a way to validate the numerical solution method used here.

4.4.1. The effect of a viscous ambient gas. A viscous ambient gas will influence both the mean velocity distribution in the jet as well as the stability of the jet flow. If the viscosity ratio $\tilde{\mu}$, is small the influence on the mean velocity profile will be small, but the influence on the stability may still be large. This is due to the fact that in the inviscid case the source of instability is the pressure variation over the waves due to the velocity discontinuity at the surface. In the case of a viscous gas there will be a no-slip condition at the surface, which will change the boundary conditions for the disturbance and hence the stability.

In figure 4.1 results are also plotted for a jet with a viscous ambient gas, $\tilde{\mu}$ =0.001, and a basic flow of the gas given by eq. (14) in section 2.2. This small value of $\tilde{\mu}$ was chosen to exemplify the large effect of a viscous ambient gas. Since the basic flow of the jet is only slightly changed by the gas, it is assumed to be independent of the streamwise coordinate. To characterize the flow the thickness of the boundary layer in the surrounding gas is used. This is defined as δ_{99} and is taken at the position where the velocity of the gas is 1% of the mean velocity in the jet, U_m. Both the odd mode and the even mode are significantly damped for higher wavenumbers. From the figure it is also clear that for lower wavenumbers the viscosity in the gas may enhance the growth rate.

In the figure the growth rate is plotted for three different thicknesses of the boundary layer in the gas. This shows that the growth rate decreases when the thickness of the boundary layer is increased, which is equivalent with a reduced shear at the interface.

4.5. Linear stability results for viscous jet flow

The complete formulation of the stability problem for the plane liquid jet contains several parameters, Re, We, α, $\tilde{\mu}$ and $\tilde{\rho}$. It also depends on the downstream position as well as the inlet length for the basic flow. The effect of all parameters can not be investigated and the results presented are based on the flow of a water jet in air. This means that $\tilde{\mu}$ and $\tilde{\rho}$ will be kept constant. For $T = 20°\text{C}$ the viscosity for water is $\mu^l = 1.01 \cdot 10^{-3}$ kg/ms and for air $\mu^g = 1.79 \cdot 10^{-5}$ kg/ms, which gives a viscosity ratio $\tilde{\mu} = 0.0177$. Similarly for the density $\rho^l = 997$ kg/m^3 and $\rho^g = 1.21$ kg/m^3, which gives $\tilde{\rho} = 1.21 \cdot 10^{-3}$. The surface tension was set to be $\gamma = 0.070$ N/m.

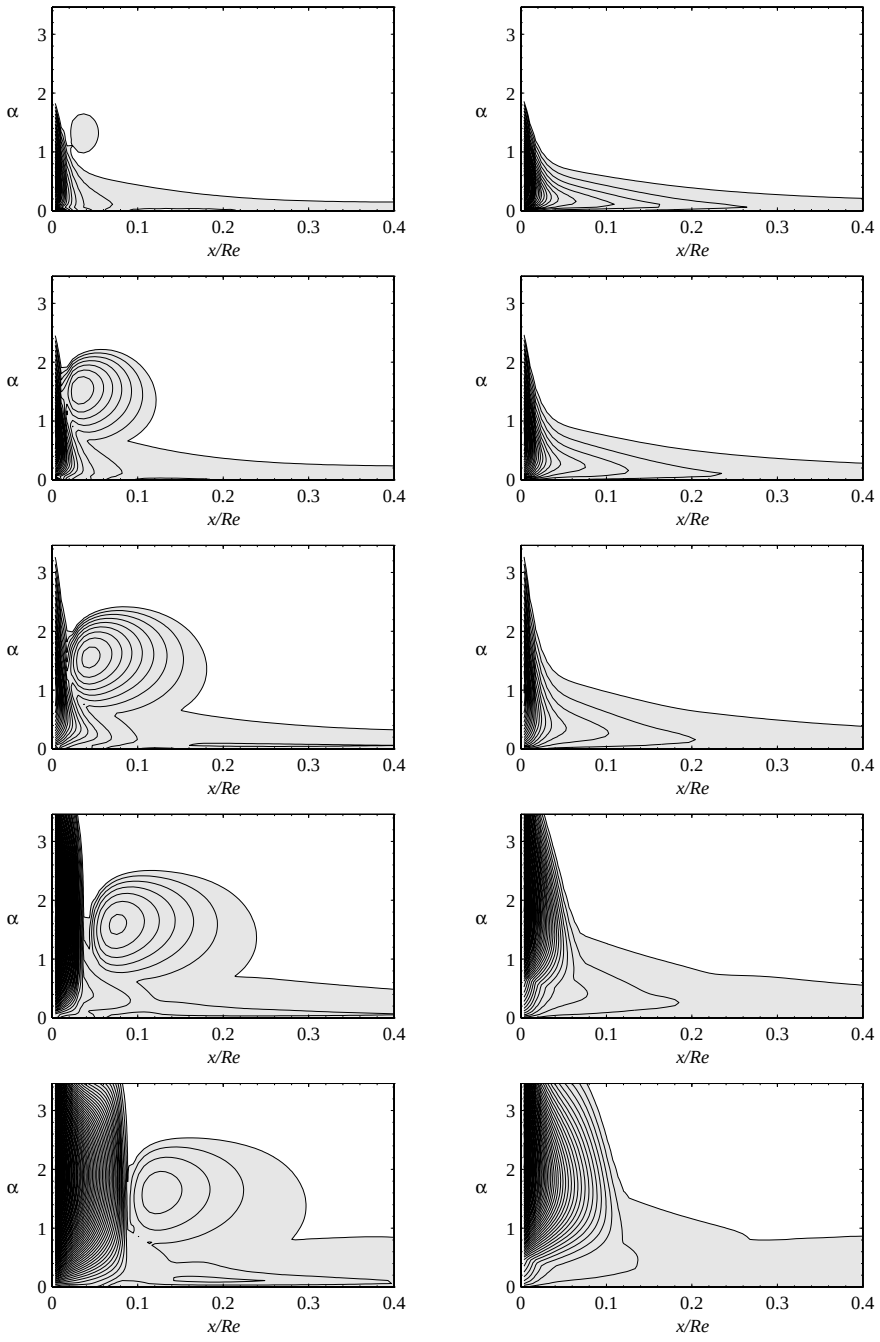

FIGURE 4.2. Unstable regions for a plane liquid jet emanating form a channel surrounded by a viscous gas. The shaded area indicates an unstable region. Also, the growth rate is indicated by contours of constant growth rate, $\Delta\alpha c_i = 0.005$. The left column contains the results for the even modes and the right column the result for the odd modes. From top to bottom Re = 125, 250, 500, 1000, 2000.

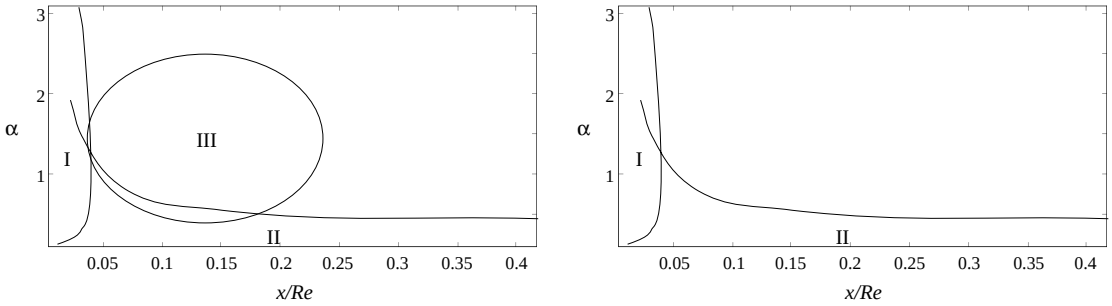

FIGURE 4.3. Qualitative description of the location of the unstable modes in figure 4.2. Even modes (left) and odd modes (right)

4.5.1. Stability diagrams. Figure 4.2 shows unstable regions for a plane liquid jet emanating from a channel with an upstream parabolic velocity profile. In the figure results for five different Reynolds numbers are shown, $Re = 125$, 250, 500, 1000 and 2000. The vertical axis in the graphs represents the 'global' wavenumber and the horizontal axis the streamwise position scaled with the Reynolds number. As the velocity distribution scales with x/Re, it is also convenient to present the stability diagrams as function of this variable.

The jet is unstable in the shaded region of the figures with a growth rate indicated by contour curves. The figure shows both even modes (left column), and odd modes (right column). When the Reynolds number is increased the shaded regions grows. It should be noted that an increase in Reynolds number gives that for a constant x/Re the x-position moves downstream.

Three different unstable anti-symmetric (even) modes can be found in figure 4.2. The unstable regions for these modes partially overlap and are difficult to separate. However, one of these three even modes appears as a bounded region with a centre at $\alpha \approx 1.5$. This mode becomes unstable a distance downstream the nozzle and becomes stable again further downstream. In figure 4.3 the locations of the different modes are given qualitatively. The bounded mode corresponds to region *III*.

This region can be clearly seen for the lowest Reynolds number, $Re = 125$. As the Reynolds number is increased both the upstream end and maximum of this region moves towards higher x/Re. It is also expanding in the wavenumber direction. The maximum growth rate for this region increases to $Re = 1000$, after which it decreases.

There is no similar region for the odd modes. However, if this bounded region of instability for the even modes is excluded, the graphs for the two remaining even modes are similar to the graphs for the odd modes. The qualitative location for these modes are given by regions *I* and *II* in figure 4.3.

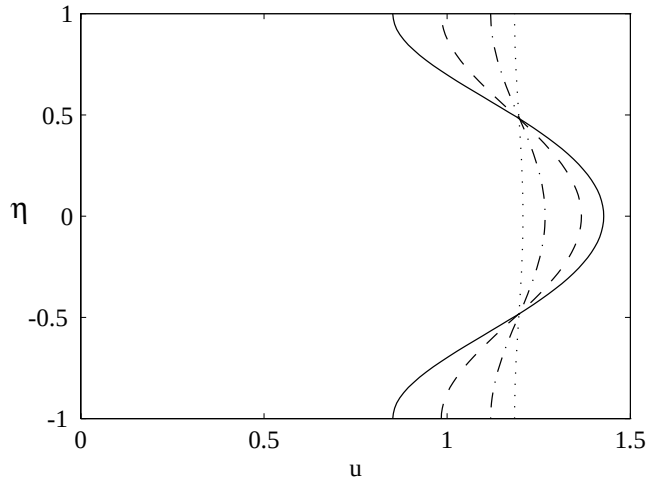

FIGURE 4.4. Streamwise velocity profiles for the four positions in figure 4.5. (—) $x/Re = 0.037$, (- -) 0.069, (- · -) 0.149, (· · ·) 0.306.

For $Re = 125$ the regions given by I and II are concentrated to the lower left corner, *i.e.* close to the nozzle and to low wavenumbers. This region has two branches, one which is orientated parallel to the vertical axis and one which is parallel to the horizontal axis. When the Reynolds number is increased the branch closest to the α axis extends towards higher wavenumbers and further downstream. The slope from high growth rate to no growth at all is very steep, since the contour curves are stacked together in this region. For $Re = 2000$ the region seems to be parallel to the α-axis, for $\alpha > 0.5$. This is not the case since for higher wavenumbers than those shown in the graph, the growth rate decreases. The maximum growth in this region is found at $\alpha \approx 1.5$. The second branch, *i.e.* the region orientated along the x/Re-axis, also expands for higher Reynolds numbers and becomes parallel to the axis for $x/Re = 0.2$. However, it seems to extend somewhere from the middle of the α-axis in the graph. The unstable region for the odd modes has a similar behaviour but the area of the region is larger and the maximum growth rate is lower.

To investigate the effect of the velocity profile on the stability, the profiles at four positions, $x/Re = 0.037$, 0.069, 0.149, 0.306 were examined with respect to wavenumber and Reynolds number. The velocity profiles can be seen in figure 4.4 and the corresponding stability diagrams in figure 4.5. The vertical axis of the graphs in figure 4.5 represents the 'local' wavenumber, *i.e.* scaling is performed with the local jet thickness, and the horizontal axis represents the Reynolds number, *Re*. As for figure 4.2 even and odd modes are shown, and the unstable regions are shaded. The qualitative location of the modes can be found in figure 4.6. As for the figure 4.5 the streamwise position of the velocity profiles will change when the Reynolds number changes.

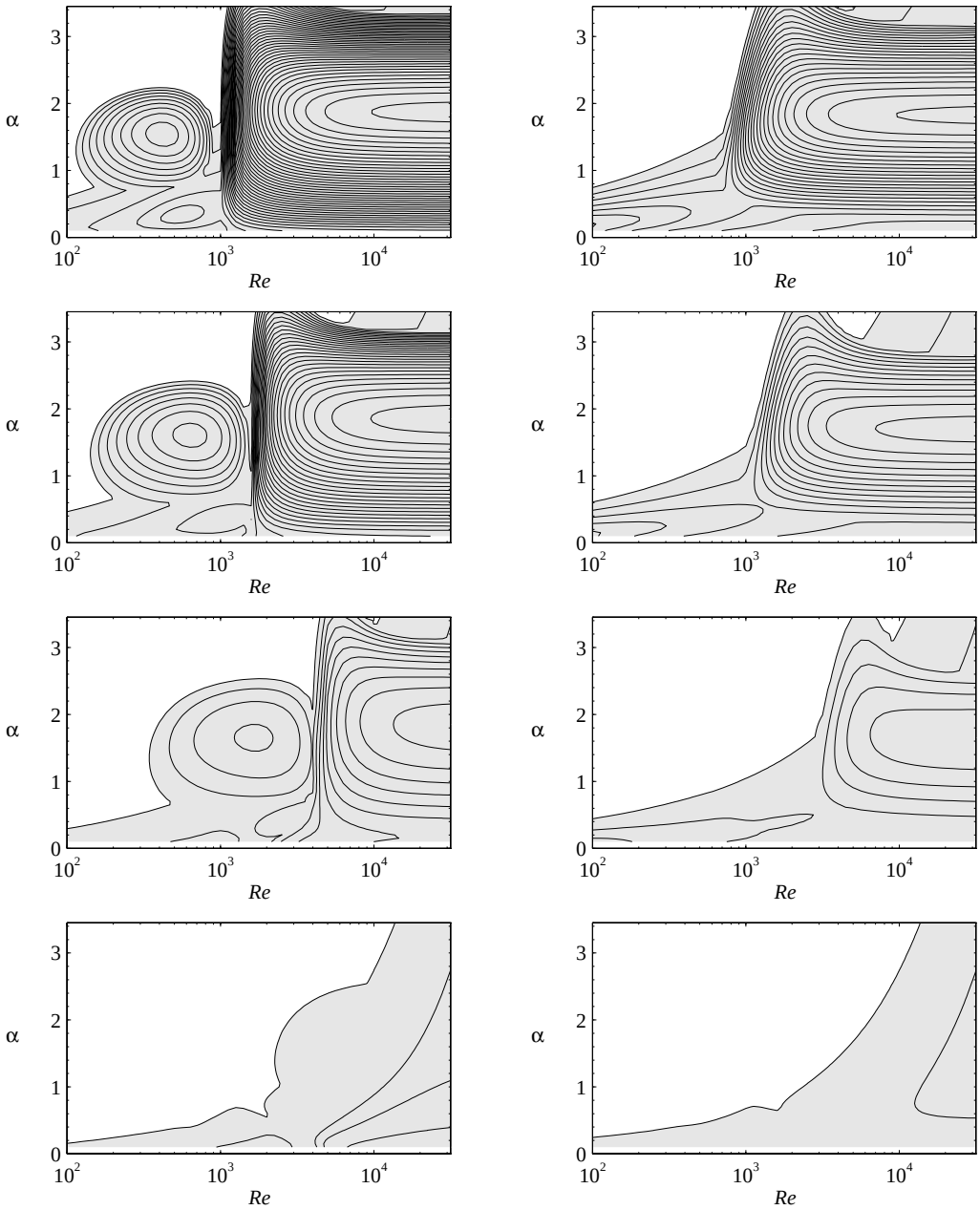

FIGURE 4.5. The maximum growth rate as a function of Reynolds number for four positions in the jet with a fully developed Poiseuille flow inside the channel. Distance between two contourlines $\Delta\alpha c_i = 0.005$. The left column contains the v-even modes and the right odd modes. From top to bottom $x/Re = 0.037, 0.069, 0.149, 0.306$.

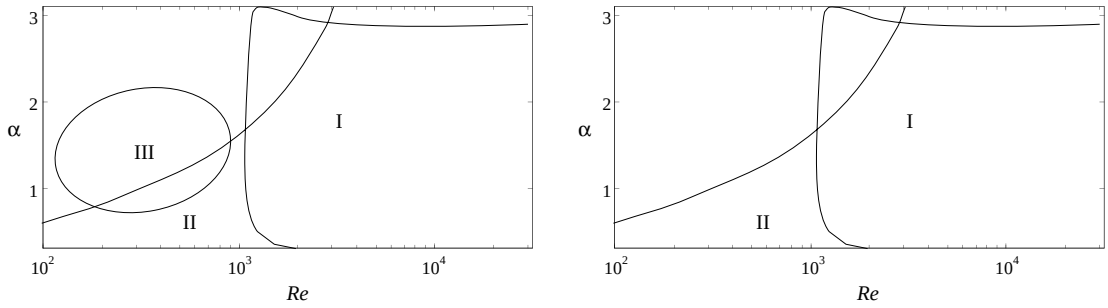

FIGURE 4.6. Qualitative description of the location of the unstable modes in figures 4.5. Even modes (left) and odd modes (right)

The first position chosen was at $x/Re = 0.037$. This is a position where the location of the free surface is still changing. Consider first the even modes. For the lowest Reynolds number shown, $Re = 100$, there is an unstable region *II* for $\alpha < 0.6$. When the Reynolds number is increased the growth rate increases and region *II* extends towards higher wavenumbers. For a Reynolds number only slightly higher a second unstable region *III* can be seen. This is the same region as the bounded region found in figure 4.2, and the maximum is found at $\alpha \approx 1.5$ and $Re \approx 400$. Behind this the low wavenumber region *II* can be seen extending to higher wavenumbers with increasing Reynolds number. For $Re \approx 1000$ the third unstable region *I* can be identified. The growth rate for this region increases quickly with Reynolds number, and the maximum growth is found at $\alpha \approx 1.9$. This region seems to occur at $Re \approx 1000$ for all waveneumbers in the wavenumber region shown. For the odd modes a similar behaviour can be found for regions *I* and *II*.

For the velocity profile at $x/Re = 0.069$ the growth rate for all regions has decreased. All regions have also moved towards higher Reynolds numbers. To the next position at $x/Re = 0.149$ the decrease is continued. Especially the growth rate in region *I* has decreased for both the even and the odd mode.

The lowest graphs represent $x/Re = 0.306$,where region *I* has vanished totally while region *III* still can be seen, but now starting at $Re \approx 2500$. For all four position the extent of region *II* only changes slightly.

In figure 4.7 the flow of the ambient gas is the same as for figure 4.5. However, the velocity distribution in the jet is uniform and assumed to be unaffected by the gas. As can be seen in the figure only one type of mode is unstable. By comparison between figures 4.5 and 4.7 it is clear that this mode is almost independent of the velocity distribution.

4.5.2. Amplitude distribution of the disturbance. The separation of the modes in the unstable regions has been done by examining the eigenvalue spectra and the eigenfunctions. These can be seen in figures 4.8-4.10. These figures all

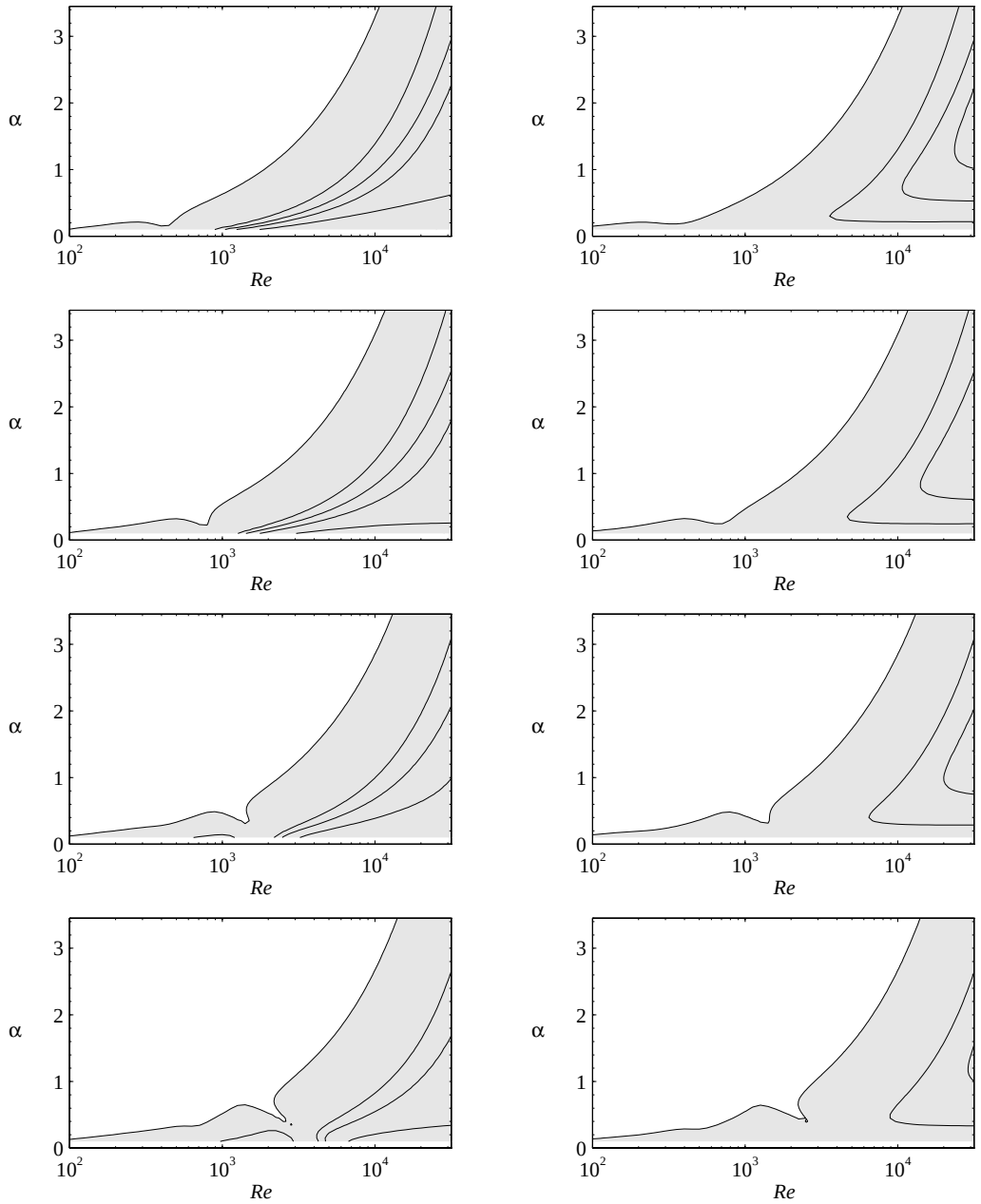

FIGURE 4.7. The maximum growth rate as a function of Reynolds number for four positions in a uniform jet with viscous ambient gas. Distance between two contourlines $\Delta\alpha c_i$ =0.005. The left column contains the v-even modes and the right odd modes. From top to bottom $x/Re = 0.037$, 0.069, 0.149, 0.306.

contain six graphs with the upper left graph in each figure representing the eigenvalue spectrum. The horizontal axis represents the real part of the eigenvalues, which is the same as the phase velocity, c_r. It should be remembered that the velocity is normalized with the mean velocity of the jet. The vertical axis represents the growth rate, αc_i. An eigenvalue above $\alpha c_i = 0$, corresponds to a growing disturbance.

Five more graphs are shown in each figure, and these represents the eigenfunctions for five different eigenvalues. Those graphs are marked, $e_{I,II,III}$ and $o_{I,II}$, corresponding to the eigenvalue with the same marking in the eigenvalue spectrum. The eigenvalues are related to figures 4.2, 4.5 and 4.7 through the subscripts *I*, *II* and *III*, whereas *e* indicates an even mode and *o* an odd mode. The vertical axis in these graphs represents the y-axis, with the location of the centreline at $y = 0$ and the free surface at $y = 1$. In the graphs the u-disturbance amplitude is given as a solid line and the amplitude for the v-disturbance as a dash-dotted line. At the top of each of those five graphs the corresponding eigenvalue is presented with phase speed c_r and growth rate αc_i.

Figure 4.8 shows a typical eigenvalue spectrum for region *I*, $Re = 5000$ and $\alpha = 1.5$. As can be seen mode e_I gives maximum growth, and for this the maximum amplitude in the eigenfunction for the streamwise velocity is found at the location for the inflection point in the basic velocity profile. The phase speed of this disturbance is very close to the mean velocity for the jet at this location. There is a similar odd mode o_I, with a slightly lower growth rate and higher phase velocity. The modes representing region *II* have the maximum streamwise velocity at the surface.

Mode e_{III} has as an eigenfunction that is similar to modes e_I and o_I. In order to see that this is really the mode corresponding to region *III* the eigenvalue spectra was plotted for a fixed wavenumber $\alpha = 1.5$, for Reynolds numbers starting from $Re = 500$ and increasing. The stepsize was kept sufficiently small, to allow tracking of the individual modes.

Figure 4.9 is representative for region *II*. The Reynolds number and wavenumber have changed compared to figure 4.8, $Re = 1000$ and $\alpha = 0.3$. The maximum growth rate is found for mode o_{II}. The eigenfunction corresponding to this mode gives the maximum disturbance velocity at the surface, both for the normal as well as for the streamwise velocity. For the even mode the maximum is found at the centreline. The mode corresponding to region *III* has the u-maximum at the inflection point and the v-maximum and the centreline. Also, the v-velocity is close to zero at the surface for e_{III}.

Figure 4.10 shows the eigenvalue spectrum from the centre of region *III*. The even mode e_{III}, which has no counterpart if the odd modes is the most unstable. The eigenfunction for this mode gives two maxima for the u-velocity, one which is close to the surface and one which is slightly below the inflection point. The normal velocity is zero at the surface which implies that the amplitude of the

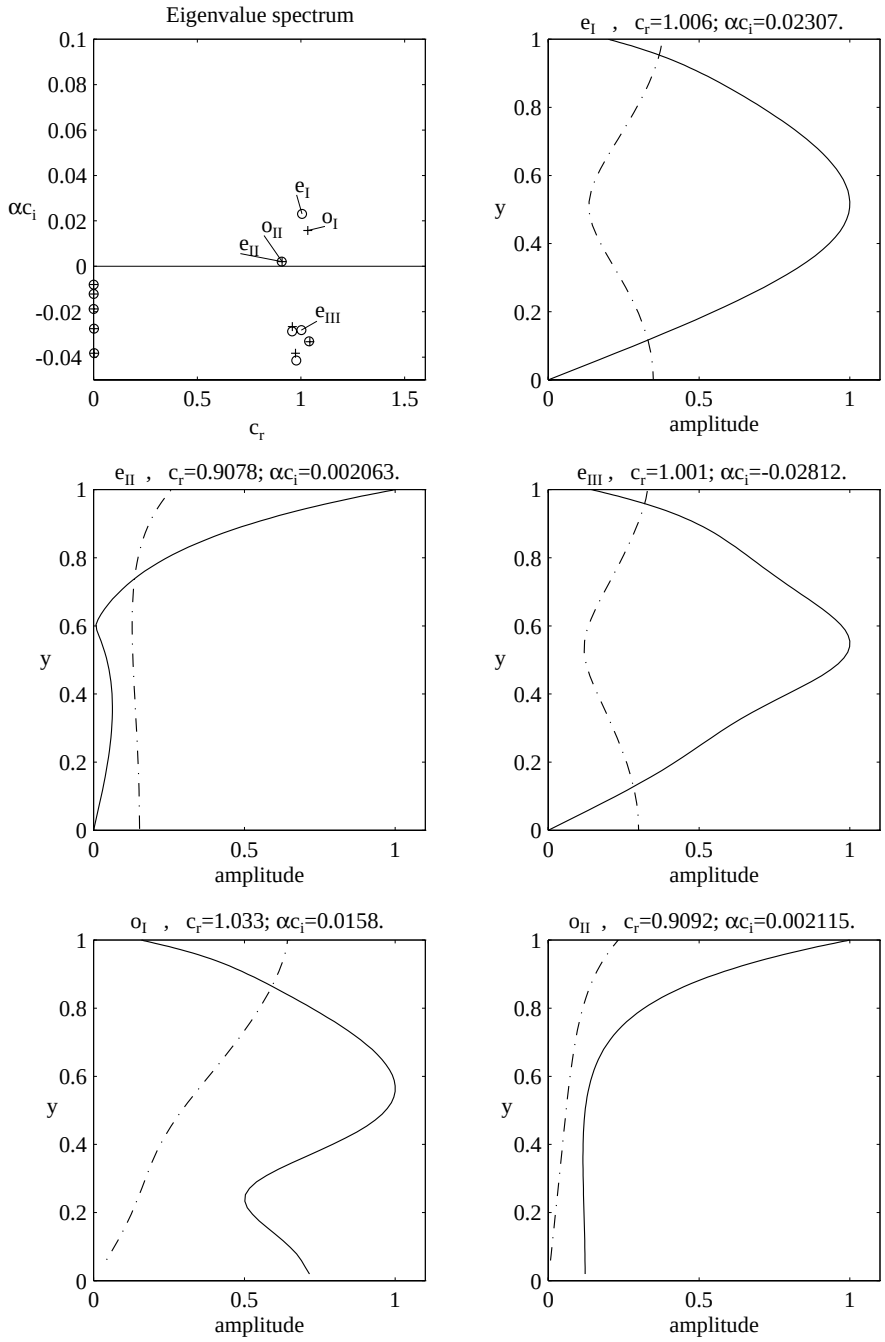

FIGURE 4.8. Eigenvalue spectrum and eigenfunctions for $x/Re = 0.149$. $Re = 5000$ and $\alpha = 1.5$ (region I). ($\circ$) v-even and ($+$) v-odd modes. (—) u-amplitude and (- · -) v-amplitude. Calculated with a non-uniform velocity profile and viscous ambient gas.

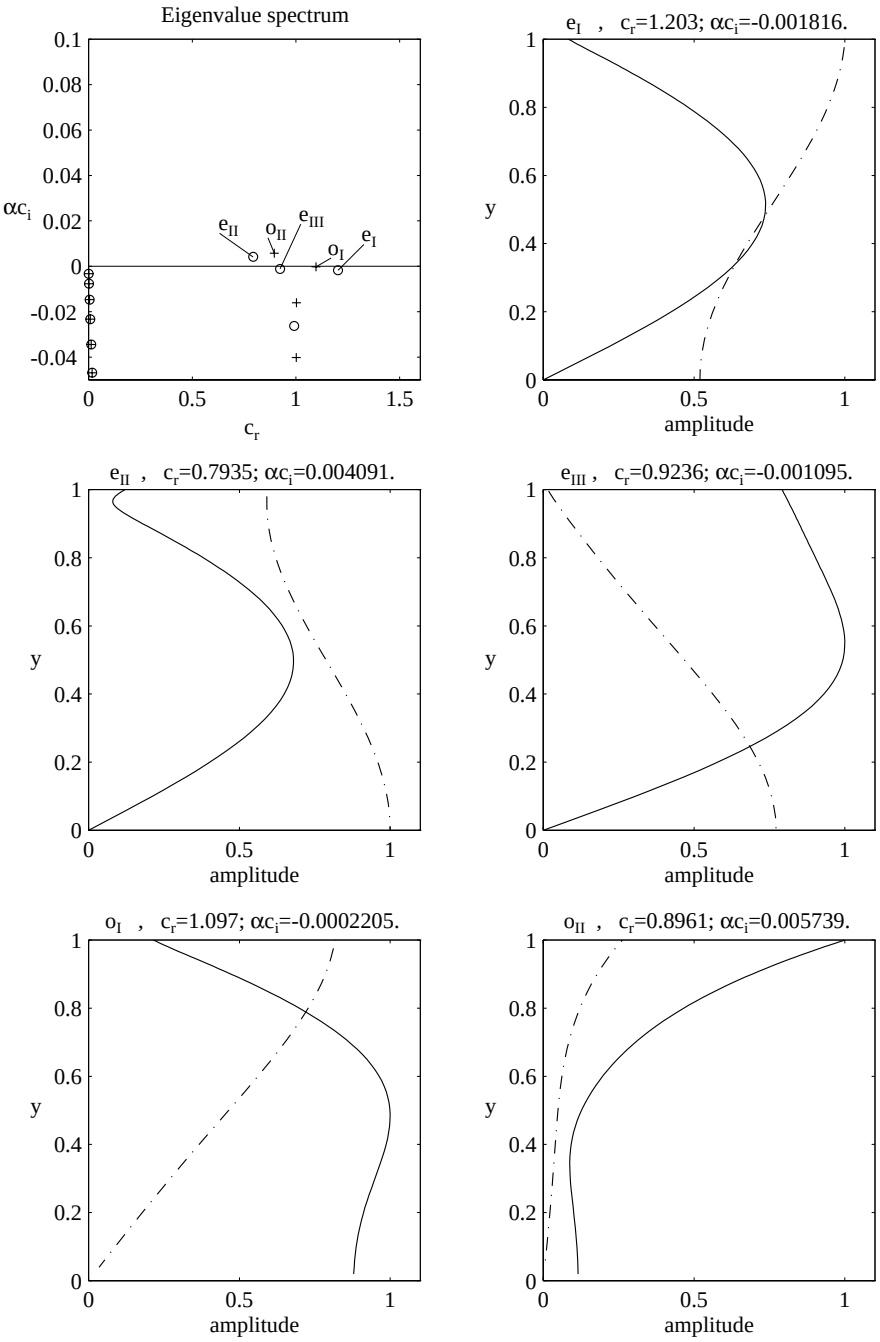

FIGURE 4.9. Eigenvalue spectrum and eigenfunctions for $x/Re = 0.149$. $Re = 1000$ and $\alpha = 0.3$ (region II). ($\circ$) v-even and ($+$) v-odd modes. (—) u-amplitude and (- · -) v-amplitude. Calculated with a non-uniform velocity profile and viscous ambient gas.

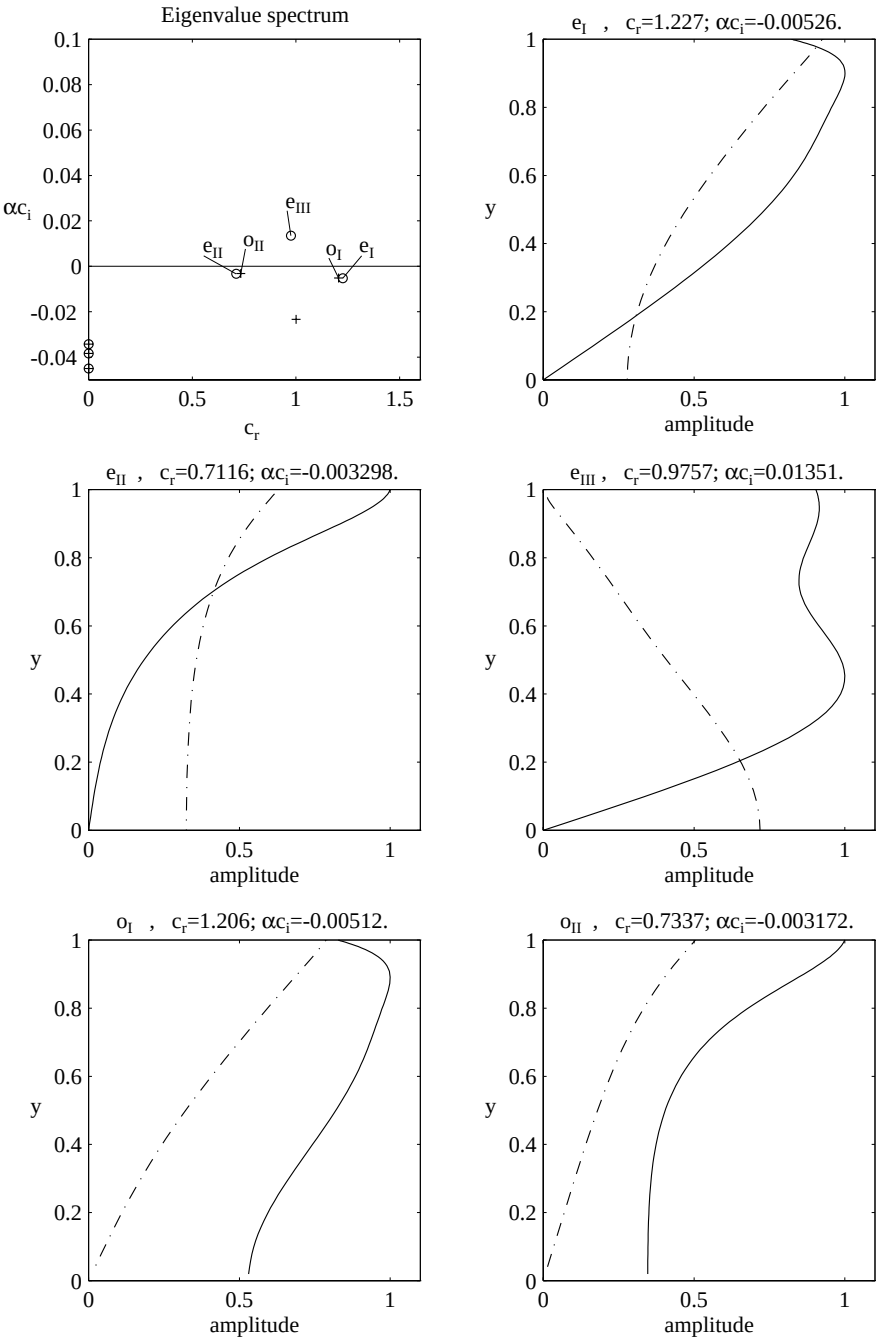

FIGURE 4.10. Eigenvalue spectrum and eigenfunctions for $x/Re = 0.149$. $Re = 1000$ and $\alpha = 1.5$ (region *III*). ($\circ$) v-even and ($+$) v-odd modes. (—) u-amplitude and (- · -) v-amplitude. Calculated with a non-uniform velocity profile and viscous ambient gas.

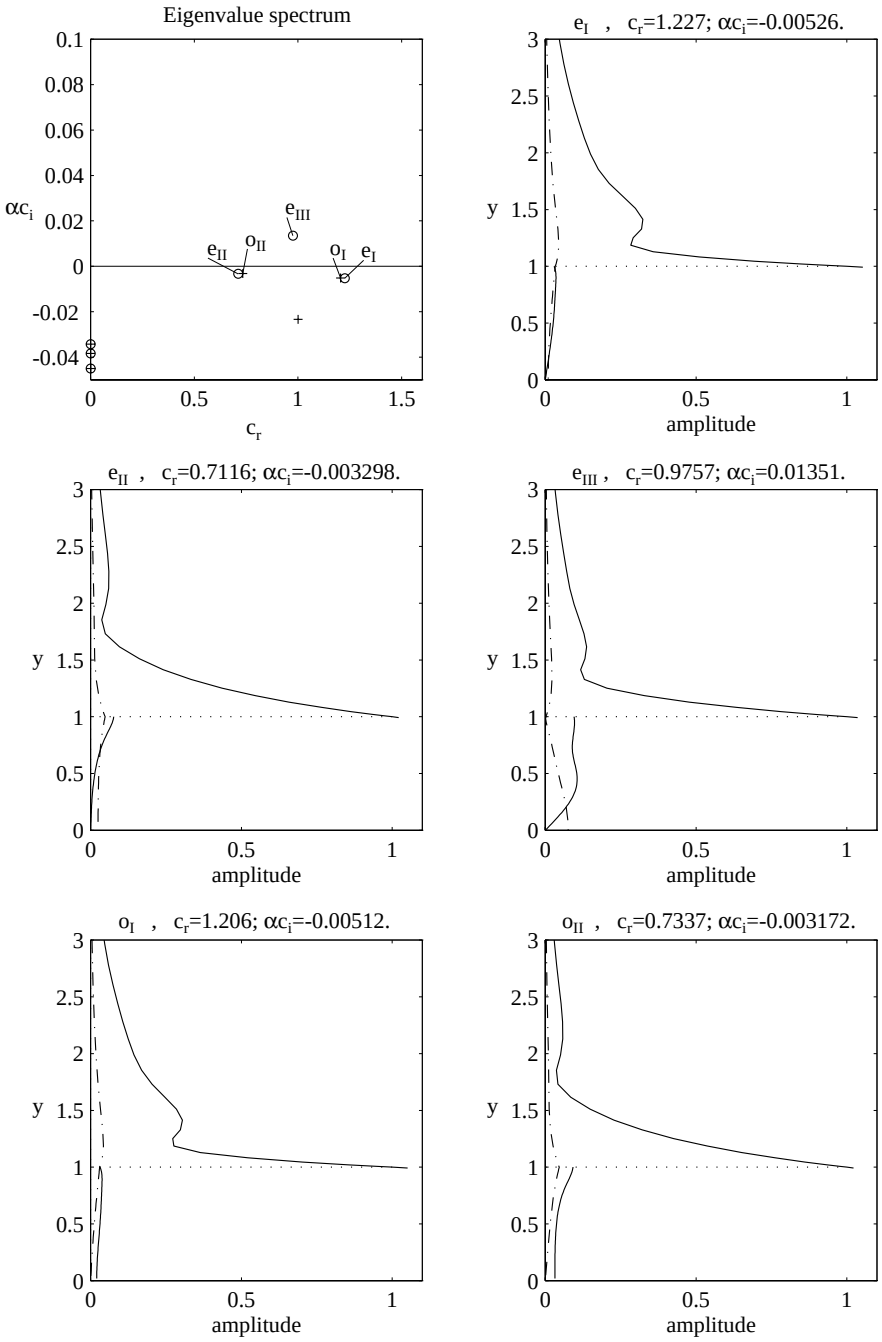

FIGURE 4.11. Eigenvalue spectra and eigenfunctions for $x/Re = 0.149$. $Re = 1000$ and $\alpha = 1.5$ (region *III*). ($\circ$) v-even and ($+$) v-odd modes. (—) u-amplitude and (- · -) v-amplitude. Calculated with a non-uniform velocity profile and viscous ambient gas.

waves on the surface is zero. The other four modes all have maxima close to or at the surface for both velocity components.

The calculation includes the ambient gas, and figure 4.11 shows the same parameters as figure 4.9 with the amplitude of the disturbance velocities in the air added in the graphs. The v disturbance velocity is continuous across the surface. This is given by the boundary condition, eq. (37). The amplitude of the streamwise velocity disturbance is larger in the gas at the surface of the jet than in the liquid. This discontinuity is given by eq. (38).

Since the flow is unbounded there exists a continuous branch in the eigenvalue spectra, see *e.g* Drazin & Reid (1981). For figures 4.8–4.11 this continuous branch can be found close to the real axis, *i.e.* $c_r = 0$.

4.5.3. Effect of varying entrance length. The importance of the basic velocity distribution can be examined by replacing the upstream fully developed flow with a partially developed flow. Four different inlet lengths have been chosen, which give different velocity profiles at the end of the channel. The result can be seen in figure 4.12. The modes that are unstable directly after the end of the channel, region *I*, have a growth rate that decreases with decreasing inlet length. This is also true for the bounded mode, region *III*. However, the low wavenumber modes, region *II* seems to be almost unaffected by the change in velocity profile.

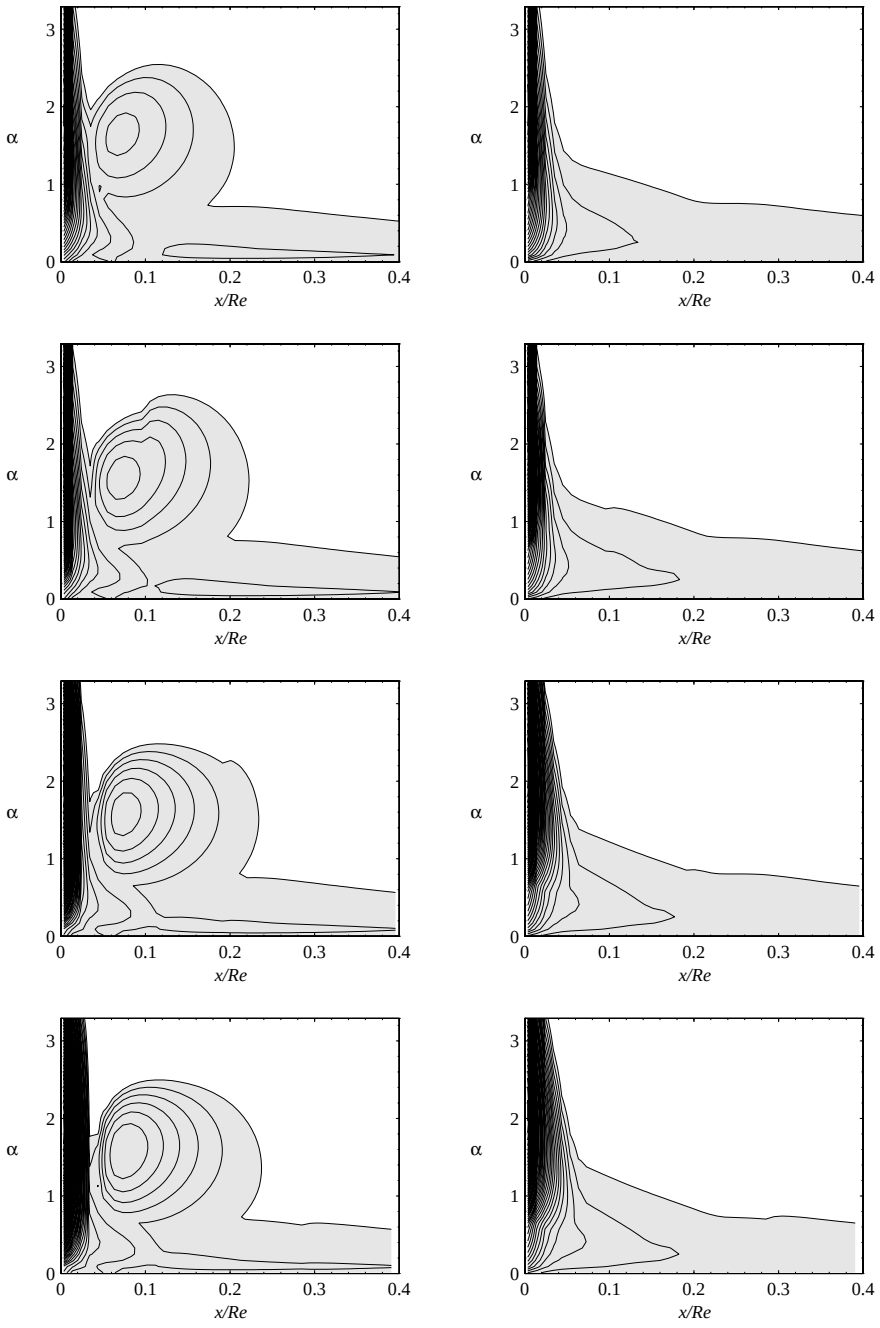

FIGURE 4.12. Unstable regions for a plane liquid jet emanating from a channel with varying entrance length, from top to bottom $\ell_E = 15$, 30, 70, 110, and $Re = 1000$. The shaded area indicates an unstable region. Also, the growth rate is indicated by contours of constant growth rate. $\Delta\alpha c_i$ =0.005. The left column contains the plane for v-even modes and the left odd modes. Calculated with viscous ambient gas.

CHAPTER 5

Experimental set-up

5.1. The flow loop and the nozzle

Two different types of plane water-jets have been produced with the apparatus shown in figure 5.1. The apparatus consists of three main parts, the headbox where the nozzle is mounted, the dump tank and the submerged centrifugal pump. The flow rate was adjusted with a valve downstream the pump. The maximum flow rate of the pump is 340 l/min and the maximum pressure head 125 kPa. The jet width at the outlet is 150 mm and with a 2 mm jet it is possible to obtain a jet velocity of 11 m/s but for thicker jets the velocity is reduced. The maximum obtainable Reynolds number based on jet thickness is around $25 \cdot 10^3$.

The water is fed from the pump to the headbox through a hardened PVC hose which is connected to a stiff PVC tube just upstream the headbox. The PVC-tube was divided into two before entering the headbox. To minimise vibrations the headbox was tightly fixed to a heavy workshop machinery tripod standing directly on the basement floor. In order to damp pressure pulsations in the system a small air pocket was kept at the top of the supply loop.

The headbox had the dimensions 25x25x15 cm^3 and was made of Plexiglas allowing optical access to its interior. At the outlet of the headbox different nozzle geometries can be inserted. The two nozzles used in this study were a two-dimensional *vena contracta* type and a plane channel nozzle which will produce a more or less fully developed plane Poiseuille flow. The width of the nozzles was 15 cm. Due to surface tension acting on the free rims of a plane jet, the jet tend to contract in the spanwise direction (see *e.g.* Taylor (1959)). To avoid this and in order to ensure the two dimensionality of the jet, the sides of the jet were prevented to contract by letting side walls extend 20 cm beyond the nozzle exit. The orientation of the jet was chosen such that the jet emanates vertically to simplify shadowgraph visualizations and to avoid a bending of the jet by gravity.

The jet flow quality depends on the upstream conditions in the headbox, such as flow inhomogeneities and turbulence level and scales. In order to reduce such disturbances the water, when entering the headbox, had to pass a flow distributor consisting of a 30 mm thick bed of packed 4 mm diameter glass beads. Downstream this distributor the flow passed two fine meshed screens which reduce the turbulence level and also give a pressure drop which helps making the flow uniform. Downstream the screens a 6 cm long honeycomb with a cell diameter of 5 mm aligns the flow. Finally a screen was mounted as an arc with the top directed

in the flow direction. This made it possible for air bubbles to move up to the sides at start up of the flow loop. Air bubbles did however easily get stuck at this screen and therefore it was possible to manually vibrate the screen by inserting a bar from the nozzle opening. The last screen had a porosity of 0.60 and for all velocities the Reynolds number based on wire diameter was less than 10 and hence this final screen was subcritical. The arc-shape of the screen will redirect the flow slightly and this will have some effect on the velocity distribution in the jets but the effect is assumed to be negligible. A pressure transducer was mounted on the wall of the headbox downstream the last screen and the transducer output was calibrated against the jet flow rate.

The slit nozzle consisted of two 5 mm thick brass pieces which were machined sharp at the outlet side. They could easily be moved in order to change the slit width.

The channel nozzle consisted of a contraction made of two quarter cylinders with a radius of 5 cm followed by two 4 cm long flat plates, all made of brass. Also for this nozzle the channel width could be varied.

Both nozzles were carefully polished before performing any experiments. The sharp edges were checked regularly to ensure that they had no damages which could disturb the jet. Damage to the edges (or even a water droplet stuck at the outlet) showed up in the visualizations as a stationary wave pattern on the surface having a V-shape with the origin at the edge.

The flow of the gas surrounding the jet will influence the flow of the jet. With the present design of the nozzles and headbox the air flow should be similar for the two different orifices tested.

5.2. Flow visualization

Two different methods have been used to visualize the flow of the plane jet, namely the shadowgraph method and reflective flakes (iriodin) seeded in the water. For both methods the images have been processed to obtain not only qualitative but also quantitative information.

5.2.1. Shadowgraph method. For the shadowgraph method, figure 5.2 *i*, the jet was illuminated from one side by an ordinary slide projector standing 5 m from the jet. The distance should be as large as possible since the light source ideally should approximate a point light source. When the light from the projector pass through the jet any curvature of the surface of the jet, will give rise to a deflection of the light. This will be seen as a pattern of shadows on a semi-transparent plate which is mounted on the other side of the jet. This pattern corresponds to the irregularities on the surface of the liquid jet. The sharpness of the pattern depends on the distance between the jet and plate, and a shorter distance gives a sharper picture. The semi-transparent plate had vertical and horizontal centimeter markings in order to simplify measurements in the shadowgraph image.

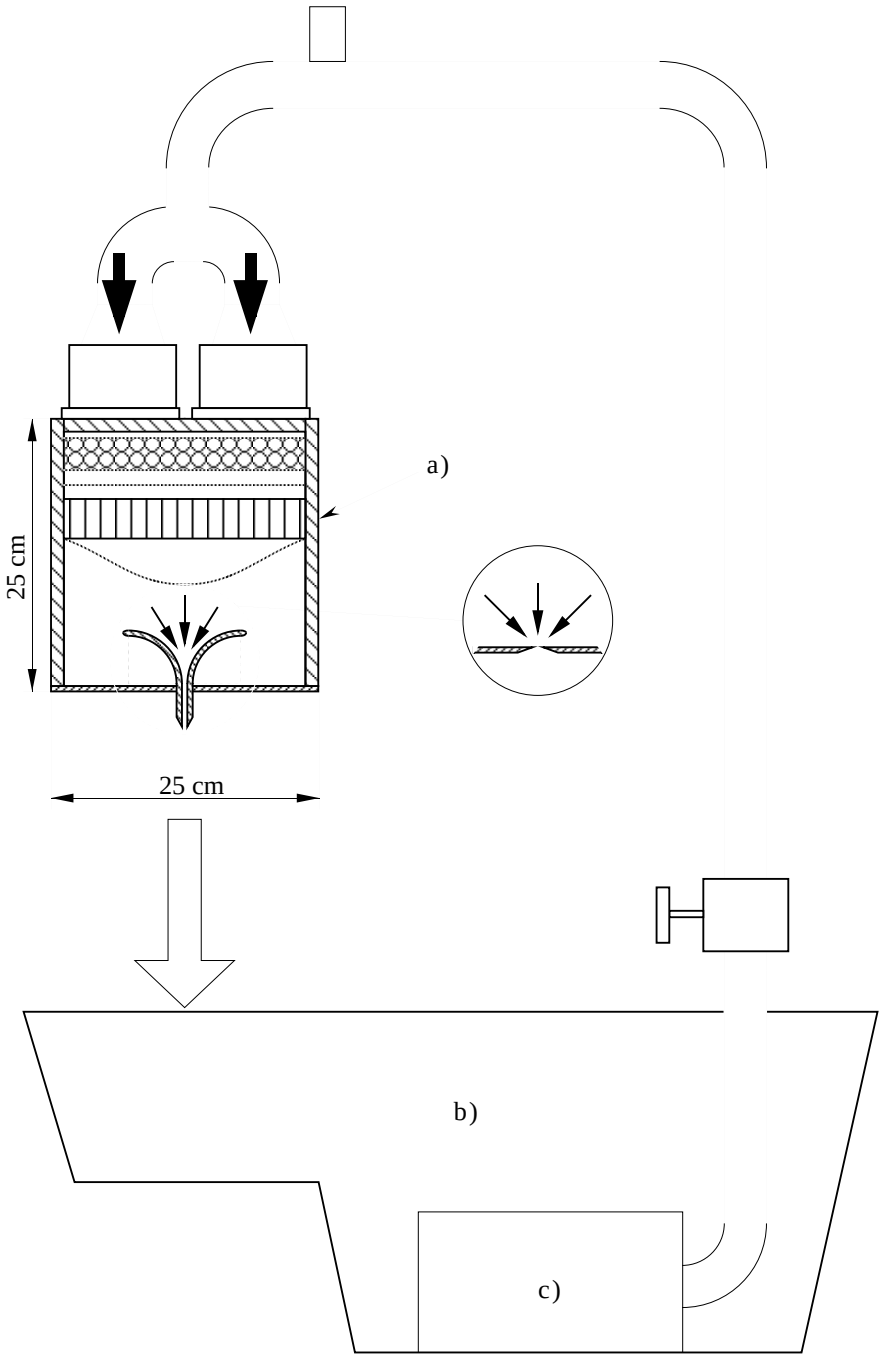

FIGURE 5.1. Experimental setup, a) head box, b) dump tank, c) centrifugal pump.

5.2.2. Reflective flakes. Reflective flakes were used to visualize phenomena inside the jet. These flakes react on the shear, and tend to orient along stream surfaces. In order to detect a gradient in the flow, only a small concentration

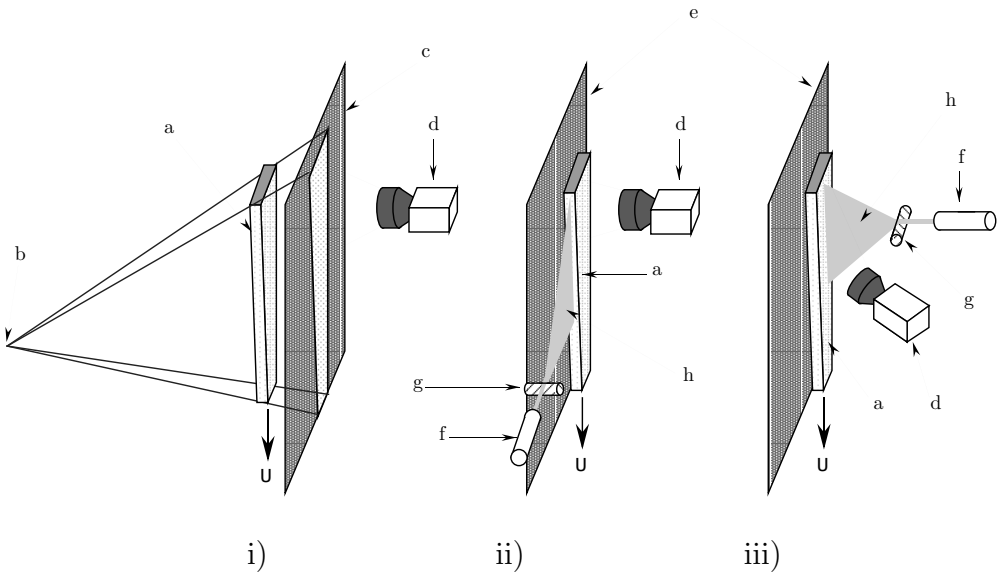

FIGURE 5.2. Visualization set-ups. i) shadowgraph; ii) particle visualization with a light sheet from the side; iii) particle visualization with a light sheet normal to the jet. a) liquid jet, b) light source, c) semi-transparent plate, d) camera, e) black background, f) laser, g) glass cylinder and h) laser sheet.

of the flakes is needed. The jet was then illuminated with a laser sheet in two different configurations, shown in figure 5.2 *ii* and *iii*.

The laser sheet was created by letting the laser beam from a 10 mW semiconductor laser pass through a glass cylinder. In the first configuration the light sheet was led into the jet from the side, figure 5.2 *ii*. The light sheet had a thickness of approximately 1 mm, which allowed an illumination of the core of the jet. In the second configuration the sheet was directed normal to the jet, 5.2 *iii*, which allowed for illumination of the thickness variation of the jet. For both configurations a black non-reflecting curtain was used as a background to improve the contrast.

5.2.3. Video recording and photography. Both the shadowgraph and particle visualizations were recorded. Photos of the visualizations were taken by an Olympus OM-2 camera with 35 mm black and white as well as colour slide film. Also, video recordings were made with a greyscale CCD-camera and a Hi8 video recorder. The use of video allows transient events to be captured as long as the speed of these is not too high. To improve the time resolution further a high-speed CCD-camera (Kappa 100) was used. This allowed sequences to be captured at 500 frames per second.

5.2.4. Image processing. To determine the wave length of the wave disturbance accurately image processing of the video recordings was made. Frames from the video recording of the shadowgraph visualization were transferred to a

Macintosh PowerPC/8500 computer via a *Scion LG-3* frame grabber card. From each frame a small strip (typically 10 pixels wide) representing the centre of the jet was extracted and transferred to the numerical software *Matlab*. To remove noise the images were averaged in the spanwise direction. The result was a signal with a clear waveform. This signal was then divided into overlapping sequences and the streamwise length of these was typically a few wavelengths. However the background light intensity varied almost linearly in the streamwise direction and therefore the following expression for the intensity variation, $I(x)$, was fitted to the data in the least square sense,

$$I(x) = A\sin(kx + \varphi) + Bx + I_m.$$

Here A is the amplitude of the wave, k the wavenumber, φ the phase, B the coefficient for the linear trend of the intensity and I_m the mean intensity in the image. Since this was made on a series of sequences for different streamwise positions, the downstream development with x of the wavenumber could be found. In order to improve the accuracy this was done for 50-100 consecutive frames, and the results were averaged. From the wavenumber the wave length and the phase speed of the waves (knowing their angular frequency) could easily be obtained.

5.3. Velocity measurements

Velocity measurements in the jet were made both to determine the mean flow development and to investigate the disturbance flow. The mean flow measurements were made with a Pitot tube, whereas the time dependent velocity measurements were made with hot wire anemometry.

5.3.1. Pitot tube measurements. Jet velocity profiles were measured with a Pitot tube constructed from a small stainless steel tube. The original tube had inner and outer diameters of 0.4 mm and 0.6 mm, respectively. To reduce the spatial dimension of the Pitot tube tip the tube was flattened and sharpened at its end, resulting in an inner opening of 0.08 mm and an outer width of 0.2 mm. Special care was taken to ensure that the edges of the hole were sharp and this was checked with a microscope. The probe could be manually traversed through the jet. The pressure measured with the Pitot tube was transmitted by PVC-tubes to a differential pressure transducer. The pressure transducer measured the difference between the total pressure from the Pitot tube and the atmospheric pressure, which was assumed to be the same as the static pressure in the jet.

It was necessary to ensure that there was no air present in the tubing from the Pitot tube to the pressure transducer, which otherwise could have an effect on the pressure reading. The lack of air in the pressure sensing system was possible to determine not only by the transparency of the tubes, but also by monitoring the adjustment time when subjected to a change in pressure. When fully functioning the response time was less than 0.5 s, but if an air bubble entered the system

this time increased dramatically. The Pitot tube and pressure transducer were calibrated against a known height of water before and after the measurements.

5.3.2. Hot wire anemometry measurements. Hot wire anemometry was used to determine the amplitude and phase distributions of the travelling wave disturbance. The anemometer used was a Dantec M01 and the hot film probe was the boundary layer type R15. It has a cylindrical sensor with a diameter of 70 μm and a sensing length of 1.25 mm. The hot film probe could be traversed through the jet with the same traversing mechanism as used for the Pitot tube measurements.

To obtain absolute measurements from hot wire anemometry the anemometer system has to be calibrated. However, since the procedure to obtain absolute readings is quite cumbersome since hot film anemometry in water is subjected to various sources of drift, it was decided to only obtain relative readings of the wave amplitude. If the amplitude of the fluctuating signal is small the relation between the signal from the anemometer and the velocity can be assumed to be linear. This can easily be seen from the King's law expression given by

$$u = k_1(E - E_0)^{1/n},$$

where E is the output from the anemometer at u velocity, E_0 the output at zero velocity, and k_1 and n constants determined by calibration. A series expansion around the mean velocity U_m or the voltage at this velocity E_m, gives

$$U_m + \Delta U = k_1\left((E_m + \Delta E)^2 - E_0^2\right)^{1/n} = k_1\left(E_m^2 - E_0^2\right)^{1/n} + \left[\frac{2k_1}{n}\frac{E_m}{E_m + E_0}\left(E_m^2 - E_0^2\right)^{1/n}\right]\epsilon + \mathcal{O}(\epsilon^2),$$

where

$$\epsilon = \frac{\Delta E}{E_m - E_0}.$$

Hence if $\Delta E \ll E_m - E_0$, then

$$\Delta U \sim \Delta E.$$

The experimental set-up to determine the wave characteristics can be seen in figure 5.3. The hot film probe was traversed through the jet at a distance of 20 mm downstream of the nozzle. The waves were triggered by a loudspeaker mounted on the nozzle and a signal generator was used to drive the loudspeaker at a fixed frequency. The signal to the speaker was sampled to a Macintosh Classic computer simultaneously as the signal from the anemometer by a *GW Instruments, inc.* MacAdios-adio A/D-converter. By traversing the probe through the jet and sample at a number of locations the phase of the disturbance could be found by using the generator signal as reference.

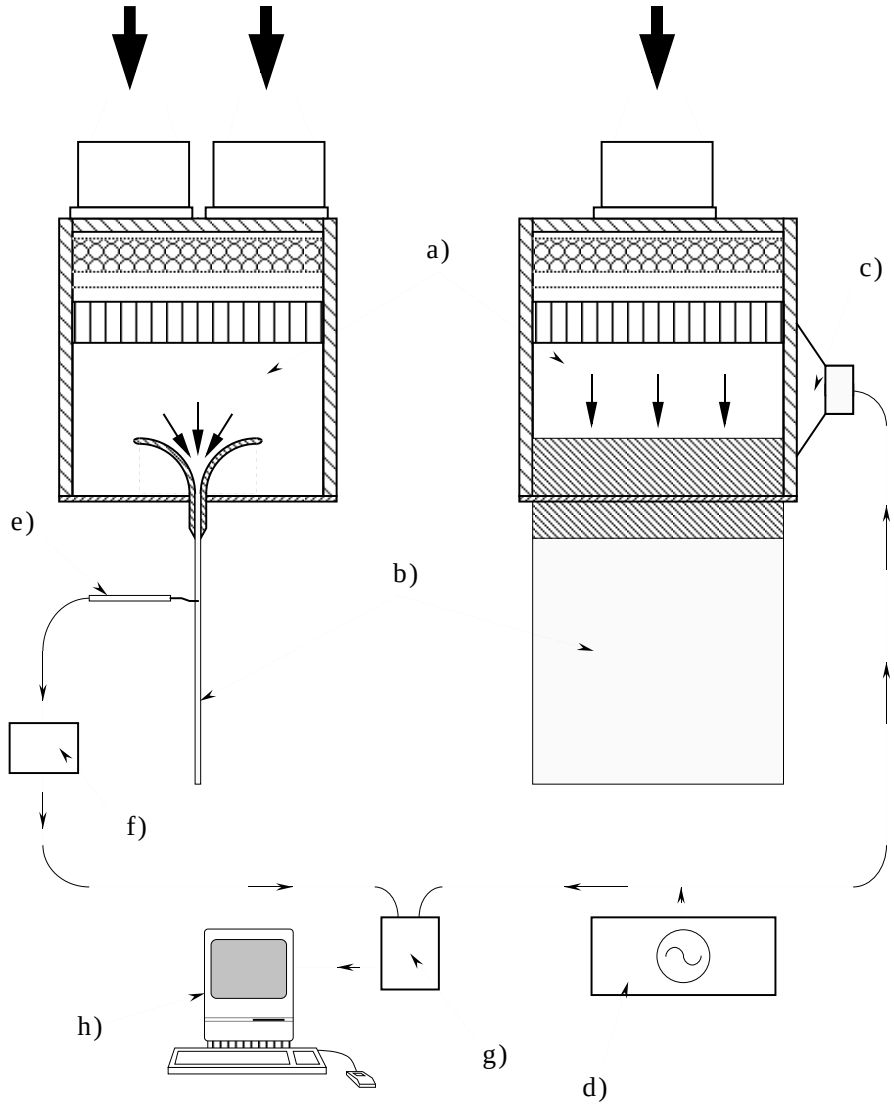

FIGURE 5.3. Measurements with hot wire anemometry. a) headbox, b) liquid jet, c) loudspeaker, d) signal generator, e) hot wire probe, f) anemometer, g) A/D converter and h) computer.

CHAPTER 6

Experimental results

Measurements of the streamwise velocity distribution and flow visualizations were made with both the channel and the slit nozzle. The results showed significant differences in the behaviour of jets emanating from these nozzles. Special emphasis was put on the development of the wave instability which was studied both with flow visualization and hot wire anemometry.

6.1. Mean flow development in the channel jet

Velocity profiles were measured with a Pitot tube at the end of the channel and at four downstream positions, $x = 0$, 10, 20, 30, 40 mm, see figure 6.1. In this figure results from two measurement series are shown. These were taken in the central region of the jet, where the Pitot tube was totally submerged. When this was not the case capillary waves could be seen upstream the point where the surface was disturbed. The occurrence of these waves was determined through visual inspection of the surface of the jet close to the tip of the Pitot tube. Also, if the Pitot tube was not fully inside the jet the measured pressure was slowly

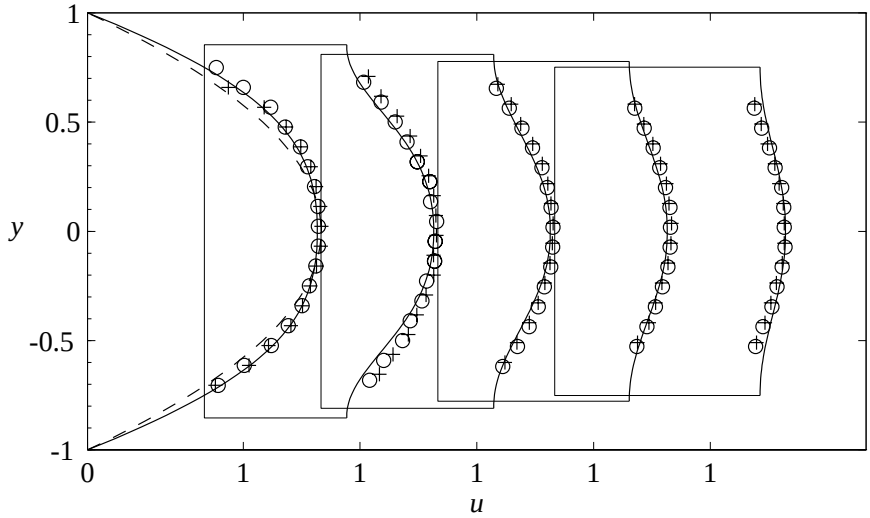

FIGURE 6.1. Velocity distribution in the channel jet. (—) calculated, (+) and (∘) measured, (– –) parabolic profile with the same maximum velocity as the measured profile. $U_m = 1.3$ m/s, $a = 0.55$ mm, $Re = 700$, profiles at $x = 0$, 10, 20, 30, 40 mm.

fluctuating. This was a result of an unsteady flow past the tip of the tube, *i.e.* the water covered the tube intermittently.

The result from a numerical solution, obtained with the method described in chapter 3 of the entrance flow in a plane channel, was fitted to the measured velocity profile at $x = 0$. This gave an entrance length of $\ell_E \approx 80a$, which corresponds well to the length of the plane part of the channel nozzle which is $73a$. The fitted profile at the end of the channel was then used as the upstream boundary condition in a calculation with the same parameters as in the experiment. Since the experimental jet was directed vertically, gravity was included in this calculation.

The result of this calculation can also be seen in figure 6.1. As a reference a parabolic profile with the same maximum velocity is also shown. This shows that the flow in the channel was not a fully developed parabolic flow. At the four downstream positions the jet is contracting according to the calculation, as the profile relaxation accelerates the liquid at the surface. The velocity at the centreline of the jet does not decrease, but increases slightly a distance downstream due to gravity.

The region in the jet where measured points satisfy the condition that the Pitot tube should be totally submerged is shrinking downstream implying that the jet is contracting. The contraction can also be seen in figure 6.2, which is a time averaged image of a particle visualization with the set-up shown in figure 5.2 *iii.* This image is taken from below at an angle to the jet. The nozzle can be seen in the top of the image where the brightest regions are reflections from the nozzle. The image was averaged over 100 frames to reduce noise and enhance contrast. The gradual contraction of the jet can be seen clearly.

6.2. Channel jet instabilities

6.2.1. Natural waves on the surface of the jet. The outflow from the plane channel nozzle was visualized with the shadowgraph method, and a series of eight images at different velocities can be seen in figure 6.3. The velocities range from 1.3–4.4 m/s and the corresponding Re from 700–2400. The dark regions at the sides of the jet are the side walls which prevent the spanwise contraction of the jet. Along the sides and at the bottom of the images centimeter markings can be seen. For all images the channel width is 1.1 mm.

At a low velocity, $U_m = 1.3$ m/s, the only disturbance on the jet surface is capillary waves originating from the vertical side walls and free rims at the sides of the jet, figure 6.3 *a.* The origins of these capillary waves are primarily the upstream ends of the side walls, which form small upward facing steps to the flow. However, the flow in the centre of the jet is assumed to be unaffected by these disturbances.

When the velocity is increased, $U_m = 1.5$ m/s, periodic darker and brighter lines parallel to the nozzle start to appear in the shadowgraph image, figure 6.3 *b.*

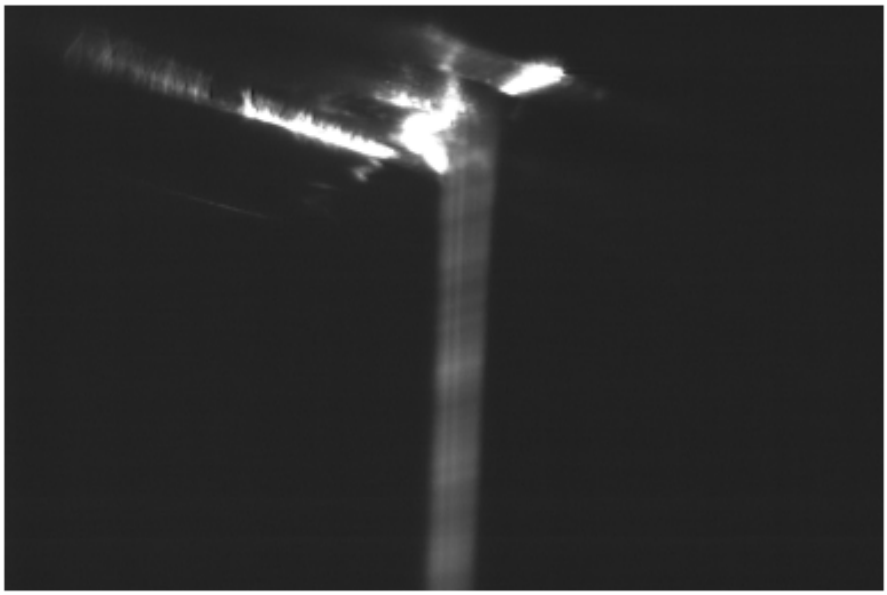

FIGURE 6.2. Particle visualization of the contraction of the jet. The nozzle can be seen at the top of the image.

These are a result of waves on the surface of the jet. The wavelength is of the order of 3 mm.

In figure 6.3 *c*, the velocity of the jet is increased further, $U_m = 1.7$ m/s. In the region $x = 7$–8 cm of this image localized irregularities can be seen in the jet, which indicate the development of three dimensional disturbances. These seem to originate from the break-up of the waves and occur randomly.

As the velocity increases the break-up moves closer to the nozzle, figures 6.3 *d*–*f*. The velocities are $U_m = 1.8, 1.9$ and 2.0 m/s, respectively. Also, the location of the break-up becomes more localized to a line parallel with the nozzle when the velocity is increased. Downstream of the break-up streaky structures in the streamwise direction can be seen in the visualization, figures 6.3 *e,f*. The break-up of the waves cause spray formation on the surface, *i.e.* drop formation, and at higher velocities this spray formation increases. In figures 6.3 *g,h* it makes the visualizations to become blurry, since the large amount of small drops will deflect the light randomly. In the last image the break-up is so strong that holes start to appear in the jet, which can be seen as bright spots in figure 6.3 *h*.

6.2.2. Waves forced by acoustic excitation. With a loudspeaker attached to the headbox it was possible to trigger waves in the jet before naturally occurring waves were observed. When this is done with a fixed frequency, the phase of the waves is also fixed, relative to the phase of the loudspeaker signal.

The waves could also be triggered by noise, for instance by clapping your hands a few meters away from the jet.

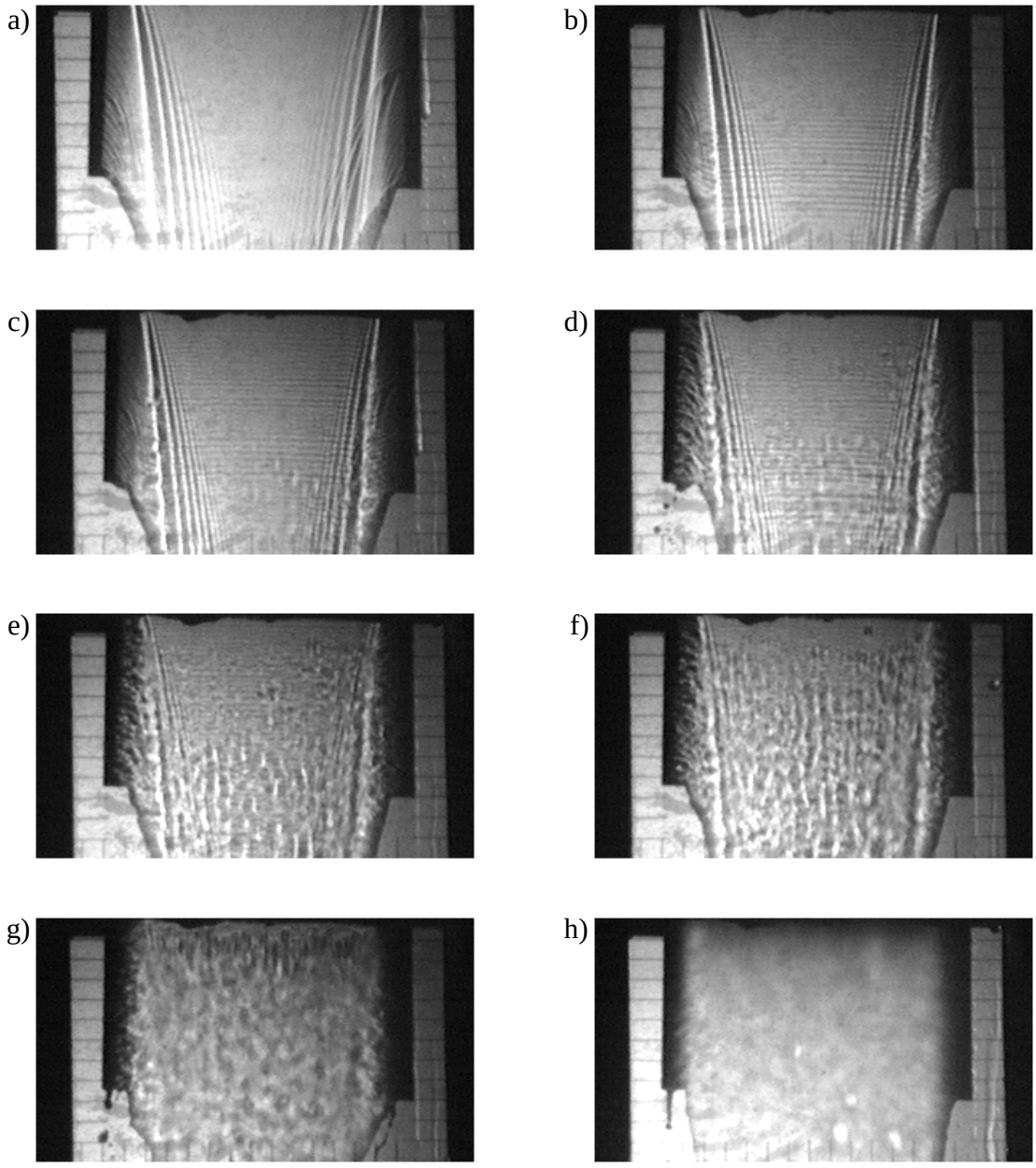

FIGURE 6.3. Wave development and break-up for naturally occurring disturbances visualized with the shadowgraph technique. a = 0.55 mm, a) 1.3 m/s, b) 1.5 m/s, c) 1.7 m/s, d) 1.8 m/s, e) 1.9 m/s, f) 2.0 m/s, g) 2.2 m/s, h) 4.4 m/s.

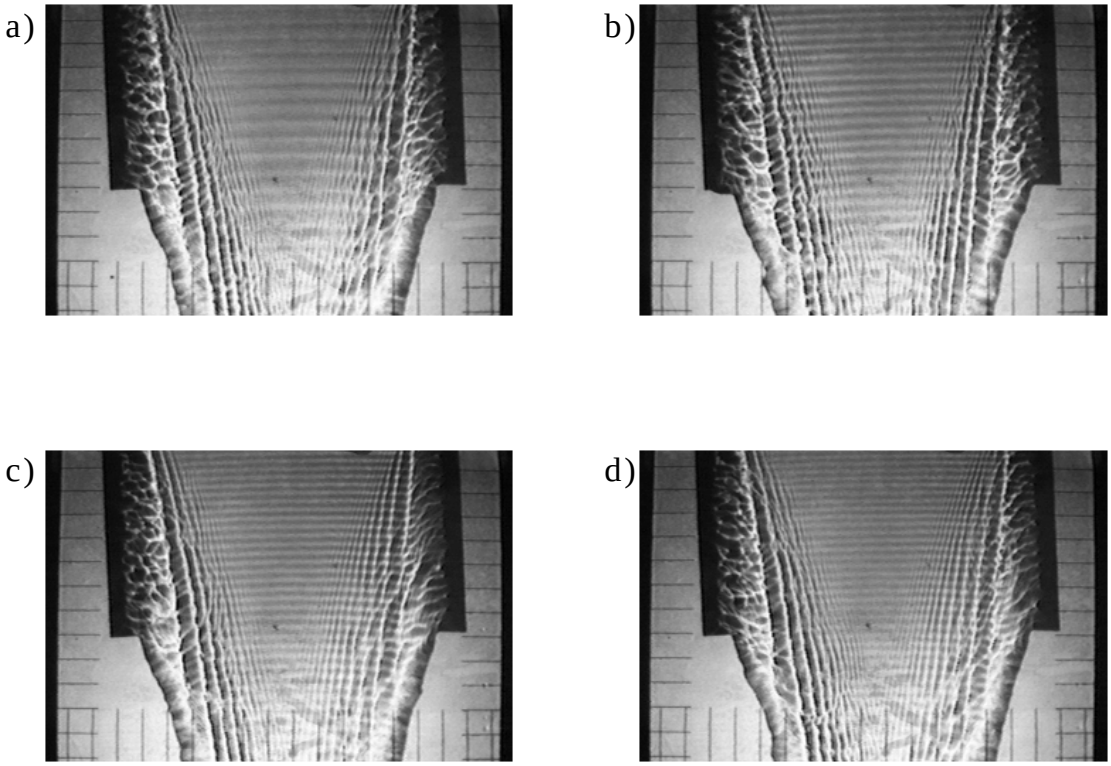

FIGURE 6.4. Shadowgraph visualization of forced wave disturbances $Re = 700$ and $a = 0.55$ mm. a) $f = 340$ Hz, b) 485 Hz, c) 612 Hz, d) 669 Hz.

Figure 6.4 shows a series of four images of the jet at $Re = 700$ at four different forcing frequencies. In the figure the Reynolds number is just below the limit of naturally occurring waves. The images show the response to different frequencies starting at the lowest frequency for which it was possible to obtain waves with the audio equipment used, and ending with the highest frequency. By iteratively lowering the amplitude of the forcing signal and changing the frequency it was possible to determine the frequency for which the waves were most unstable. This frequency was found to be $f \approx 530$ Hz.

By image processing it is possible to get quantitative measurements from these images. Figure 6.5 shows the downstream development of the wavenumber and amplitude of the waves, where the amplitude is taken from the intensity variation and evaluated according to appendix B. The left graph shows the variation of the wavenumber α as a function of the distance from the nozzle x, where $x = 0$ corresponds to the nozzle edge. In the graph results for four frequencies are shown and these frequencies are the same as for figure 6.4. As can be seen the wavenumber decreases downstream and for all four frequencies, which indicates that the phase velocity increases. The phase velocity was always close to the mean velocity.

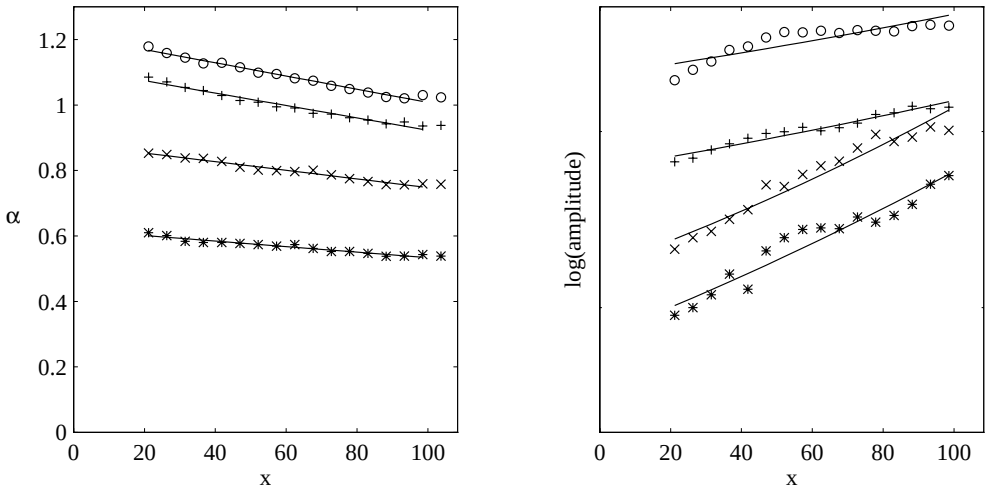

FIGURE 6.5. The downstream variation of the wavenumber (left) and amplitude (right) for four frequencies, $Re = 700$ and $a = 0.55$ mm. $(*)$ $f = 340$ Hz, $(\times)$ 485 Hz, $(+)$ 612 Hz, $(\circ)$ 669 Hz.

In the right graph the logarithm of the amplitude is plotted as a function of x. Lines of constant slope obtained through least-squares fits are also shown. A straight line in this diagram indicates an exponentially growing disturbance. The curves have been shifted vertically to simplify a comparison. The amplitude grows faster for the two low frequencies than for the two high frequencies, at least when it comes to the intensity variation in the images.

The method used to obtain the amplitude variation has to be validated before it is possible to draw any conclusions from these results. This should be made against a well known case where the amplitude variation is known or possible to measure by some other method.

To facilitate a comparison between linear stability theory and the present experimental results figure 6.6 was calculated. This figure shows in a and b curves of constant growth rate for the even and odd modes, respectively. The contours of constant growth rate are shown as solid black lines and the frequency of the wave disturbance is indicated by white contour lines, labelled with the frequency in Hz. The thick line is the demarcation line between two unstable modes. Along this line the frequency change is discontinuous. In the lower two figures (c and d) the growth rate from figures a and b have been integrated along lines of constant α. A comparison between figure 6.5 and figure 6.6 c show that the wavenumber variation along a constant frequency shows good agreement between the theoretical results and the experiments. It is not possible from this graph to explain why the largest sensitivity of the wave disturbance was obtained at $f \approx 530$ Hz, however this frequency is in the range of the most unstable frequencies. One should bear in mind that a spatial analysis may change the picture, especially since in the

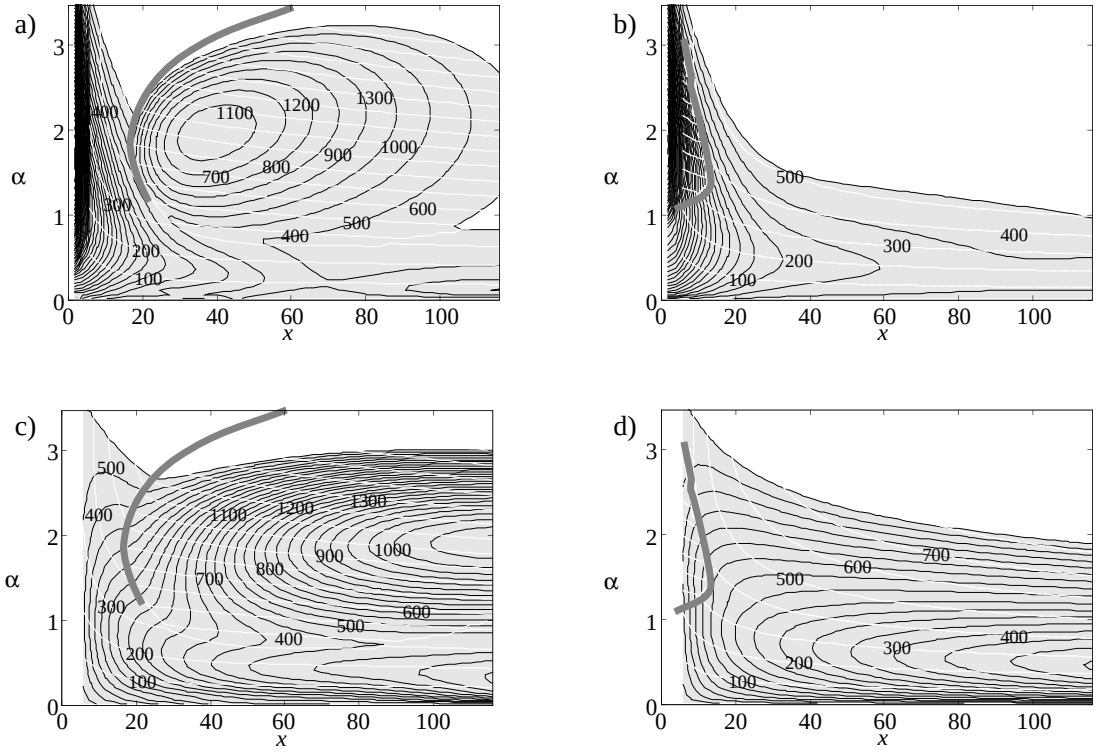

FIGURE 6.6. Contourplots of the growth rate (top) and integrated growth rate (bottom). The basic flow is calculated with gravity, $Re = 700$, $a = 0.55$ mm and $\gamma = 0.070$ N/m.

region close to the nozzle the frequency contour curves are almost parallel to the α-axis and hence the group velocity is small.

Since the wave phase is fixed by the signal to the loudspeaker, it is possible to measure the phase difference between this signal and the signal from the hot film anemometer traversed in the normal direction through the jet. The phase- and amplitude distribution in the jet can be seen in figure 6.7. The waves are anti-symmetric or sinuous, corresponding to a $\hat{v}$-even mode. In the figure the calculated amplitude distributions for the two most unstable modes are also shown for the present flow parameters (*i.e.* Reynolds number, velocity distribution and frequency of the disturbance). As can be seen neither of these distributions fit the measured distribution well, however a linear combination of the two give good agreement. At this position only the first mode is unstable, but closer to the inlet the second mode is the most unstable, so therefore both modes may appear simultaneously.

If the width of the channel is increased it gives a less developed flow and visualizations show that the waves start to occur at higher Reynolds numbers. This was also the case for the break-up, which was delayed. It was also noted that the flow of the surrounding air seems to have little or no influence on the

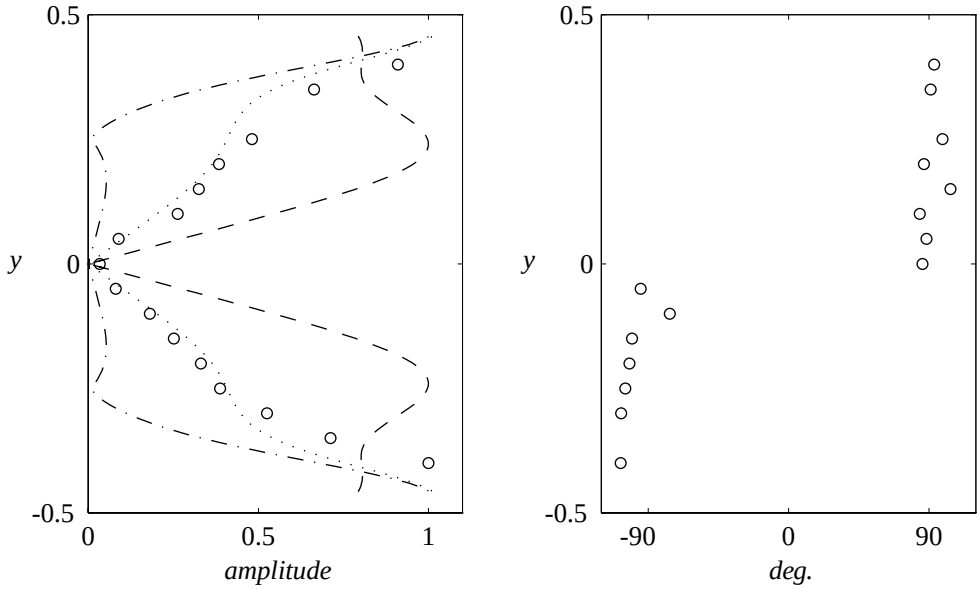

FIGURE 6.7. Phase distribution in the jet (left) and amplitude distribution (right) in the jet. Waves are triggered by a loudspeaker at 530 Hz. $Re = 700$, $a = 0.55$ mm. The maximum disturbance amplitude is approximately 0.5% of U_m. In the left picture amplitude distributions from linear theory are also shown, (- - -) first mode, (- · -) second mode and (· · ·) linear combination.

occurrence of these waves. This was investigated by blocking the airflow and changing the geometry outside the jet.

6.2.3. Break-up of the waves. The channel jet was also visualized with reflective flakes and a laser sheet in the xz-plane, see figure 5.2 *ii*. In these visualizations the waves cannot be seen at all, but instead the break-up of the waves can be clearly seen, figure 6.8. This figure contains images from the visualization at three different velocities. Both an instantaneous image as well as image-processed and time averaged images are shown.

At low velocity when the spots start to appear in the shadowgraph visualization, figure 6.3 *b*, the break-up can be seen as a local phenomenon, figure 6.8 *a*. The break-up originates from a point and it appears to create a pair of streaks originating at this single point. To enhance this structure the image is also shown after performing image-processing with edge-detection, figure 6.8 *b*. The edge-detection routine trace intensity gradients in the image.

At a slightly higher velocity streaks cover the width of the jet, figure 6.8 *c*. These appear as stronger than the streaks found upstream the break-up. The origins of these streaks are located along a ragged line parallel to the nozzle, and if the break-up is averaged over 100 frames this line can be clearly seen. The break-up line is straight and parallel to the nozzle, figure 6.8 *d*. In the centre of this image the averaging also shows that the break-up occurs more often at specific

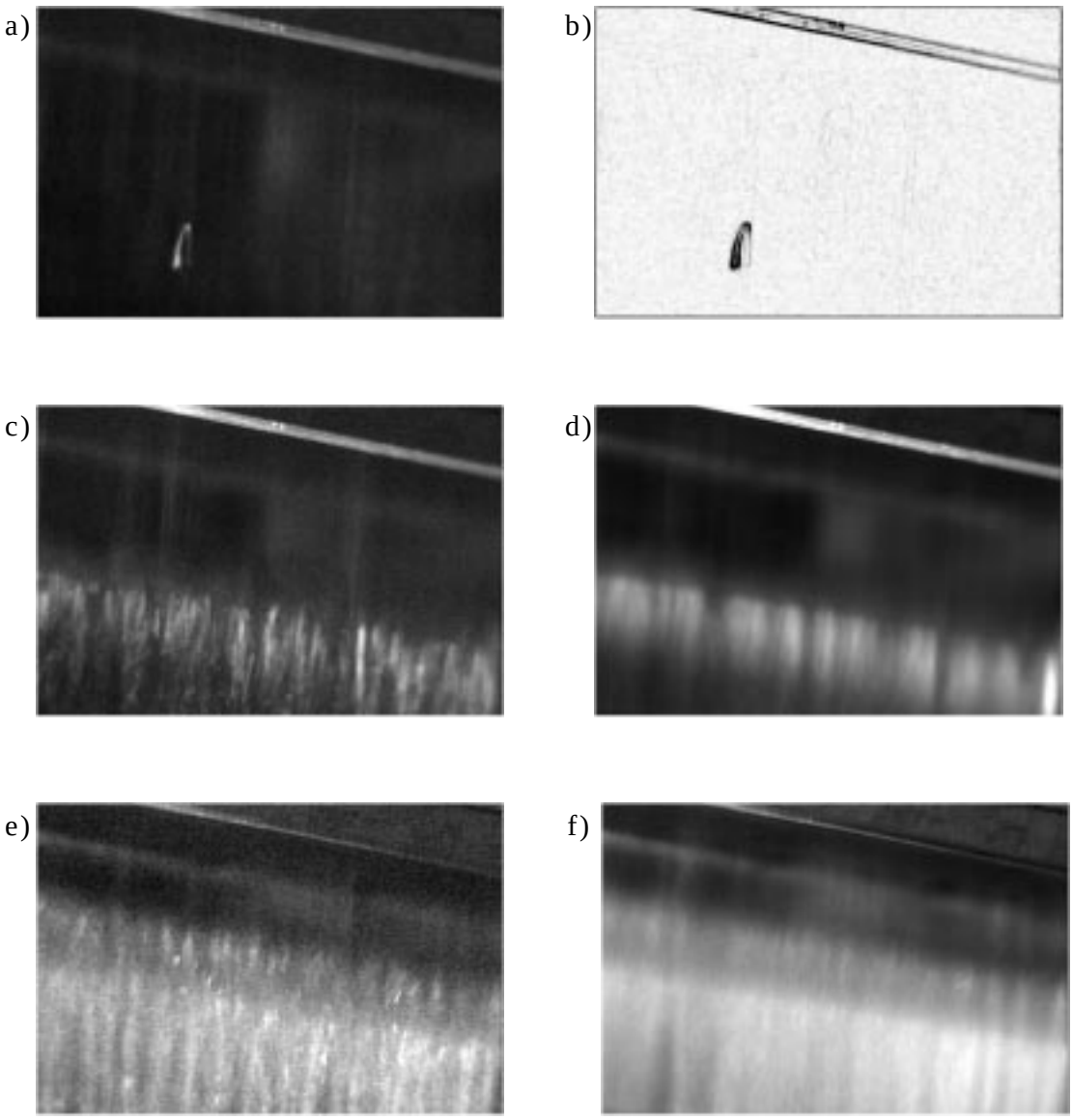

FIGURE 6.8. Visualization of the wave break-up with particle visualization. The straight line at the top is the nozzle outlet, $a = 0.55$ mm. a) single frame and b) edge detection of the break-up at $U_m = 1.9$ m/s, c) single frame and d) time average of the break-up at $U_m = 2.0$ m/s, e) single frame and f) time average of the break-up at $U_m = 2.2$ m/s.

spanwise locations, which give the streaky structure a clear periodicity. To the left in the averaged image the break-up is more stochastic since the averaging gives a more even reflection from the particles. Upstream of the averaged streaks

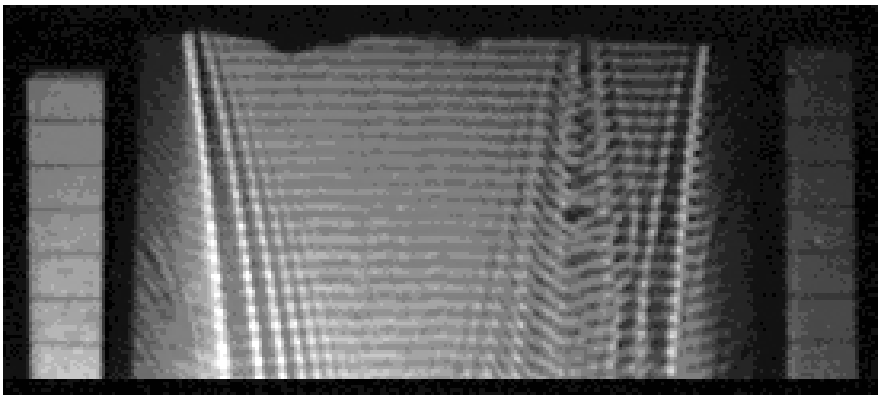

FIGURE 6.9. Channel jet with shadowgraph visualization. The waves are triggered at $f = 530$ Hz.

in the centre of the image low amplitude streaks with the same spanwise location can be seen. These originate from the nozzle.

6.2.4. Effect of upstream flow inhomogeneities. The waves found in the channel jet occur 'naturally' and are not perfectly homogeneous in the spanwise direction. Phase shifts of the waves can be seen in the jet. With particle visualizations vertical streaks originating from the nozzle was found. These cause the phase shift and were found to be stationary or slowly oscillating in the spanwise direction. A closer investigation of the conditions inside the nozzle showed that one explanation for these streaks were air bubbles trapped under the last screen. These bubbles cause vortices which are stretched through the nozzle. Occasionally, when the velocity was high, these bubbles were found to be oscillating.

Surface roughnesses and particles on the channel walls also caused stationary streaks in the jet. An example of this can be found in figure 6.9. At the top of the image the jet is emanating from the nozzle. A small roughness at one of the channel walls causes a stationary streak, which creates capillary waves. The streak also causes phase shifts in the waves on the surface. Note, that in this visualization the waves were forced.

6.2.5. Effect of turbulence intensity on the break-up. To investigate the influence of upstream disturbances on the break-up of the waves the last screen was removed. This gives a higher turbulence level at the entrance of the channel. When the screen was mounted the particles showed a steady laminar flow in the entrance region, and with the screen removed the flow was clearly more turbulent. The break-up of the waves was unaffected by this change at higher velocities when a clear break-up line could be seen in the images, but at low velocities spots could be observed more often with the screen removed, *i.e.* with a relatively higher

turbulence intensity. The presence of phase shifts in the waves increased, and also an increase of streaky structures upstream the break-up was found.

6.3. Slit jet

Pitot tube measurements were only performed at one position for the slit nozzle jet, at $x = 20$ mm. The velocity distribution was uniform in the whole region where measurements were possible. As for the channel nozzle, measurements could only be performed when the Pitot tube was completely inside the jet.

The visualizations were performed by the same methods as for the channel jet. Figure 6.10 shows 4 images of the slit jet with particle visualization. The nozzle can be seen at the top of these images, and at the left side and bottom of each of the images a scale with centimeter markings can be seen. The jet thickness is $a = 0.5$ mm in all images.

The first of these figures, figure 6.10 *a*, show the slit jet at a low velocity, $Re = 1300$. A streaky region in the centre of the jet can be seen, but if compared with the channel jet there is no apparent difference between the two cases. The streaks are stationary or slowly oscillating in the spanwise direction. By inspection of the conditions in the nozzle these can be explained in the same way, *i.e.* originating from disturbances inside the nozzle. However, at velocities where waves can be found for the channel jet, the slit jet is undisturbed. Waves could not be found at any velocity, at least not in the range which could be achieved with the present experimental apparatus. For higher velocities, figure 6.10 *b*-*d*, the streakiness becomes stronger. At low velocities the streaks seem to be fairly stationary but at the higher velocities they move randomly in the spanwise direction.

Streaks with a different behavior can also be found. These differ from the streaks discussed earlier. A transient phenomenon observed consists of two streaks which start at a spanwise position. From the first point of appearance they move at high velocity in opposite directions. The velocity of this motion is considerably higher than the rocking motion induced by the bubbles below the last screen.

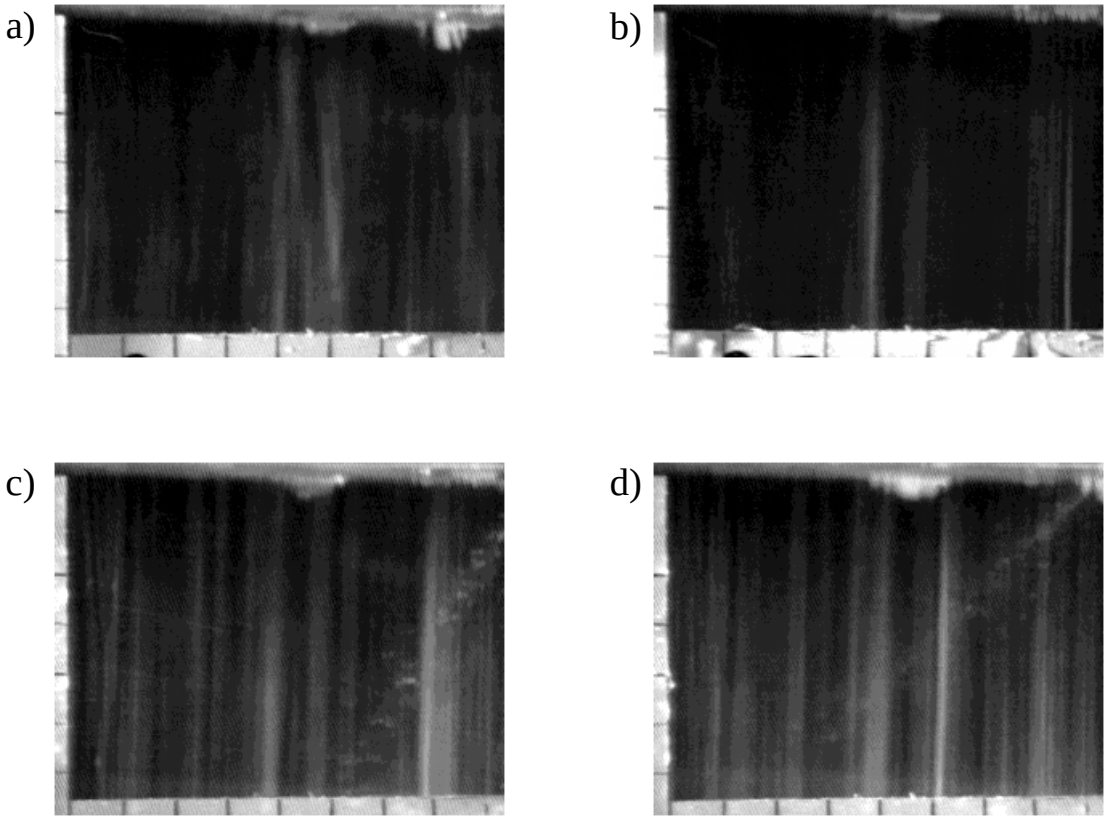

FIGURE 6.10. Slit jet with particle visualization, $a = 0.5$ mm. a) $Re = 1300$, b) 2000, c) 2900, d) 4000. Scales can be seen at left side and bottom, 1 div.=1cm.

CHAPTER 7

Discussion

In order to understand the development of free, plane liquid jets, both the development of the basic laminar flow as well as its stability have been investigated. This includes both the formulation of the problem with the appropriate boundary conditions, obtaining solutions for the basic flow field and to the stability equations for two-dimensional wave disturbances, as well as comparisons with experiments. The experiments have also shown that the wave instability results in a break-up of the laminar jet. This break-up gives rise to a turbulent jet which appears to contain streaky structures.

7.1. Basic flow development

The basic flow field of the plane liquid jet depends mainly on the nozzle geometry and the Reynolds number. For an inviscid ambient gas the jet will acquire a uniform velocity distribution far downstream. The jet will also contract in the downstream direction. The final jet velocity and width are given by conservation of mass and momentum. The relaxation length, ℓ_R, for the velocity distribution inside the jet was found to be practically independent of how well developed the flow is when it leaves the nozzle. This seems as first as a paradox but can be explained by the fact that the relevant length scale for the relaxation length will be the half channel width, and therefore it will be independent of the entrance length. When the boundary condition changes at the nozzle outlet and the relaxation process starts momentum has to be re-distributed over the full jet thickness. If instead the re-distribution of the velocity only had to take place over a thin boundary layer close to the jet surface then the entrance length would be an important parameter. However, for the location of the free surface the relaxation length ℓ_R was found to depend on the development length inside the nozzle. The relaxation length for the jet thickness was about one-fifth of the relaxation length for the velocity distribution to become uniform, for a jet emanating from a channel with an upstream fully developed parabolic profile. It was also found that the characteristic downstream development lengths ℓ_R and ℓ_E are proportional to Re.

A viscous ambient gas will affect the velocity distribution in the jet slightly. Here a thin boundary layer will develop at the surface of the jet in order to fulfill the boundary condition of no-slip. The relaxation process will be slowed down and further downstream it will also give an expansion of the jet, as compared to

the case with an inviscid outer gas. This expansion takes place since momentum flux is drained from the liquid jet to the ambient gas by the shear on the surface. In all physical applications a viscous gas will be present, and because of this the jet will never become uniform far downstream. Instead it will continue to expand. However, if the viscosity and density of the gas are lower than for the liquid this process can be considered to be slow.

The inviscid flow from the slit nozzle was calculated by Söderberg (1994). Both these results and the present measurements clearly show that the basic flow is well described by inviscid theory. Boundary layers will of course be present because of the no-slip condition at the nozzle walls, but these will be very thin at the exit since the flow is strongly accelerated. For nozzles with contraction angles that are in between the channel and slit nozzles (*i.e.* in between 0 and 90 degrees) there will be a gradual change from fully developed viscosity dominated flow to an almost inviscid flow.

7.2. Instabilities and break-up of plane liquid jets

Laminar shear flows which have a velocity distribution with an inflection point, where the shear is at a maximum, are known to be highly unstable. This is, according to linear stability theory for parallel flows a necessary but not sufficient condition for the jet to be inviscidly unstable, see *e.g.* Drazin & Reid (1981). In the case of a channel flow nozzle the relaxation of the jet velocity distribution from parabolic-like at the channel outlet to uniform, results in a velocity distribution with inflection points close to the jet surfaces. These may give rise to inflection type wave instabilities. In the experiments with the channel flow nozzle wave disturbances were observed to occur naturally.

The stability calculations were made assuming two-dimensional wave disturbances. Furthermore the flow was assumed to be locally parallel, *i.e.* the wave length of the wave disturbance was assumed to be small compared to the characteristic length scale for the development of the basic flow field. The stability was investigated in the temporal sense where the stability of a disturbance of a specific wave length is considered. Two types of wave disturbances may exist, either sinuous or varicose. Depending on the parameters of the problem (such as the Reynolds number and the basic velocity distribution) one or several modes may be unstable. For typical parameter ranges studied up to five different unstable modes were found. Three of these were sinuous (anti-symmetric) and two were varicose (symmetric). The two symmetric modes have counterparts in the anti-symmetric modes and the first of these two pairs has eigenfunctions with a maximum amplitude at the point of inflection. The other pair of modes has maximum growth located at low wavenumbers. These two modes have their maximum amplitude at the surface.

The fifth mode (e_{III}), is only found in a limited part of the parameter space. The eigenfunction of $\hat{v}$ show that the amplitude is zero at the surface for low Re,

i.e. it does not distort the jet surface. Since it does not distort the jet surface it cannot be observed through shadowgraph visualization. The origin of this mode is not clear.

The measured amplitude distribution of the forced wave disturbance was found to originate from a sinuous mode. However, neither of the three modes could approximate the amplitude distribution accurately. Instead a linear combination of the surface wave mode (e_{II}) and the fifth mode (e_{III}) give a good approximation of the measured distribution.

The break-up of the waves creates strong streaky structures in the jet which are stronger than the streaks originating from the nozzle. This can be judged based on the appearance of the streaks with particle visualization. The origin of the break-up is not clear, but may be related to the interaction between two or more unstable modes.

7.3. Relevance to paper manufacturing and future work

The Reynolds numbers in this study are much smaller than those typically occurring in modern paper manufacturing. The presence of fibres and fibre flocs will however influence the generation and destruction of turbulence, which will result in turbulent length scales larger than the size of the fibres and/or flocs. In analogy with the Kolmogorov dissipation length scale hypothesis this would correspond to a large value of the kinematic viscosity. Based on this a relevant Reynolds number can not be derived with a viscosity taken to be the same as for water, but it should be considerably higher. Therefore the present results may not only serve as a thorough study of free, plane Newtonian jets but also have relevance for the fibre suspension jets at high velocities.

In order to investigate the influence of fibres similar experiments should be made with fibre suspensions. This would give the possibility to find an effective viscosity for fibre suspensions which may be used for modelling purposes.

7.4. Conclusions

- If a plane liquid jet emanates from a nozzle with a partially or fully developed flow the process of velocity profile relaxation will always be present. The effect of this process depends on the contraction ratio of the nozzle. A slit nozzle will give a velocity distribution which is close to that of the potential flow solution.

- Stability calculations are strongly affected by the boundary conditions applied to the jet surface. With the assumption of an inviscid gas the strength of the instability is strongly overpredicted for most wave numbers.

- The profile relaxation process may cause a wavy instability of the jet. Linear stability theory as well as experiments have shown that the most unstable mode is of sinuous type. Controlled experiments where a wave disturbance was excited at the nozzle have shown how the wave number and frequency of the disturbance are related which also gives that the phase speed of the waves is close to the mean flow speed of the jet.

- The waves were found to increase in amplitude in the downstream direction and break up if the velocity of the liquid is high enough. The break-up results in strong streamwise streaks which affects the whole width of the jet. It will also cause partial disintegration of the jet, *i.e.* spray formation. The streamwise streaks caused by the break-up is much stronger than streaks originating from the inside of the nozzle.

- Streaky structures were also observed when disturbances existed in the head box, both for the channel and the slit nozzles.

Acknowledgements

I wish to thank my supervisor Prof. Henrik Alfredsson for his advise during this work and his suggestions and help with the manuscript. Prof. Bo Norman, Department of Pulp and Paper Chemistry and Technology shared generously his knowledge of the science and art of paper manufacturing. I also wish to thank Prof. Arne Johansson for the opportunity to work within the Department of Mechanics and Prof. Fritz Bark for incorporating this project into the FaxénLaboratory. Marcus Gällstedt is thanked for his help with the construction of the experimental apparatus. I would also like to thank all research students and staff at the department, especially my colleagues at the Fluid Physics Laboratory Andrey Bakchinov, Per Elofsson, Ardeshir Hanifi, Carl Häggmark, Mitsuyoshi Kawakami, Renaud Lavalley, Masaharu Matsubara, Nils Tillmark and Johan Westin. Special thanks to Matsu for sharing office space and for all the fruitful discussions concerning fluid mechanics and other things.

Finally I would like to thank my wife Satu for her support and my children Mikaela, Madeleine and Julia for the necessary distraction.

This work has been funded by NUTEK, the Swedish National Board for Industrial and Technical Development.

Bibliography

Batchelor, G. K. 1967 *An Introduction to Fluid Dynamics.* Cambridge University Press

Brennen, C. 1970 Cavity surface wave patterns and general appearance. *J. Fluid Mech.* **44** 33.

Bogy, D. B. 1979 Drop Formation in a Circular Liquid Jet. *Ann. Rev. Fluid Mech.* **11** 207–227.

Chandrasekhar, S. 1961 *Hydrodynamic and Hydromagnetic Stability.* Oxford: Clarendon Press.

Debler, W. & Yu, D. 1988 The Break-up of Laminar Liquid Jets. *Proc. Roy. Soc. Lond. A* **415** 106–120.

Fletcher, C.A.J. 1991 *Computational Techniques for Fluid Dynamics*, 2nd edn, vol. I and II. Springer-Verlag.

Drazin, P. G. & Reid, W. H. 1981 *Hydrodynamic Stability.* Cambridge University Press.

Gavis, J. & Modan, M. 1967 Expansion and contraction of jets of Newtonian liquids in air: Effect of tube length. *Phys. Fluids* **10**, 487–498.

Goedde, E. F. & Yuen, M. C. 1970 Experiments on liquid jet instability. *J. Fluid Mech.* **40** 495–514.

Hagerty, W. W. & Shea, J. F. 1955 A Study of the Stability of Plane Fluid Sheets. *J. Appl. Mech.* **22**, 509–514.

Hoyt J. W. & Taylor J.J. 1968 Waves on water jets. *J. Fluid Mech.* **83**, 119–227.

Joseph, D. D. 1978 Slow Motion and Viscometric Motion; Stability and Bifurcation of the Rest State of a simple Fluid. *Arch. Rat. Mech. Anal.,***56.**

Lamb, H. 1932 *Hydrodynamics*, 6th edn. Dover.

Leib S. J. & Goldstein, M. E. 1986 The generation of capillary instabilities in a liquid jet. *J. Fluid Mech.* **168**, 479–500.

Li, X. & Tankin, R.R. 1991 On the temporal stability of a two-dimensional viscous liquid sheet. *J. Fluid Mech.* **226**, 425–443.

Lindqvist, A. N. 1996 *Structures in the Flow from Paper Machine Headboxes.* Licentiate Thesis 1996:16 L, Div. of Fluid Mechanics, LuleåUniversity of Technology.

MacCarthy, M. J. & Molloy, N. A. 1974 Review of Stability of Liquid Jets and the Influence of Nozzle Design. *Chem. Engng. J.* **7**, 1–20.

Mansour, A. & Chigier, N. 1995 Dynamic behaviour of liquid sheets. *Phys. Fluids A* **3**, 2971–2979.

Nickell, R. E., Tanner, R.I. & Caswell B. 1968 The solution of viscous incompressible and free surface flows using finite element methods. *J. Fluid Mech.* **65**, 189–206.

Pai, S. I. 1954 *Fluid Dynamics of Jets.* Van Nostrand.

Plateau, J. 1873 Statique expérimentale et théorique des liquides soumis aux seules forces moléculaires, cited by Lord Rayleigh in *Theory of Sound, 2nd edn, vol. II.* Dover.

Rayleigh, Lord. 1896 *Theory of Sound* , 2nd edn, vol. II. Dover.

Savart F. 1833 *Ann. Chem.* **53**, 337.

Schlichting, H. *Boundary layer theory*, 7:th edn. McGraw-Hill.

Söderberg, D. 1994 *An Experimental Study of the Stability of Plane Liquid Jets.* M.Sc.Thesis, Dept. of Mechanics, Royal Institute of Technology. Reprint, TRITA-MEK TR 1996:5.

Taylor G. I. 1959 The dynamics of thin sheets of fluid III. Disintegration of fluid sheets. *Proc. Roy. Soc. A* **253**, 313–321.

Tillet , J. P. 1968 On the laminar flow in a free jet of liquid at high Reynolds numbers. *J. Fluid Mech.* **32**, 273–292.

Van Dyke, M. 1970 Entry flow in a channel. *J. Fluid Mech.* **44**, 813–823.

Yu, T. & Liu T. 1992 Numerical solution of a Newtonian jet emanating from a converging channel. *Computers Fluids* **21**, No. 4, 813–823.

Wolf, D.H., Incropera F.R. & Wiskanta R. 1995 Measurement of the turbulent flowfield in the free-surface jet of water. *Exp. in Fluids* **18**, 397–408.

APPENDIX A

Conservation laws for a free liquid jet

Consider a steady two-dimensional laminar liquid jet emanating from a channel into an inviscid gas. The streamwise momentum equation is given by

$$u\frac{\partial u}{\partial x} + v\frac{\partial u}{\partial y} = -\frac{\partial p}{\partial x} + \frac{1}{Re}\left(\frac{\partial^2 u}{\partial x^2} + \frac{\partial^2 u}{\partial y^2}\right),$$

and the continuity equation by

$$\frac{\partial u}{\partial x} + \frac{\partial v}{\partial y} = 0.$$

The flow of the jet is assumed to be symmetric with respect to the centreline of the jet, $y = 0$, and these equations are non-dimensionalized with the mean velocity in the channel and the half channel height. At the solid walls there are no-slip conditions for u and v, and at the surface of the jet there are the no-shear condition and the condition that there should be no flow across the surface of the jet. The wall and free surface of the jet is given by $y = h(x)$.

The streamwise momentum equation is integrated from the centreline to the wall/surface,

$$\int_0^h \left[u\frac{\partial u}{\partial x} + v\frac{\partial u}{\partial y} + \frac{\partial p}{\partial x} - \frac{1}{Re}\left(\frac{\partial^2 u}{\partial x^2} + \frac{\partial^2 u}{\partial y^2}\right)\right]\, dy = 0.$$

The integration of the convective terms gives

$$\int_0^h \left(u\frac{\partial u}{\partial x} + v\frac{\partial u}{\partial y}\right)\, dy = \int_0^h \frac{\partial u^2}{\partial x}\, dy + [uv]_h = \frac{d}{dx}\int_0^h u^2\, dy + \left[u(v - \frac{dh}{dx}u)\right]_h, \quad (1)$$

where $[\ldots]_h$ implies that the expression within the brackets is evaluated at h. Here we have made use of the following relation

$$\frac{d}{dx}\int_{g_1(x)}^{g_2(x)} f(x)\, dy = \int_{g_1(x)}^{g_2(x)} \frac{df(x,y)}{dx}\, dy + \frac{dg_2(x)}{dx}f(x, g_2(x)) - \frac{dg_1(x)}{dx}f(x, g_1(x)).$$

The second term on the *R.H.S* in eq. (1) is zero both at the wall and at the surface of the jet. This since at the wall both u and v are zero and at the surface

$$u\frac{dh}{dx} = v,$$

which is the kinematic equation for the free surface in a steady flow. This gives that

$$\int_0^h \left(u\frac{\partial u}{\partial x} + v\frac{\partial u}{\partial y} \right)\, dy = \frac{d}{dx}\int_0^h u^2\, dy.$$

The integration of the pressure term gives

$$\int_0^h \frac{\partial p}{\partial x}\, dy = \frac{d}{dx}\int_0^h p\, dy - \frac{dh}{dx}[p]_h,$$

and of the viscous stress terms

$$\int_0^h \left(\frac{\partial^2 u}{\partial x^2} + \frac{\partial^2 u}{\partial y^2} \right)\, dy = \int_0^h \frac{\partial}{\partial y}\left(-\frac{\partial v}{\partial x} \right)\, dy + \left[\frac{\partial u}{\partial y} \right]_h = -\left[\frac{\partial v}{\partial x} \right]_h + \left[\frac{\partial u}{\partial y} \right]_h,$$

since

$$\frac{\partial u}{\partial y} = v = 0 \quad \text{at} \quad y = 0.$$

The integration of the streamwise momentum equation finally gives

$$\frac{d}{dx}\int_0^h \left(u^2 + p \right)\, dy + \left[-p\frac{dh}{dx} + \frac{1}{Re}\left\{ \frac{\partial v}{\partial x} - \frac{\partial u}{\partial y} \right\} \right]_h = 0. \tag{2}$$

If the surrounding gas is inviscid the jet will become uniform far downstream

$$\frac{dh}{dx} = \left[\frac{\partial u}{\partial y} \right]_h = \left[\frac{\partial v}{\partial x} \right]_h = 0 \quad \text{when} \quad x \to \infty,$$

and the pressure is assumed to be constant, which gives that

$$\int_0^h u^2\, dy = u_\infty^2 h_\infty$$

The conservation law related to the mass flow is obtained by integration of the continuity equation

$$\int_0^h \left(\frac{\partial u}{\partial x} + \frac{\partial v}{\partial y} \right)\, dy = \frac{d}{dx}\int_0^h u\, dy + \left[v - \frac{dh}{dx}u \right]_h = \frac{d}{dx}\int_0^h u\, dy = 0, \tag{3}$$

which gives

$$\int_0^h u\, dy = u_\infty h_\infty.$$

A.1. Poiseuille flow case

Consider a channel with a fully developed parabolic profile, $u(y) = 1 - y^2$. If the Reynolds number is assumed to be large and the pressure constant, eq. (2) becomes

$$\frac{d}{dx}\int_0^h u^2\, dy = 0.$$

This gives that

$$\int_0^h u^2 \, dy = \frac{8}{15} = C_{momentum},$$

which is independent of x. Also the equation for the conservation of mass flow, eq. (3), gives that

$$\int_0^h u \, dy = \frac{2}{3} = C_{massflow}.$$

Hence far downstream

$$U_\infty^2 h_\infty = C_{momentum}$$
$$U_\infty h_\infty = C_{massflow}$$

which will give

$$h_\infty = \frac{C_{massflow}^2}{C_{momentum}} = \frac{5}{6}.$$

This is valid in the limit $Re \to \infty$.

APPENDIX B

Image analysis of shadowgraph visualization

An expression will be derived in order to couple the amplitude of waves on thin liquid sheet and the intensity variation of a shadowgraph visualization.

B.1. Intensity as a function of curvature

The liquid sheet is assumed to have a constant thickness whereas and the surface of the liquid sheet is subjected to sinuous perturbations. If the shadowgraph method is used parallel light passes through the sheet. This is modelled with the aid of geometrical optics where the sheet is assumed to be a thin lens, which can have several configurations, see figure 1.2 in Chapter 1.

We limit our interest to the maxima and minima of the waves. At these points the normal to the surface is parallel to the incoming light. We hence study only central rays, which gives the following expression for a surface according to figure B.1.

$$\frac{1}{a} = \left(\frac{n_{liquid}}{n_{gas}} - 1\right)\left(\frac{1}{R_1} + \frac{1}{R_2}\right),$$

where $R_{1,2}$ are the radiia of curvature for the two liquid-gas interfaces, n_{gas} and n_{liquid} denotes the refraction indices and a is the so called focal distance. In this expression the radiia are both defined as positive if the jet forms a bi-convex lens. With this assumption it is clear that for the anti-symmetric case $R_1 = -R_2$, which implies that the rays will pass through the jet undisturbed. Hence only a symmetric disturbance would cause a deflection of the rays. However, it may be shown that if the lens is not assumed to be thin and the two interfaces have the

Surface A	Surface B	Mode
convex	convex	anti-symmetric
convex	concave	symmetric
concave	convex	anti-symmetric
concave	concave	symmetric

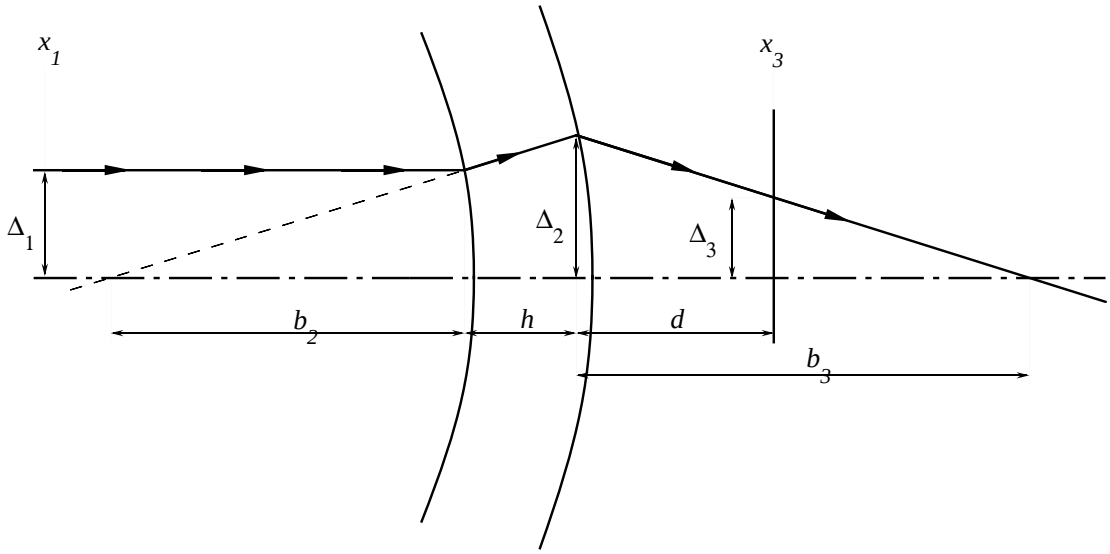

FIGURE B.1. Geometric relations for two initially parallel rays passing through a thin liquid sheet.

same radius R, separated by a distance h, this gives

$$\frac{1}{b_3^\alpha} = \left(\frac{n_{liquid}}{n_{gas}} - 1\right)\left(1 - \frac{1}{1+\epsilon h/R}\right)\frac{1}{R}, \tag{1}$$

$$\frac{1}{b_3^\beta} = \left(\frac{n_{liquid}}{n_{gas}} - 1\right)\left(\frac{1}{1-\epsilon h/R} - 1\right)\frac{1}{R}, \tag{2}$$

where the superscripts α and β denote the concave-concave and convex-convex cases, respectively, and $\epsilon = 1 - n_{gas}/n_{liquid}$.

Now, consider two rays passing through the undisturbed jet. These originate far away from the jet and at a point x_1, before they pass through the jet the rays are parallel and separated by a distance Δ_1. This distance will be the same at a point x_3 after passing an undisturbed liquid sheet, and the light flux between these two rays is constant.

Geometric properties, see figure B.1, will now give for a distorted liquid sheet

$$\frac{\Delta_2}{b_2 + h} = \frac{\Delta_1}{b_2},$$
$$\frac{\Delta_3}{b_3 - d} = \frac{\Delta_2}{b_3},$$

which together with the deflection at the first surface,

$$b_2 = \frac{R}{\epsilon},$$

and eqs. (1) and (2), can be reduced to

$$\frac{\Delta_3^\alpha}{\Delta_1} = 1 + \frac{\epsilon h}{R} - \frac{\sigma \epsilon h}{R^2}, \tag{3}$$

where α indicates that this is for the concave-concave case and we define σ as

$$\sigma = d\left(\frac{n_{liquid}}{n_{gas}} - 1\right).$$

In a similar way this can be done for the convex-convex case,

$$\frac{\Delta_3^\beta}{\Delta_1} = 1 - \frac{\epsilon h}{R} - \frac{\sigma \epsilon h}{R^2}. \tag{4}$$

Now by subtracting eq. (4) from eq. (3)

$$\frac{\Delta_3^\alpha}{\Delta_1} - \frac{\Delta_3^\beta}{\Delta_1} = 2\frac{\epsilon h}{R}. \tag{5}$$

If the surface of the jet is disturbed the rays will now be distorted due to the curvature of the surface. One of the rays is considered to be passing through the centre of the wave crest, and hence remain undisturbed. The other ray will pass though a position where the curvature will cause a deflection. After passing through the sheet the rays will diverge or converge depending on if the surfaces are convex or concave. At a point after that the rays have passed through the jet, x_3, the distance between these hence has changed and since the flux between them will remain constant the intensity at this point will also change. The conservation of the light flux can then be expressed as

$$I_1\Delta_1 = I_2\Delta_2 = I_3\Delta_3. \tag{6}$$

Eq. (5) together with eq. (6) gives

$$\frac{I_1}{I_3^\alpha} - \frac{I_1}{I_3^\beta} = 2\frac{\epsilon h}{R}. \tag{7}$$

A relative change, Λ, in intensity can be expressed as

$$I_3^{\alpha,\beta} = I_1(1 + \Lambda^{\alpha,\beta}), \quad \Lambda^{\alpha,\beta} = \frac{I_3^{\alpha,\beta} - I_1}{I_1},$$

which together with eq. (7) becomes

$$2\frac{\epsilon h}{R} = \frac{1}{1+\Lambda^\alpha} - \frac{1}{1+\Lambda^\beta}.$$

which if we assume that $\Lambda^\alpha = -\Lambda^\beta = \Lambda$, can be reduced to

$$\frac{1}{|R|} = \frac{1}{\epsilon h}\left|\frac{\Lambda}{1-\Lambda^2}\right|. \tag{8}$$

B.2. Surface curvature as function of wave amplitude

The surface of the liquid sheet is given by

$$\mathcal{F}(x,y) = y - f(x) = y - c + A\sin(kx),$$

where c is an arbitrary constant, A the amplitude of the waves and k the wavenumber. The normal to this surface, $\mathbf{n}$, is given by

$$\mathbf{n} = \nabla\mathcal{F}/|\nabla\mathcal{F}| = (-f_x, 1)/|\nabla\mathcal{F}|, \quad |\nabla\mathcal{F}| = \sqrt{1+f_x^2},$$

hence the radius of curvature is defined as,

$$\frac{1}{R} = \nabla\cdot\mathbf{n} = \nabla\cdot(\nabla\mathcal{F}/|\nabla\mathcal{F}|)$$

$$\begin{aligned}\Rightarrow \frac{1}{R} &= -f_{xx}(1+f_x^2)^{-1/2} + f_x^2 f_{xx}(1+f_x^2)^{-3/2} \\ &= Ak^2\sin(kx)\left\{1+A^2k^2\cos^2(kx)\right\}^{-1/2} \\ &\quad - A^3k^4\cos^2(kx)\sin(kx)\left\{1+A^2k^2\cos^2(kx)\right\}^{-3/2}.\end{aligned}$$

But we are only interested of the curvature where the wave has its maximum, and this gives

$$\Rightarrow \frac{1}{R} = Ak^2, \tag{9}$$

which is an exact relation between the amplitude of the wave and the curvature of the surface.

Together eqs. (8) and (9) give the amplitude as a function of wavenumber and intensity,

$$|A|k^2 = \frac{1}{\epsilon h}\left|\frac{\Lambda}{1-\Lambda^2}\right|.$$